Thesis for the degree of Doctor of Philosophy

Mitigation of urban storm water runoff through application of computational fluid dynamics

Kaj Pettersson

Department of Architecture and Civil Engineering
CHALMERS UNIVERSITY OF TECHNOLOGY
Göteborg, Sweden 2021

Abstract

This thesis covers computational methods for improving the ability of green roofs to mitigate storm water runoff in urban environments. Roofs with living vegetation, known as green roofs, have been used for this purpose however quantification of their ability to slow and stop rainfall runoff has not been undertaken to a large degree. In this work two different approaches are taken: i) to improve green roof performance by optimizing their location on a building facade; and ii) to optimize the design of the growth substrate by examining the impact of the porous microstructure on infiltrating flow. The approach for optimization by placement makes use of traditional computational fluid dynamics and applies a full turbulence model to an Eulerian multiphase system consisting of a steady-state wind phase and a set of transient rainfall phases. The rainfall phases are determined by droplet size and the quantity incident upon the building facade is calculated and compared to experimental results. The analysis shows that the accuracy varies widely dependent upon location upon the structure and several sources of error are discussed. The second approach makes use of the lattice Boltzmann technique to aid in the deisgn of the growth substrate. Several representative porous media are generated using monodisperse randomly packed particles and gravity-driven infiltration is tracked from an initialized standing water height above the porous subdomain. Many aspects of the flow and properties of the microstructure are analyzed and conclusions are drawn based upon such factors as interfacial area, saturation rate, capillary pressure, and pore size distribution. Guidelines are drawn to aid in the design of thin homogeneous growth substrates based upon the findings. These ideal cases are compared to simulations performed on XMT scans of real growth substrate material and some conclusions are drawn on the observed differences.

Keywords: Green roof, CFD, lattice Boltzmann, microstructure, wind-driven rain, infiltration, building facade.

Sammanfattning

Titel: Förbättrad hantering av urbant dagvattenflöde i gröna tak genom användning av numeriska beräkningsverktyg

Denna avhandling syftar till att förbättra förmågan hos gröna tak att hantera dagvattenflöde i urbana miljöer genom att använda numeriska beräkningsverktyg. Tak som täcks med levande växtlighet, så kallade gröna tak, har länge använts för att hantera dagvattenflöde i urbana miljöer. Trots det har inte deras förmåga att hindra och fördröja avrinning från regn kvantifierats tillräckligt. I detta arbete används två olika angreppssätt: i) att förbättra prestandan genom att optimera var på byggnaden växtligheten placeras, och ii) att optimera själva utformningen av växtsubstratet genom att undersöka den porösa mikrostrukturen och dess inverkan på infiltrationsflödet. Optimeringen av takens placering baseras på traditionell CFD där en fullständig turbulensmodell används i ett Euleriskt multifasflödessystem som innehåller konstant vindhastighet och en uppsättning dynamiska regnevent. Regnets intensitet bestäms av storleken på regndropparna och antalet regnevent som verkar på olika delar av byggnaden beräknas för att jämföras med experimentella resultat. Analysen visar att tillförlitligheten varierar stort beroende på var på byggnaden beräkningen utförs. Flera felkällor diskuteras i avhandlingen. För det andra angreppssättet med målet att förbättra takens prestanda genom att optimera utformningen av växtsubstratet används beräkningsteknik baserad på lattice Boltzmann. Flera representativa porösa material analyseras genom att en fiktiv porstorleksfördelning skapas där partiklar packats slumpmässigt. Gravitationen driver infiltrationen genom materialet genom att en vattenyta med ett givet djup ansätts ovanpå substratet. Aspekter på mikrostrukturens påverkan på vattenflöde och flödesegenskaper analyseras och slutsatser baserat på gränssnittsytan, mättningshastighet, kapillärtryck och porstorleksfördelning presenteras. För att underlätta utformningen av tunna homogena växtsubstrat används resultaten för att utveckla designriktlinjer. Dessa idealfall jämförs sedan med XMT-skanning av verkliga växtsubstrat för att säkerställa den praktiska tillämpbarheten av resultaten.

Nyckelord: gröna tak, CFD, lattice Boltzmann, mikrostruktur, slagregn, infiltration, byggnads fasad.

Acknowledgments

Wow, it's the end of an age! ...or so it seems to me. I cannot believe 5 years has gone by in what feels like such a short time. It seems like yesterday that I stepped into the office full of ideas and confidence. Well, safe to say 5 years on I am older and hopefully a little wiser, time will tell on that one! As I look back on the time I appreciate all of the successes and failures that led me to who and where I am now. I will always be grateful for the time I've spent at Chalmers and for the opportunity to chase my insatiable desire to learn more about this fascinating world we live in. Thank you!

I would like to begin my thanks with my supervisors, who have been enthusiastic and supportive throughout my work. Angela, thank you so much for your guidance and trust along the way, I hope you found it as illuminating as I did! Dario, thank you for your patience and support as well as discussions both within and outside of work topics! Pär, thank you for your insight and aid along the way. Though not strictly speaking a supervisor; Srdjan I'd like to thank you as well for your contributions but moreso your sense of humor, which always gave me a laugh!

I would also like to thank my colleagues, in particular Pepe, Josef, Govin, Tommie, Yichi and all of the coffee/lunch therapy group. It was always a pleasure to have a chat and a laugh together! I'm sure I've missed loads of people by name so just pencil yourself in ;).

I want to express my most profound gratitude to my family; my mother Rita and my brother Thor. You guys have always believed in me. There are no words to truly express what you guys mean to me so I won't, you know it already anyway.

My friends, my crew! It simply would not have been possible for me to reach this stage without you all. You are the greatest bunch of souls I've ever met or likely will. You've always been there for me. Thank you!

My final thanks goes out to musicians across the globe in times past and present. The sciences and the arts are flip sides of a coin, one cannot exist without the other and together they create the cosmic symphony known as life that we all enjoy for the moment. In that regard I would like to mention both Truckstop Alaska and the Abyss for providing endless conversations and the opportunity to meet wonderful people and discover thousands of bands over the years.

Kaj Pettersson
Göteborg, May 2021

List of Publications

This thesis is based on the following appended papers:

Paper 1. Kaj Pettersson, Sinisa Krajnovic, Pär Johansson and Angela Sasic Kalagasidis. *Simulating wind-driven rain on building facades using Eulerian multiphase with rain phase turbulence model.* Building and Environment (2016), 106: 1–9.

Paper 2. Kaj Pettersson, Dario Maggiolo, Srdjan Sasic, Pär Johansson and Angela Sasic Kalagasidis. *On the impact of porous media microstructure on rainfall infiltration of thin homogeneous green roof growth substrates.* Journal of Hydrology (2019), 582: 124286.

Paper 3. Kaj Pettersson, Dario Maggiolo, Srdjan Sasic, Pär Johansson and Angela Sasic Kalagasidis. *Contribution of dynamic capillary pressure to rainfall infiltration in thin homogeneous growth substrates* Postprint, under review, (2021).

Paper 4. Kaj Pettersson, Dario Maggiolo, Srdjan Sasic, Pär Johansson and Angela Sasic Kalagasidis. *Impact of topological heterogeneity on liquid infiltration of a thin growth substrate using lattice Boltzmann on XMT scanned core images* Preprint, to be submitted, (2021).

Other relevant publications co-authored by Kaj Pettersson:

Lars Gullbrekken, Sivert Ulvsløkk, Tore Kvande, Kaj Pettersson and Berit Time. *Wind pressure coefficients for roof ventilation purposes* Journal of Wind Engineering and Industrial Aerodynamics (2018), 75:144-152.

List of Acronyms

ANN	–	Artificial neural network
CFD	–	Computational Fluid Dynamics
CFL	–	Courant-Friedrichs-Lewy
DNS	–	Direct numerical simulation
EM	–	Eulerian Multiphase
EVM	–	Eddy viscosity model
HAM	–	Heat-air-moisture
FEM	–	Finite element method
FVM	–	Finite volume method
G-A	–	Green-Ampt model
LBGK	–	Lattice-Bhatnagar-Gross-Krook
LBM	–	Lattice Boltzmann method
LECA	–	Lightweight expanded clay aggregate
LGCA	–	Lattice Gas Cellular Automata
LPT	–	Lagrangian Particle Tracking
N-S	–	Navier-Stokes
PDF	–	Probability distribution function
PNM	–	Pore network model
PANS	–	Partially-averaged Navier-Stokes
RANS	–	Reynolds Averaged Navier-Stokes
RGPZ	–	Revil, Glover, Pezard, and Zamora model
RNG	–	Re-normalization group
RSM	–	Reynolds Stress Model
SIMPLE	–	Semi-implicit method for pressure-linked equations
SMHI	–	Swedish Meteorological and Hydrological Institute
SWRC	–	Soil water retention curve
TWRI	–	Transient water release and imbibition
UHI	–	Urban heat island
VGM	–	van Genuchten-Mualem model
WRC	–	Water retention curve
WDR	–	Wind-driven rain
XMT	–	X-ray microtomography

Contents

Part I

Introductory chapters

Chapter 1

Introduction

1.1 Green roof design and usage

Green roofs are defined as any roofing construction incorporating vegetation, which can range from grasses up to trees and bushes. The vegetation is accompanied by a soil or soil-like layer called the growth substrate as well as several additional layers, as seen in Figure 1.1. While most modern green roof designs incorporate many of the additional layers they are not necessarily always included. Green roofs are classified into two major types, dependent upon the size of the vegetation and the consequent thickness of the construction. Intensive green roofs consist of a thicker growth substrate layer, typically between 20-100 cm, and vegetation ranging from trees to bushes to flowerbeds. They can be used as gardens or park-like areas however they require additional structural considerations as well as frequent maintenance. Extensive green roofs consist of growth substrates 5-20 cm deep and are generally planted with low-lying hardy vegetation such as sedum and various grasses. These constructions typically do not require additional load-bearing considerations and maintenance is minimal provided weather patterns are not extreme. The vegetation for these types of roofs is primarily selected on the basis of hardiness, with lesser consideration given to aesthetics or alternative function. There are also green roof designs falling between these two types, known as semi-intensive, with a substrate thickness between the two previously mentioned and with vegetation a combination of grasses and flowers and mid-height plants.

Growth substrates used in green roofs consist of a mix of materials ranging from organic such as bark chips, biochar, compost and mature soil matter to inorganic such as expanded clay aggregates, sands, pumice stone, crushed brick, and chemically inert plastics. The appropriate mix is determined by a balance between water requirements for the vegetation and desired drainage as well as long-term stability with regard to vegetation growth. An additional consideration currently under investigation is the choice of materials for the purpose of water purification and entrapment of pollutants including heavy metals. The filter sheet is included to prevent erosion of the growth substrate and blockage of the drainage with substrate material. The drainage layer is dedicated to to removal of excess water and consists of intermittent linked basins or channels of a liquid-impermeable material such as a plastic whereby the excess water

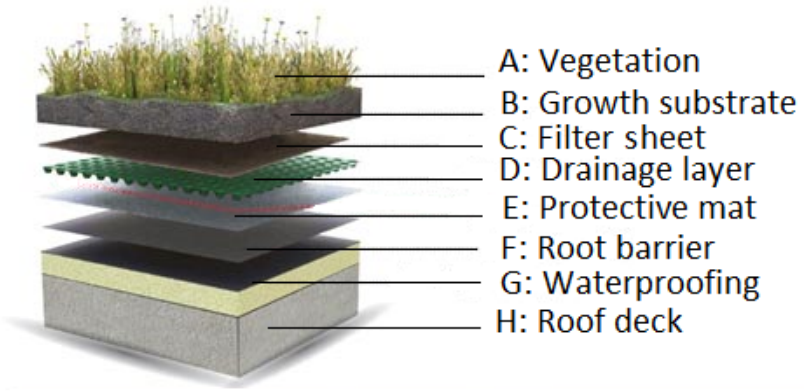

Figure 1.1: Green roof component breakdown. (OrgeBot 2017)

is drained away from the roof. Underneath this we have several layers dedicated to the protection of the roofing structure from any damage caused by water leakage or root growth.

Green roof usage dates back to at least the medieval ages and were used by the Vikings. Findings in Scandinavia and Newfoundland sites show their use in 700-1000 A.D. Archaeologists presume their usage was for defense and insulation purposes. In more modern times the constructions have experienced a resurgence of interest, for a variety of reasons. Claims for their usage consist of aesthetic and social benefits to more quantifiable contributions such as reduction of urban noise pollution to traditional pollution filtering and entrapment to urban heat island reduction as well as mechanical damage protection and urban storm water management.

The contribution to urban noise pollution reduction has been demonstrated using modeling as well es experimentation. Van Renterghem et al. used 2D and 3D full wave modeling to determine that specific placement of green walls and roofing within narrow urban canyons reduces automobile noise within courtyards (Van Renterghem et al. 2013). In particular combining wall and roof vegetation maximizes this effect and placement on higher storeys of a building also aid in their performance. Connelly and Hodgson investigated the transmission loss of vibrations using specially designed experimental facilities and found that green roofs aided in the reduction of low frequency noise transmission (Connelly and Hodgson 2013). This result is complemented by another study which determined a reduction in decibel level for both medium and high frequency ranges by 0-10 dB due to the substrate and acoustic scattering by the vegetation (Lunain et al. 2016).

The possibility of using green roofs to aid in storm water purification and pollutant entrapment has been found to be viable, however there is also evidence they may contribute to pollution through fertilizer runoff. One example of their ability to aid is the use of seaweed in the growth medium to trap heavy metals such as Cadmium, Nickel, and Chromium (Vijayaraghavan and Joshi 2015). Viecco et al. conducted experiments to determine dry climate deposition quantities of PM 2.5 and PM 10 on green roof and living walls. Their work determined that sedum was most effective and that such strategies can be used in arid climates to improve air quality (Viecco et al.

2018). One concern regarding the use of green roofs is the leaching of phosphates from the growth substrate into the water system as determined by Karczmarczyk et al. who recommended implementation of phosphate reduction measures, particularly in the case of widespread green roof usage (Karczmarczyk et al. 2018). This is based upon experimental data using the most industrially widespread growth substrates available.

The thermal contributions from green roofs are considered as twofold, the first being their insulatory contribution to the structure energy footprint and second, their impact on the urban heat island effect. Susca provides a climatic and structural guideline overview for decision makers with the aim to maximize green roof potential (Susca 2019). Xing et al. used an experimental setup consisting of 2 rooms, one of which incorporated a green wall, the other a standard construction, to determine that the room with the green wall reduced heating demand by holding a higher nighttime temperature indoors while reducing the exterior air temperature by 1-3 °C (Xing et al. 2019). Kim et al. modeled the urban heat island (UHI) effect across multiple climatic zones within the United States and looked at the reduction of UHI bsed upon modifying urban morphology and the inclusion of green roofs. It was determined that the inclusion of vegetated areas had a marginal impact on the urban climate and that the most effective inclusions were higher area ratios of trees and grasses in hot climates (Kim et al. 2018).

Storm water runoff reduction is widely considered the most important benefit of green roof usage, with much attention given to quantifying their impact beginning around the mid 2000s. Researchers began to quantify storm water runoff reduction of green roofs and advocate for their usage to solve the issue of urban flooding. This quantification has been split into two major categories, one of which is optimization of performance by placing them in the most exposed locations. This is accomplished by experiments and modeling of rainfall on building facades to determine optimal placement. The other strategy has been to accurately calculate water infiltration of green roof substrates and drainage layers. The work encompasses experimental setups from laboratory to *in situ* full scale testing as well as modeling ranging from 1D simple diffusion equations to fully 3D infiltration models. Further discussion of these methods in significant detail is provided in subsequent chapters as they constitute the foundation for the work presented in this thesis.

1.2 Climatic motivation

The primary motivation for the usage of green roofs as an aid to storm water management in urban environments stems from the measured increases in rainfall frequency and severity as measured in the northern climes such as that by SMHI in Sweden (Olsson et al. 2018) and Great Britain (Stovin et al. 2012). Indeed the issue is more globally widespread, with interest in Italy (Masseroni and Cislaghi 2016), Hong Kong (Wong and Jim 2014), the subcontinent (Bhatla et al. 2019), and Australia (Schreider et al. 2000). The need to address the impact of this increasing rainfall in urban storm water infrastructure begins to appear around the mid 2000s such as this report (Arisz and Burrell 2006) detailing the need for such considerations,

as well as in Vietnam (Huong and Pathirana 2013) and Denmark (Gregersen et al. 2013). It is clear that the combination of increased localized rainfall frequency and intensity driven by climate change and UHI effects and limited spatial allowances for water catchments within urban environments can be addressed to a degree by taking advantage of available rooftop space for the purpose of storm water mitigation.

1.3 Alternative technologies

It is appropriate to mention that there are alternative technologies to the traditional green roof that are in use, such as blue/gray roofs. Each design type has its own advantages and disadvantages worthy of mention. Blue/gray roofs are defined as similarly to green roofs with the important difference that no organic material is included and that they may be used to temporarily store water for domestic purposes. They can be designed to drain water using active or passive controls, with the passive control similar in theory to that of a standard green roof. Benefits of this type of roof are similar to green roofs and also include this possibility for temporary water storage as well as limited maintenance requirements due to the absence of organic material. There is also a risk of leakages in many of the types of green/blue/gray roofs, detracting from their use in some cases. They may also be employed for cooling purposes as a thermal sink however they are not capable of hosting the same level of biodiversity seen in green roofs and require additional structural considerations depending upon the dimensions of the roof.

1.4 Main goals of the thesis

There are two main goals of this thesis, each dealing with one aspect of improving the ability of green roofs to mitigate storm water. Each goal will be treated separately and the background and motivation for their investigation will be presented at the time of their respective introduction. The main goals are:

- Optimization of green roof placement on building facade to capture the most incident rainfall
- Optimization of green roof storm water mitigation by design of the growth substrate

1.4.1 Optimization of green roof placement (Paper 1)

The main goal of this section of the thesis is to improve prediction of the location on a building facade where the incident rainfall is highest given a prevailing wind. This is accomplished by extending previous computational fluid dynamics models within the field of study to include full turbulence model closures for the rainfall phases. This inclusion is tested to determine its viability and if any increase in accuracy is accomplished.

1.4.2 Optimization of green roof substrate design (Papers 2-4)

The goal of this aspect of the work is to provide increased insight into the impact of the growth substrate on storm water infiltration dynamics. This is done by applying the lattice Boltzmann method to chosen porous domains representing the growth substrate of a green roof. We identify and quantify the underlying physical phenomena responsible for transport of storm water through these porous domains and apply the observations to provide guidelines for substrate design. This is accomplished by extracting properties of the flow and the solid microstructure and linking observations with physical and mathematical formalizations.

1.5 Structure of thesis

The structure of the thesis is determined by the subject of the papers and concepts are introduced in the relevant chapters. Chapter 2 is directly related to Paper 1 and consists of a short introduction to computational fluid dynamics (CFD) and its application to the problem of improving green roof performance by their placement on a structure facade. It includes a description of the model employed as well as some of the difficulties encountered when modeling rainfall using CFD. Some results from the calculations are presented along with a discussion of the viability of the technique and thoughts on future improvements. Chapter 3 relates to Papers 2-4 and provides an introduction to concepts of soil science required to evaluate the performance of green roof runoff mitigation. It covers the formal definitions of saturation and permeability along with the introduction of Darcy's law and its extension to multiphase flow. Concepts relevant to porous media are introduced and a background of the resultant research is included. It also covers the introduction of the Boltzmann equation for particle motion present in statistical mechanics and its use in the lattice Boltzmann method to solve flows at the pore-scale within difficult geometries. The model is outlined and results based upon this method are presented and discussed in the frame of solving infiltration of soil. Work conducted on X-ray microtomographic scans of real growth substrates and the subsequent modeling of infiltration is compared to the previous cases and a reflection on future work concludes the chapter. Chapter 4 provides a quick summary of the work and some general reflections as well as wrapping up the stated goals and defining possible further investigations.

Nomenclature (Chapter 2)

b	–	Tuning parameter, raindrop distribution function
B_1	–	Tuning parameter, raindrop distribution function
B_2	–	Tuning parameter, raindrop distribution function
C_d	–	Drag coefficient
$c_{\epsilon 1}$	–	Tuning parameter, standard $k-\epsilon$ model
$c_{\epsilon 2}$	–	Tuning parameter, standard $k-\epsilon$ model
c_μ	–	Tuning parameter, standard $k-\epsilon$ model
d_{drop}	–	Droplet diameter, rain
F	–	Liquid water fraction of drops in air less than size d_{drop}
$\mathbf{f}$	–	Body force (tensor notation)
f_c	–	Coriolis force
f_h	–	Raindrop size distribution, through horizontal plane
g_i	–	Gravity
H	–	Characteristic height, structure
I	–	Rainfall intensity
I_u	–	Stream-wise turbulence intensity
k	–	Turbulent kinetic energy
L_x	–	Domain length, x-direction
L_y	–	Domain length, y-direction
L_z	–	Domain length, z-direction
m	–	Tuning parameter, raindrop distribution function
$\mathbf{n}$	–	Normal vector
p	–	Pressure
P^k	–	Production term for turbulent kinetic energy
$\overline{p_i}$	–	Time-averaged pressure
q	–	Phase number indicator
q_s	–	Rain phase turbulent profile scaling factor
R	–	Relative Reynolds number
R_h	–	Rainfall intensity, horizontal
R_{wdr}	–	Rainfall intensity, wind-driven rain
S_h	–	Event cumulative rainfall
s	–	Tuning parameter, raindrop distribution function
t	–	Time
$\mathbf{u}$	–	Velocity (tensor notation)
u_i	–	Velocity (Einstein notation)
u_r	–	Velocity, reference height

$\overline{u_i}$ – Velocity, time-averaged
$\overline{u}_q, i$ – Velocity, rain phase
u_i' – Velocity, instantaneous fluctuation
u^*_{ABL} – Friction velocity, atmospheric boundary layer
V_t – Terminal velocity, raindrop
V_n – Rain phase velocity, structure-face normal
y_G – Boundary layer depth, atmospheric boundary layer
y_r – Reference height
y_0 – Aerodynamic roughness length, atmospheric boundary layer
W – Liquid volume per volume of air
α – Power law exponent, atmospheric boundary layer
α_q – Phase volumetric fraction
$\alpha_{q,loc}$ – Phase volumetric fraction, local
δ_{ij} – Dirac delta function
η_d – Specific catch ratio, wind-driven rain
η – Catch ratio, wind-driven rain
ϵ – Dissipation of turbulent kinetic energy
κ – von Karman constant
ρ – Density
ρ_w – Density, rain phase
λ – Latitude
ϕ_{wind} – Wind direction
μ_{nw} – Dynamic viscosity, wind
ν – Kinematic viscosity
ν_{nw} – Kinematic viscosity, wind
ν_t – Turbulent kinematic viscosity
Ω – Angular velocity, Earth's rotation
σ_k – Tuning parameter, standard $k - \epsilon$ model
σ_ϵ – Tuning parameter, standard $k - \epsilon$ model

Chapter 2

Optimization of green roof placement

2.1 Brief introduction to computational fluid dynamics

Computational fluid dynamics (CFD) is a numerical methodology for solving the equations for conservation of energy, momentum and mass, primarily within the Eulerian framework (fixed-frame). It was first developed in the 1920's and progressed in complexity and scope over the century. It is used in engineering to model and solve a variety of flow-related problems as well as within animation to mimic liquid motion with greater realism. The applications within engineering range from the microscopic to the macroscopic scale with computational domains in microns to Earth's atmosphere. Due to range in scales previously mentioned it is often necessary to look at the problem on many levels of detail and gain an understanding of the most important processes at work. Turbulence for example operates on scales of the same magnitude of the computational domain to what is known as the Kolmogorov scales, wherein the turbulent energy is dissipated as heat It is a very powerful technique for examining complex multiscale problems with a controllable level of accuracy, which is determined by a variety of factors. One such controlling factor is that these computations are quite expensive in terms of computational power and the time required and thus a balance between accuracy and resource management is imperative. The great flexibility of the method and its wide range of applications have propelled the methodology to prominence within many areas of research and with the advancements made in computational power new possibilities are frequently arising.

2.2 Current state of research

The original method of calculating the quantity of wind-driven rain incident upon a building facade was developed by Choi in 1994 (Choi 1994) who employed Lagrangian particle tracking (LPT) and the concept of a stream tube The steady-state wind profile

was calculated and then trajectories for individual drops were iteratively calculated, forming a tube connecting an area of the inlet boundary to and area of the building facade. Once this was accomplished a distribution of raindrop sizes present within this stream tube were calculated and by summing their liquid contribution a quantity of rainfall on the building facade as determined. This process was consequently both time consuming and calculation-intensive as this process must be done for each unique rainfall intensity and wind direction. The amount of wind-driven rain (WDR) on each facade zone was calculated using previous research on raindrop terminal velocities classified by raindrop size and raindrop size distribution dependent on rainfall intensity (Gunn and Kinzer 1949) (Best 1950). The details of the method were formalized in 2002 by Blocken and Carmeliet (Blocken and Carmeliet 2002). These issues motivated subsequent researchers to modify the process in a variety of ways, both to increase accuracy and reduce computation requirements.

The first applications of Choi's technique that were validated against experimental data were published in 2002, 2006 and 2007 by Blocken and Carmeliet (Blocken and Carmeliet 2002) (Blocken and Carmeliet 2006) (Blocken and Carmeliet 2007). In the papers the researchers applied the method using steady-state 3D Reynolds-averaged Navier-Stokes (RANS) with standard and realizable $k - \epsilon$ turbulence models, respectively. The results of their approach were compared with experimental data gathered at the VLIET test building of the Laboratory of Buildings Physics, Katholieke Universiteit Leuven in Flanders, Belgium, with the results showing relatively good ability to predict WDR on the building facade.

The model was extended to quasi-steady state, presented in (Blocken and Carmeliet 2002). This allowed for combinations of steady-state results to be linearly interpolated to allow for results from combination that were not solved directly, creating a form of solution matrix.This improved flexibility when calculating the total rainfall impinging on a building facade under changing conditions rather than a single solution. A subsequent paper was published detailing temporal accuracy standards for applying the quasi-steady WDR technique (Blocken and Carmeliet 2008). This paper showed that weather data must be collected and properly weighed such that the data was given in 10 minute intervals.

The original models neglected the turbulent dispersion term of the raindrop phases to simplify the calculations however this was treated as a known source of error that must be addressed. In 2009 Blocken et al. tested 4 different turbulence models using the LPT approach on modeling the wind blocking effects on WDR between two buildings (Blocken, Dezsö, et al. 2009). The results showed the wind blocking effect of the buildings reduced WDR on both buildings by around 25% where the blocking was in effect. Additionally the $k - \epsilon$ model performed most poorly compared to the realizable $k - \epsilon$, RNG $k - \epsilon$ and RSM models, with the RSM model giving the most accurate results. The failure of the standard $k - \epsilon$ lay in the over-prediction of turbulent kinetic energy along the roofline, thus giving inaccurate WDR results for the rooftop. Another study was undertaken in 2009 by Akubu et al. to determine the accuracy of the LPT modeling technique on WDR with winds oblique to the building facade (Abuku et al. 2009). The model was validated against data gathered at a site in Trondheim and the results suggested the technique to be

less accurate when applied to oblique WDR than to WDR driven by wind normal to the building facade.

Huang and Li published a paper detailing the replacement of LPT with Eulerian Multiphase (EM) to model the rain phases (S. Huang and Q. Li 2010). This alteration of the method by Choi was a means of eliminating the iterative raindrop trajectory calculations. In this method the rain is divided into different phases, each with a different raindrop diameter, and each phase has a corresponding volumetric ratio in its momentum equation. The conservation of mass and momentum equations are solved for each phase however turbulent dispersion is still neglected. In 2013 Kubilay et al. used the model proposed by Huang and Li wherein the model is validated against experimental data gathered at the Hunting Lodge St. Hubertus in the Netherlands (Kubilay et al. 2013). The accuracy of the new method was found to be comparable to that attained using LPT however the computational resources were reduced significantly.

In 2014 Kubilay et al. released two papers on the application of the EM quasi-steady method to an array of cubes in close proximity to each other and to the Hunting Lodge St. Hubertus (Kubilay et al. 2014c) (Kubilay et al. 2014b). In these works the turbulent dispersion term is included and the closure of each rain phase is attained by introducing a response coefficient which determines to what degree the rain phase velocity fluctuations align with those of the wind phase. The full solution is attained by iteratively solving the rain phase equations until the desired residual values are reached and the catch ratio is calculated for the entire building facade. The results of the simulation on the cubes was validated against detailed meteorological data gathered from a site in Switzerland (Kubilay et al. 2014a). The Hunting Lodge results were compared to the previous works without the implementation of turbulent dispersion and accuracy was shown to improve slightly in this new model. An implementation of full turbulence models for the raindrop phases had not been tested previously and such an implementation is attempted in this work.

2.3 Goal of doctoral research (pt 1)

The main goal of this section of the thesis is to improve prediction of the location on a building facade where the incident rainfall is highest given a prevailing wind. This is accomplished by extending previous computational fluid dynamics models within the field of study to include full turbulence model closures for the rainfall phases. This inclusion is tested to determine its viability and if any increase in accuracy is accomplished.

2.4 Single phase mathematical model

We introduce the conservation equations of mass and momentum for incompressible Newtonian fluid flow, a specific formulation of the Navier-Stokes equations. These equations will be used to calculate the steady-state wind flow profile around a building

after some modifications. Equation 2.1 is the conservation of mass and 2.2 represents the conservation of momentum:

$$\nabla \cdot \mathbf{u} = 0, \tag{2.1}$$

$$\frac{\partial \mathbf{u}}{\partial t} + \mathbf{u} \cdot \nabla \mathbf{u} = \mathbf{f} - \frac{1}{\rho}\nabla p + \nu \nabla^2 \mathbf{u}. \tag{2.2}$$

where $\mathbf{u} = [u_1, u_2, u_3]$ is the fluid velocity, f the external body force(s) (usually gravity), ρ is the fluid density, p is the fluid pressure, and ν is the kinematic viscosity. These equations represented in Einstein notation are:

$$\frac{\partial u_i}{\partial x_i} = 0, \tag{2.3}$$

$$\frac{\partial u_i}{\partial t} + u_j \frac{\partial u_i}{\partial x_j} = f_i - \frac{1}{\rho}\frac{\partial p}{\partial x_i} + \nu \frac{\partial^2 u_i}{\partial x_j \partial x_j}. \tag{2.4}$$

The modeling of the wind profile around a building will make use of the Reynolds-Averaged Navier-Stokes (RANS) equations, thus we describe the notion of the closure problem present in time averaging the equations presented above. Time averaging equations 2.3 and 2.4 is accomplished using the decomposition in 2.5 for all variables, and applying the subsequent relations:

$$u_i = \overline{u}_i + u_i', \tag{2.5}$$

$$\overline{\overline{u}_i} = \overline{u}_i, \tag{2.6}$$

$$\overline{u_i'} = 0, \tag{2.7}$$

$$\overline{\overline{u}_i u_j'} = 0, \tag{2.8}$$

$$\overline{u_i' u_j'} \neq 0. \tag{2.9}$$

This will transform equation 2.3 and 2.4 into equations 2.10 and 2.11 however we have no conservation equation for the final term, the double correlation of the instantaneous velocities $\overline{u_i' u_j'}$, known as the Reynolds stresses. This is what is known as the closure problem, as in order to solve this quantity we must derive another transport equation for this quantity, which leads to more variables for which we have no equation. The solution to this problem is to employ turbulence modeling to close the problem and provide an equation for this term.

$$\frac{\partial \overline{u}_i}{\partial x_i} = 0, \tag{2.10}$$

$$\overline{u}_j \frac{\partial \overline{u}_i}{\partial x_j} = -\frac{1}{\rho}\frac{\partial}{\partial x_i}\overline{p} + \frac{\partial}{\partial x_j}\left[\nu\left(\frac{\partial \overline{u}_i}{\partial x_j} + \frac{\partial \overline{u}_j}{\partial x_i}\right) - \overline{u_i' u_j'}\right]. \tag{2.11}$$

2.5 Standard $k-\epsilon$ closure model

We can make use of the Boussinesq assumption:

$$\overline{u_i' u_j'} = -\nu_t\left(\frac{\partial \overline{u}_i}{\partial x_j} + \frac{\partial \overline{u}_j}{\partial x_i}\right) + \frac{2}{3}\delta_{ij}k, \tag{2.12}$$

which provides a relation between turbulent kinetic energy, the mean energy found within turbulent eddies, and the Reynolds stresses. This is accomplished by introducing an eddy viscosity $\nu_t > 0$ and was the first method by which the closure problem was addressed. Any model which uses this type of closure is known as an eddy viscosity model (EVM), of which there are many different models in use. This relation allows equations 2.10 and 2.11 to be rewritten in terms of eddy viscosity and turbulent kinetic energy k.

$$\frac{\partial \overline{u}_i}{\partial x_i} = 0, \tag{2.13}$$

$$\overline{u}_j \frac{\partial \overline{u}_i}{\partial x_j} = -\frac{1}{\rho}\frac{\partial}{\partial x_i}(\overline{p} - \frac{2}{3}\rho\delta_{ij}k) + \frac{\partial}{\partial x_j}\left[(\nu + \nu_t)\left(\frac{\partial \overline{u}_i}{\partial x_j} + \frac{\partial \overline{u}_j}{\partial x_i}\right)\right]. \tag{2.14}$$

There are many options available within eddy viscosity models, ranging from 0 equation models to multi-equation models. In this work the 2 equation standard $k-\epsilon$ model is used. This model uses modeled equations for both turbulent kinetic energy k and turbulent dissipation ϵ which must be derived from their repsective exact transport equations. This derivation is not included here but can be found in (Launder and Spalding 1974). This model is one of the most widely used and has been modified several times for specific purposes.

The modeled k equation is:

$$\frac{\partial k}{\partial t} + \overline{u}_j \frac{\partial k}{\partial x_j} = P^k + \frac{\partial}{\partial x_j}\left[\left(\nu + \frac{\nu_t}{\sigma_k}\right)\frac{\partial k}{\partial x_j}\right] - \epsilon, \tag{2.15}$$

where P^k is the production term for the turbulent kinetic energy:

$$P^k = \nu_t \left(\frac{\partial \overline{u}_i}{\partial x_j} + \frac{\partial \overline{u}_j}{\partial x_i}\right)\frac{\partial \overline{u}_i}{\partial x_j}. \tag{2.16}$$

We define a transport equation for the modeled dissipation of turbulent kinetic energy ϵ, which represents the dissipation of kinetic energy from the smallest eddies and is assumed to be isotropic.

$$\frac{\partial \epsilon}{\partial t} + \overline{u}_j \frac{\partial \epsilon}{\partial x_j} = \frac{\epsilon}{k} c_{\epsilon 1} P^k + \frac{\partial}{\partial x_j}\left[\left(\nu + \frac{\nu_t}{\sigma_\epsilon}\right)\frac{\partial \epsilon}{\partial x_j}\right] - c_{\epsilon 2}\frac{\epsilon^2}{k}. \tag{2.17}$$

Note that several tuning parameters are required for this model which are provided below.

$$\nu_t = c_\mu \frac{k^2}{\epsilon}, \tag{2.18}$$

$$c_\mu = 0.09, \tag{2.19}$$

$$\sigma_k = 1.0, \tag{2.20}$$

$$\sigma_\epsilon = 1.3, \tag{2.21}$$

$$c_{\epsilon 1} = 1.44, \tag{2.22}$$

$$c_{\epsilon 2} = 1.92. \tag{2.23}$$

The standard $k-\epsilon$ model requires wall functions which act to improve the accuracy of the model near the boundaries, particularly in the viscous boundary layer. This is to aid in the solution of the known issue of this model to over-predict turbulent kinetic energy near boundaries. The ones used here are taken from the model creators Launder & Spalding (Launder and Spalding 1974).

2.6 Multiphase extension

The solution of the wind-driven rain requires the extension of the equations presented above to multiple phases and the temporal domain. Once the solution of the wind phase has been generated the rain phases are introduced. The transient incompressible equations of mass and momentum conservation for the additional phases, representing varying raindrop sizes, are given by:

$$\frac{\partial(\rho_w \alpha_q)}{\partial t} + \frac{\partial(\rho_w \alpha_q \overline{u}_{q,j})}{\partial x_j} = 0, \tag{2.24}$$

$$\frac{\partial(\rho_w \alpha_q \overline{u}_{q,i})}{\partial t} + \frac{\partial(\rho_w \alpha_q \overline{u}_{q,i} \overline{u}_{q,j})}{\partial x_j} + \frac{\partial(\rho_w \alpha_q \overline{u'_{q,i} u'_{q,j}})}{\partial x_j} = \rho_w \alpha_q g_i + \rho_w \alpha_q \frac{3\mu_{nw}}{(\rho_w d_{drop})^2} \frac{C_d R}{4} (\overline{u}_i - \overline{u}_{q,i}), \tag{2.25}$$

$$\alpha_1 + \sum_{q=2+} = 1, \tag{2.26}$$

where α_q is the volume fraction of qth rain phase, $\overline{u}_{q,i}$ the ith velocity component of qth rain phase, $\overline{u}_i$ the wind velocity component, ρ_w raindrop density, C_d raindrop drag coefficient and R the relative Reynolds number. The pressure and diffusion terms have been removed from the wind phase representation however several new terms are added. A term representing the wind's influence on the rain (the drag force) is added along with the gravitational body force.

$$R = \frac{d_{drop}}{\nu_{nw}} ||\mathbf{u} - \mathbf{u}_q||, \tag{2.27}$$

where d_{drop} is the raindrop diameter. Each phase is closed using the same EVM, the standard $k-\epsilon$ model. It is to be noted that while the wind phase contributes to the motion of the raindrop phases via the drag term, the raindrop phases do not have any effect on the wind phase, known as one-way coupling. This formulation is considered acceptable when one considers the volumetric fractions each rain phase occupies.

2.6.1 Rain phase turbulent closure

The closure model for the rain phase turbulent quantities is phase-specific, meaning that each phase is closed individually and there is no transport of turbulent kinetic

energy and dissipation between the phases, or any mixing model approach. The equations are:

$$\frac{\partial k_q}{\partial t} + \overline{u}_{q,j}\frac{\partial k_q}{\partial x_j} = P_q^k + \frac{\partial}{\partial x_j}\left[\left(\nu_q + \frac{\nu_{q,t}}{\sigma_k}\right)\frac{\partial k_q}{\partial x_j}\right] - \epsilon_q, \tag{2.28}$$

for each individual phase q.

$$P_q^k = \nu_{q,t}\left(\frac{\partial \overline{u}_{q,i}}{\partial x_j} + \frac{\partial \overline{u}_{q,j}}{\partial x_i}\right)\frac{\partial \overline{u}_{q,i}}{\partial x_j}. \tag{2.29}$$

$$\frac{\partial \epsilon_q}{\partial t} + \overline{u}_{q,j}\frac{\partial \epsilon_q}{\partial x_j} = \frac{\epsilon_q}{k_q}c_{\epsilon 1}P_q^k + \frac{\partial}{\partial x_j}\left[\left(\nu_q + \frac{\nu_{q,t}}{\sigma_\epsilon}\right)\frac{\partial \epsilon_q}{\partial x_j}\right] - c_{\epsilon 2}\frac{\epsilon_q^2}{k_q}. \tag{2.30}$$

While it is possible to set the constants for each phase individually, they are kept identical however repeated here for clarity. The only modification is to the definition of the turbulent viscosity for each phase.

$$\nu_{q,t} = c_\mu \frac{k_q^2}{\epsilon_q}, \tag{2.31}$$

$$c_\mu = 0.09, \tag{2.32}$$

$$\sigma_k = 1.0, \tag{2.33}$$

$$\sigma_\epsilon = 1.3, \tag{2.34}$$

$$c_{\epsilon 1} = 1.44, \tag{2.35}$$

$$c_{\epsilon 2} = 1.92. \tag{2.36}$$

2.7 Boundary conditions

The boundary conditions for the phases are defined such that a level of similarity between the different phases is present. This was enforced due to issues encountered in the initialization of the simulations, which will be discussed in more detail later.

Boundary conditions - wind

The inlet profile of the mean wind speed is given by the atmospheric flow log-law expression

$$u(y) = \frac{u^*_{ABL}}{\kappa}\ln\left(\frac{y + y_0}{y_0}\right), \tag{2.37}$$

where u^*_{ABL} and y_0 are the fitted values for the atmospheric boundary layer (ABL) friction velocity and aerodynamic roughness length, respectively, and $\kappa = 0.42$ is the von Kármán constant. The turbulent quantities are also calculated using atmospheric flow profiles

$$k(y) = 1.5(I_u u(y))^2, \tag{2.38}$$

$$\epsilon(y) = \frac{(u^*_{ABL})^3}{\kappa(y + y_0)}, \tag{2.39}$$

$$I_u = 0.3, \tag{2.40}$$

where I_u is the stream-wise turbulence intensity. In this case because our domain does not extend significantly vertically in terms of general ABL computation we can assume it is constant. In domains spanning several hundred meters in the vertical direction a more elaborate approach is used.

$$k(y) = (I_u(y)u(y))^2, \tag{2.41}$$

$$\epsilon(y) = C_\mu^{1/2} k(y) \frac{u_r}{y_r} \alpha \left(\frac{y}{y_r}\right)^{(\alpha-1)}, \tag{2.42}$$

$$I_u(y) = 0.1 \left(\frac{y}{y_G}\right)^{(-\alpha-0.05)}, \tag{2.43}$$

$$y_G = \frac{u^*_{ABL}}{6 f_c}, \tag{2.44}$$

$$f_c = 2\Omega \sin(\lambda), \tag{2.45}$$

where α is the power law exponent, y_G is the boundary layer depth, f is the Coriolis force, Ω is the angular velocity of Earth's rotation and λ is the latitude of interest. This set of equations is recommended by (Tominaga et al. 2008). Many approaches exist for approximating atmospheric inlet conditions and more information can be found in (Q.-s. Yang and J. Zhang 2009) (Richards and Hoxey 1993) (Y. Yang et al. 2009). The aerodynamic roughness length is chosen corresponding to the sand-grain roughness height as in (Nikuradse 1933). The complete boundary condition overview is given in Table 2.1.

Boundary	Type	Parameters
Inlet	Velocity	$u_x = u_x(y)$, $u_y = 0$, $u_z = u_z(y)$
Outlet	Zero gradient	$\nabla\theta = 0$
Ground	Wall	$u = 0$, $\nabla \mathbf{u} \cdot \mathbf{n} = 0$
Building	Wall	$u = 0$, $\nabla \mathbf{u} \cdot \mathbf{n} = 0$
Top	Velocity	$u_x = u_x(y_{max})$, $u_y = 0$, $u_z = u_z(y_{max})$
Sides	Symmetry	

Table 2.1: Wind phase boundary conditions.

Boundary conditions - rain

The raindrop phases are defined in a similar fashion to the wind phase with the notable inclusion of the volumetric ratio α_q and raindrop terminal velocity $V_t(q)$ on the inlet and top boundaries. The remaining boundaries use the same conditions as previously stated for the wind phase. The specifics are given in Table 2.2. It is worth noting that we have chosen to implement no-slip conditions on the walls for the rain phases which is not realistic and may be a source of error. This choice requires the raindrop velocities to be measured away from the walls rather than directly at the interface and is discussed in more detail later in the text.

Boundary	Type	Parameters
Inlet	Phase velocity	$u_{x,q} = u_{x,q}(y)$, $u_{y,q} = -V_t(q)$, $u_{z,q} = u_{z,q}(y)$
	Phase volumetric ratio	α_q
Outlet	Zero gradient	$\nabla\theta = 0$
Ground	Wall	$u_q = 0$, $\nabla u_q \cdot n = 0$
Building	Wall	$u_q = 0$, $\nabla u_q \cdot n = 0$
Top	Phase velocity	$u_{x,q} = u_{x,q}(y_{max})$, $u_{y,q} = -V_t(q)$, $u_{z,q} = u_{z,q}(y_{max})$
	Phase volumetric ratio	α_q
Sides	Symmetry	

Table 2.2: Rain phase boundary conditions.

The turbulent quantity boundary conditions for the rainfall phases were initialized in a similar manner to the wind phase, the assumption being that this would reduce numerical instability, particularly when larger number of phases were included. The boundary condition equations are:

$$k_q(y) = q_s 1.5(I_u u_q(y))^2, \tag{2.46}$$

$$\epsilon_q(y) = \frac{(q_s u^*_{ABL})^3}{\kappa(y + y_0)} \tag{2.47}$$

$$I_u = 0.3, \tag{2.48}$$

where the scaling factor q_s is added to adjust the intensity for both quantities. Several iterations were tested using this approach and q_s was ultimately left at 1. This particular implementation was chosen given the extremely low volumetric ratios involved with the acknowledgment that this approach may be inaccurate. No additional investigations were undertaken to determine the validity of such an assumption and remains a significant candidate for possible sources of error in the reported results.

2.8 Simulations

2.8.1 Domain discretization

While the theoretical framework has been introduced it is still necessary to provide information regarding the setup of the simulations, beginning with the domain determination and mesh generation. The computational domains were constructed using ANSYS ICEM, with the dimensions being chosen for each individual case to adhere to best practices in atmospheric boundary layer flow modeling. These regulations stipulate that the domain must be proportioned based upon a chosen characteristic length, in our case the building height. Figure 2.1 displays Case 2 and 2.2 shows Case 3, with their characteristic heights $H = 2$ and $H = 58$, respectively. Case 1 is not pictured but the structure is the same as in Case 2, the array of cubes. The domain dimensions are modified for Case 2 to account for a different wind

direction. The domain dimensions are determined by the requirements to ensure an accurate atmospheric boundary layer inlet profile as well as outflow length for undisturbed flow. The blockage factor of the constructions is less than 1% in the streamwise direction.

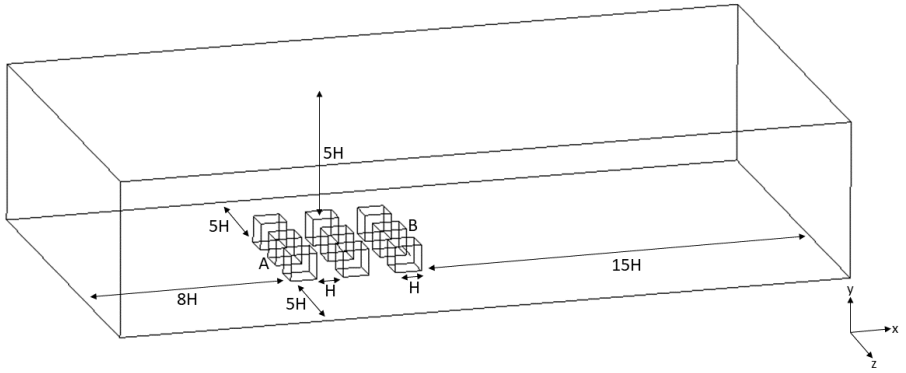

Figure 2.1: Cube array domain (Case 2).

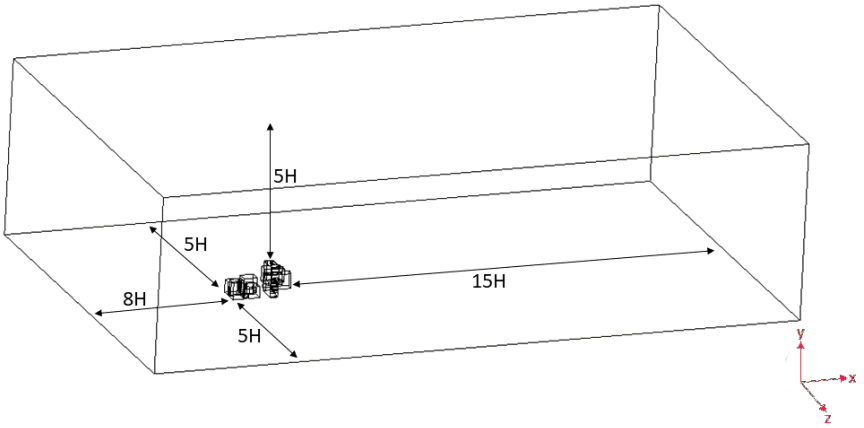

Figure 2.2: Full-scale building domain (Case 3).

The domains are discretized using structured hexaherdal elements following practice methods These require the computational mesh to adhere as best as possible to having a Courant-Friedrichs-Lewy (CFL) condition around 1, which is a requirement for explicit time stepping methods to ensure numerical stability. In addition the expansion ratio from one adjacent element to another must not exceed 1.2 and the aspect ratio of the elements are limited to prevent numerical divergence from arising. This process results in the meshing characteristics presented in Table 2.3.

The meshing for the structures used in Cases 1,2, and 3 are presented in Figure 2.3 to give a visual representation of the discretization. The number of elements in Case 1 is 2,498,109; Case 2 consists of 1,013,249 elements; and Case 3 has 14,341,622.

Length [m]	H	L_x	L_y	L_z	Δx_{min}	Δy_{min}	Δz_{min}	Δt [s]
Case 1	2.0	56.0	12.0	56.0	0.0296	0.0089	0.0296	0.001
Case 2	2.0	56.0	12.0	30.0	0.1184	0.0089	0.0296	0.005
Case 3	58.0	1288.13	348.0	783.2	0.03	0.012	0.012	0.0025

Table 2.3: Domain dimenions and discretization.

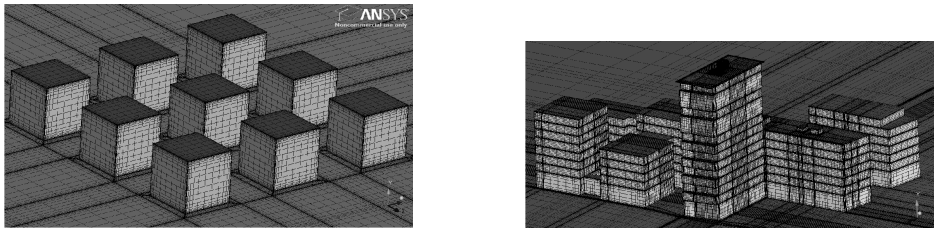

(a) Cube array discretization close-up. (b) Full-scale building discretization close-up.

Figure 2.3: Structure meshing in Ansys ICEM.

2.8.2 Simulation parameters

Solver and convergence criteria

The commercial software AVL FIRE was used to calculate the solutions for cases 1-3 using the appropriate input parameters defined below. The simulations are run in two stages. First the solution of the steady-state wind profile is calculated. In the second stage the wind profile solution is used as the initialization for the transient wind phase whereas the raindrop phases are defined using the parameters given in Table 2.5. The semi-implicit method for pressure-linked equations (SIMPLE) solver is used, though modified to the SIMPLE-PISO solver for the multiphase transient solution. Convergence is determined using residuals set at 10^{-6} and for the rain phases local convergence of the velocity and volumetric fraction profiles are monitored in the areas of interest.

Wind inlet profile

The wind profile generated by equation 2.37 is matched to experimental data of wind velocities at variable heights. For Cases 1 and 2 this data is obtained from experimental data of a rain event gathered by Kubilay et al. (Kubilay et al. 2014a) and undertaken at Swiss Federal Laboratories for Materials Science and Technology (EMPA) in Dübendorf, Switzerland, latitude 47°24′9″N and longitude 83°6′50″E. This experiment consisted of 9 cubes set in an array spaced two meters apart and with each cube measuring two meters of length. Wind velocities were measured by an 3D ultrasonic anemometer on a mast 8.4 meters high, located near the cubes and 2 cup anemometers at heights 2.4 and 5.4 meters high. Horizontal rainfall intensity was measured using a tipping bucket at a frequency of 1 Hz and data is subsequently averaged over a period 10 minutes. The inlet profiles for case 3 are taken from meteorological data from SMHI at the appropriate location in Gothenburg Sweden.

	ϕ_{wind}	$u(2.4)$	$u(5.4)$	$u(8.4)$	R_h [mm/h]	S_h [mm]	t [min]
Case 1	229.017	2.12	2.62	2.75	20.0	3.331	140
Case 2	270.151	0.54	0.96	1.38	7.10	1.18	300
	ϕ_{wind}	$u(10.0)$	$u(30.0)$		R_h [mm/h]		
Case 3	163.0	7.5	15.4		3.0		

Table 2.4: Experimental weather data for inlet profile generation.

The wind direction and rainfall intensities are chosen to match representative weather conditions taken as an annual average value.

Rain phase distributions

Each rain phase is determined by the droplet diameter d_{drop} and its corresponding terminal velocity V_t. The droplet diameter itself is a representative value for a range of droplet sizes with a given probability of occurrence in a particular rainfall intensity. This can be formalized by the equations developed by Best in 1950 (Best 1950) and is an empirical fitting to experimental data and previous research by Gunn & Kinzer in 1949 (Gunn and Kinzer 1949) wherein the distribution is:

$$F = 1 - exp\left[-\left(\frac{d_{drop}}{a}\right)^m\right], \tag{2.49}$$

$$a = B_1 I^s, \tag{2.50}$$

$$W = B_2 I^b, \tag{2.51}$$

$$f(d_{drop}) = F(d_{drop} + \delta d_{drop}) - F(d_{drop}), \tag{2.52}$$

where F is the fraction of liquid water in the air with drops of diameter less than d_{drop} [mm], I [mm/hr] is the rainfall intensity, W [mm^3/m^3] is the amount of liquid water per unit volume of air and the other variables are constants with values

$$\begin{aligned} B_1 &= 1.30, \\ B_2 &= 67, \\ s &= 0.232, \\ b &= 0.846, \\ m &= 2.25. \end{aligned}$$

The probability distribution $f(d_{drop})$ of water in the air with drops of diameter d_{drop} to $d_{drop} + \delta d_{drop}$ gives the distribution in a volume of air, however due to differences in terminal velocity of each drop size we must convert this to distribution through a horizontal plane. This conversion is accomplished by:

$$f_h(d_{drop}) = \frac{f(d_{drop})V_t(d_{drop})}{\int_{d_{drop}} f(d_{drop})V_t(d_{drop})\mathrm{d}d_{drop}}, \tag{2.53}$$

where $f_h(d_{drop})$ is the raindrop distribution through a horizontal plane. The phasic volumetric ratios can be directly taken from the probability distribution function

$f(d_{drop})$ once the assumption of a maximum raindrop diameter is determined. The distribution can be modified by the chosen number of raindrop phases. In this work two distributions were tested for Case 2 however difficulties were encountered in the stability of such simulations, a topic which is discussed in section 2.9.2. The distributions for the rainfall phases are given in Table 2.5; Case 3 is not included as no distribution tested provided satisfactory results. The number of phases limits the accuracy of the results, particularly for smaller droplet sizes as they are more influenced by the wind phase. There is a trade-off between increasing the number of phases and therefore result accuracy and computational efficiency. In the cases discussed here the raindrop sizes were chosen to reflect a equal distribution of the full raindrop size spectrum. This spectrum is dependent upon the rainfall intensity, which explains why the chosen raindrop sizes for Case 1 and 2 differ slightly. It should be noted that for raindrops with diameter in the range of $0.5 - 20$ μm the continuum assumption is not valid and the application of the Navier-Stokes to model their behavior can produce erroneous results (Beard 1976).

Case 1				Case 2		
q	α_q	d_{drop}	V_t	α_q	d_{drop}	V_t
1	0.9999992697	-	-	0.9999997142	-	-
2	2.612×10^{-7}	1.8	6.09	7.50×10^{-8}	1.2	4.64
3	2.915×10^{-7}	3.0	8.06	1.020×10^{-7}	2.0	6.49
4	1.775×10^{-7}	5.0	9.09	1.088×10^{-7}	4.0	8.83

Table 2.5: Rain phase technical information.

2.8.3 Results and discussion

Wind profile solutions

The steady-state wind profile solutions are taken after convergence as determined by the residuals for the conservation equations reaches 10^{-6} and the results are plotted for Cases 2 and 3 in Figure 2.4 and 2.5. While the results capture larger recirculation zones where the atmospheric wind profile impinges upon the structures it is to be noted that the velocities are likely to be artificially high due to the over-prediction of turbulent kinetic energy by the use of the standard $k - \epsilon$ turbulence model. This issue is treated in more detail in section 2.9. In Figure 2.4a we see the profile of the wind flow at height 1 meter from the ground as seen from above. The wind is traveling from left to right. We see an increase in velocity when the wind hits the cubes and flows around and over them, leaving areas of lower velocity in between the cubes. In this region the wind flows in a somewhat circular pattern, as evidenced by the arrows in both 2.4 (a) and (b). It is in these areas where the wind-driven rain will likely hit the sides of the cubes. The majority of the flow is uninterrupted ,though the velocity on the leeward side of the cube array is lowered slightly. In the channels between the cubes in line with direction of flow we see an increased velocity due to the compression of the wind between the rows and subsequent expansion after

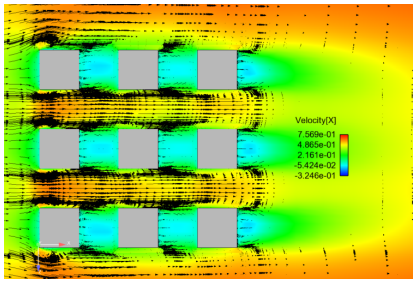

(a) Wind velocity, (cut at y=1.0).

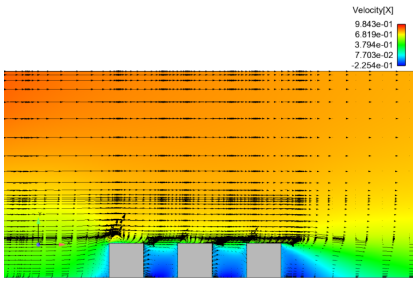

(b) Wind velocity, (cut at z=0.0).

Figure 2.4: Velocity profiles cut along equidistant planes with regard to cube array.

each cube. Due to these patterns we expect to see coverage on both the windward and leeward faces of the cubes, decreasing towards the ground, though the majority of the rainfall will be collected by the tops of the cubes.

We see similar occurrences in Figure 2.5 with increased velocities when the wind is compressed between buildings or upon its incidence to the building facades. Once again we see regions where the flow recirculates, allowing for higher rates of incident rainfall on leeward or otherwise facing parts of the buildings. We see a much higher blocking effect upon the wind by the full size structures which is to be expected as they are no aligned with the direction of wind flow and thus disturb the atmospheric flow to a greater extent.

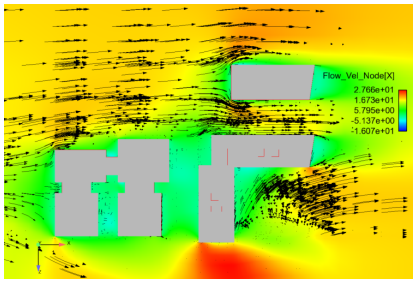

(a) Velocity profile, (x = 18.0).

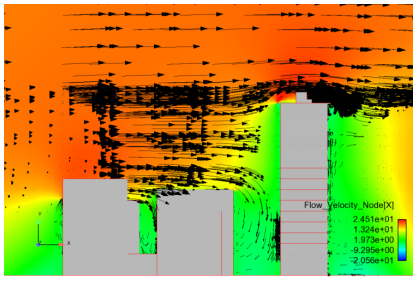

(b) Velocity profile, (z=54.0).

Figure 2.5: Velocity profiles along central planes with regard to primary structure.

Calculating wind-driven rain catch ratio

The quantity of wind-driven rain on a building facade is calculated for each phase and a sum total of all rain phases: the specific catch ratio and catch ratio as defined in equations 2.54 and 2.55, respectively. Note that the calculated field variables required for this calculation are the local volumetric ratio of each rain phase and their corresponding local velocities.

$$\eta_{d_{drop}}(q) = \frac{R_{wdr}(q)}{R_h(q)} = \frac{\alpha_{q,loc}|V_n(q)|}{R_h f_h(q)} \left(\frac{3600}{1 \times 10^{-3}}\right), \tag{2.54}$$

$$\eta = \int_{d_{drop}} f_h(R_h, d_{drop})\eta_d \mathrm{d}d_{drop}, \tag{2.55}$$

where R_{wdr} is the WDR intensity, R_h the horizontal rainfall intensity, $f_h(R_h, d_{drop})$ the raindrop size distribution through a horizontal plane and $|V_n(q)|$ the rain phase velocity magnitude normal to the building facade.

Rain phase velocity and catch ratio solutions

The rain phase velocities are taken at the boundary as close to the facade as possible and spatially averaged over a small region in the vicinity to prevent influence of any local numerical anomalies. This process is controlled directly and the area over which the averaging takes place can be modified such that the accuracy of the result can be verified to a reasonable degree. This method of evaluation for the facade-normal velocity component is also used to determine the values for the local volumetric ratio of each phase. The phase velocities vary significantly depending upon droplet diameter and this variation can be seen in Figures 2.6, where the streamlines of chosen phases are plotted for Case 2.

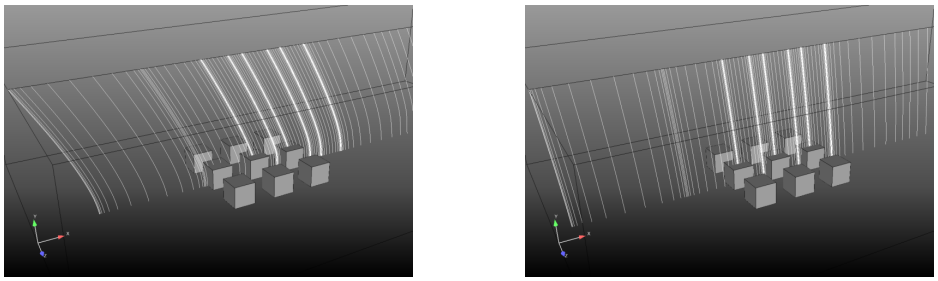

(a) Example rain phase streamlines, $d_{drop} = 1.2$ (Case 2).

(b) Example rain phase streamlines, $d_{drop} = 4.0$ (Case 2).

Figure 2.6: Rainfall streamlines for selected phases (Case 2).

The catch ratios are presented in Table 2.6 and the locations of the results ae shown in Figure 2.7, with Cube A and Cube B being the windward faces of the cubes designated in Figure 2.1. The results for the each of the cubes is compared to experimental results from Kubilay et al (Kubilay et al. 2014a) and the error difference is presented in Table 2.7.

The errors show that while the use of a turbulence model can produce accurate results in some sections of the cubes, there is still a large issue overall. The extremities are not well predicted, which can be due to the choice of turbulence model. The errors range from 5 to 70 % with little predictability in terms of location or systemic nature. More validation cases are required to draw any conclusions on this particular lack of accuracy. While we can reach low error values we cannot conclude that the model is more accurate than previous models, and indeed if one considers the additional computational component required for implementing a full turbulence model this method leaves room for improvement. We examine a few sources of difficulty in the methodology in more more detail in the following section.

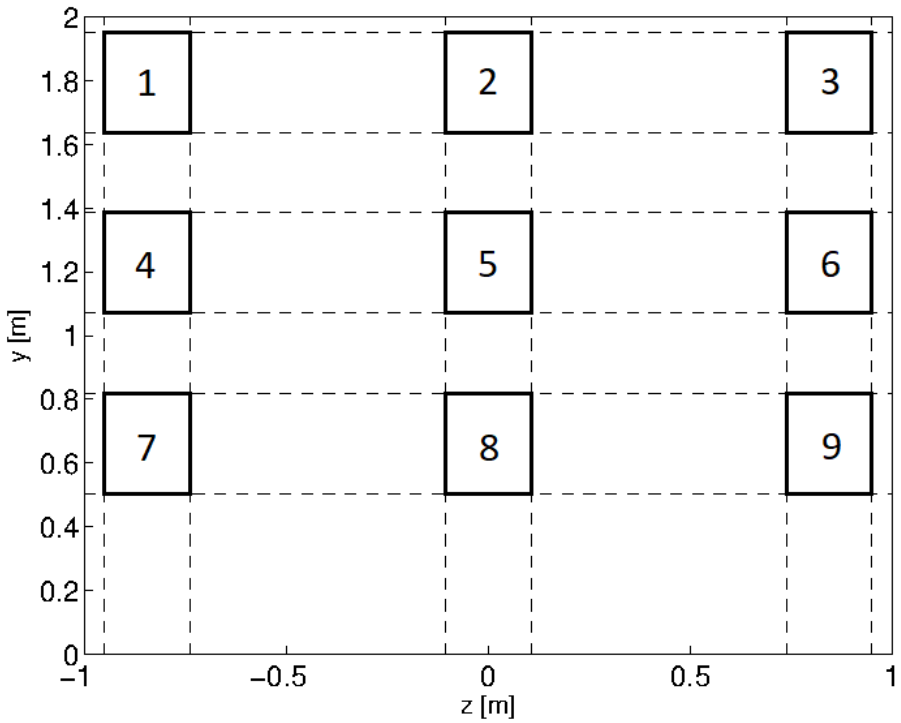

Figure 2.7: Sampling locations on the windward face of Cube A and B, numbers correspond to values in Table 2.6 and 2.7.

	Simulation				Experimental			
Point	Cube A		Cube B		Cube A		Cube B	
	Case 1	Case 2	Case 1	Case 2	Case 1	Case 2	Case 1	Case 2
1	0.20	0.08	0.21	0.07	0.29	0.15	0.28	0.17
2	0.24	0.08	0.20	0.05	0.28	0.18	0.00	0.00
3	0.20	0.06	0.22	0.07	0.28	0.22	0.29	0.17
4	0.20	0.12	0.17	0.09	0.25	0.14	0.00	0.00
5	0.21	0.12	0.18	0.08	0.24	0.14	0.24	0.13
6	0.20	0.12	0.15	0.07	0.27	0.14	0.25	0.16
7	0.21	0.05	0.16	0.09	0.23	0.14	0.18	0.10
8	0.21	0.06	0.18	0.07	0.22	0.12	0.21	0.14
9	0.17	0.07	0.17	0.10	0.27	0.15	0.24	0.12

Table 2.6: Summary of catch ratios for cases 1 and 2.

2.9 Difficulties

Several difficulties were encountered during this investigation that are worth a small discussion as the implications for future investigation are not insignificant.

Location	Cube A		Cube B	
	Case 1	Case 2	Case 1	Case 2
1	31.9	45.8	23.6	61.8
2	15.7	56.0	NA	NA
3	30.0	71.5	23.4	55.8
4	21.0	9.2	NA	NA
5	13.4	17.0	22.5	40.1
6	28.0	14.4	39.3	57.6
7	9.6	62.4	10.8	12.6
8	5.1	46.7	17.5	47.0
9	37.4	53.3	26.6	14.6

Table 2.7: Summary of errors [%] for cases 1 and 2.

2.9.1 Turbulence model choice

Originally the model of choice to solve this problem was partially-averaged Navier-Stokes (PANS), which is a newer alternative to the more traditional RANS model however it presented several insurmountable challenges in the course of its implementation. While the chosen software was capable of solving the PANS model the extension to multiphase for the rainfall resulted in almost immediate divergences. This issue was investigated for some time, leading to the conclusion that the differences required in the boundary condition implementation was destabilizing the convergence and thus a return to the more traditional RANS approach was chosen.

2.9.2 Rain phase volumetric fraction choice

The implementation of the rain phases presented another challenge in the form of the very low volumetric fractions and their implementation in a continuum (Eulerian) framework. In the past the rain phases were solved by applying Lagrangian particle tracking (LPT) to individual particles or particle packages introduced in a steady-state wind profile however the iterative calculations were computationally expensive. In the Eulerian framework the calculations are in theory reduced by solving all phases as a continuous fluid. The very low volumetric fractions assigned to each phase resulted once again in quick divergence of the simulations as the threshold tolerance for phase presence in a computational cell was of the same magnitude as the initialized phase volumetric fractions. A modification from 7 rainfall phases to 3 was implemented to increase the ratios of each phase and prevent this problem; with the sacrifice of a less accurate raindrop distribution.

2.9.3 Turbulent quantity initialization

The initialization of the turbulent quantities also presented a small challenge as if the rain phases were assigned minimal turbulent kinetic energy a divergence was almost instantaneous however if they were assigned a similar value to that of the wind phase boundary condition divergence also occurred. It was necessary to impart

a value between these extremes and monitor the evolution of the turbulent kinetic energy and dissipation in order to prevent divergences however the reduction in phase quantity also alleviated this issue. It is therefore worth nothing that when solving this problem in an Eulerian framework careful thought must be put into choice of turbulent quantities and how best to initialize them for the rainfall phases. Another option to avoid the issue is to simply neglect the turbulent dispersion term in the flow equations, however this term has been found to be significant, particularly in close proximity to the building facades.

2.10 Conclusions and Future Work

As has been stated previously in the difficulties section there are a myriad of complications that need to be addressed before I can recommend the use of full turbulent close models with this methodology. These can be solved I am certain but the question is at what level of detail we are comfortable with the resultant accuracy. There is currently no use for small-scale green roofs for the mitigation of rainfall and their placement is likely subject to constraints on the building, whether it is newly constructed or retrofitted to include such a roof design. If we require simply a guideline for placement then maybe this level of detail is not required and we are simply over-complicating the problem with little gain, particularly when we point out that each solution is valid for a single wind direction and rainfall intensity. If this kind of model is extended to fully transient solutions over long periods of time I have a strong feeling the issues discussed prior will become even more troublesome to the point that little progress will be achieved for the exponential increase in computational requirements. It is with these considerations in mind that I have decided to leave this particular investigation at this point of completion and instead focus on the second goal of the doctoral work, that of optimization of the growth substrate by design.

Nomenclature (Chapter 3)

A_lg	–	Interfacial area
$\mathscr{A}_{r_1r_2}$	–	Lattice particle scattering matrix
$\vec{c}_r$	–	Lattice node connection vectors
c_s	–	Speed of sound coefficient
$\mathscr{C}$	–	Boltzmann collision operator
d	–	Particle diameter
d_{eff}	–	Particle effective diameter
e	–	Energy
e_p	–	Particle conversion coefficient
F	–	Helmholtz free energy
F_r	–	Body force
F_{sc}	–	Shan-Chen gas-liquid interaction force
$\vec{F}$	–	External force term
f	–	Density distribution function
f_r^{eq}	–	Equilibrium probability density function
f_r	–	Spatial and temporal mean of occupancy number
$\hat{f}$	–	Post-collision probability density function
G	–	Inter-phasic interaction strength
$\mathbf{g}$	–	Gravity, vector
g	–	Gravity, scalar
$\vec{g}$	–	Relative velocity between particles
H	–	Porous media height
h	–	Standing water height
h^*	–	Standing water height, dimensionless
I	–	Particle collision differential cross-section
$\mathbf{K}$	–	Permeability (tensor)
$\mathbf{K}_\omega$	–	Permeability, phasic (tensor)
K	–	Permeability, scalar
K^*	–	Permeability, dimensionless
$\mathbf{k}_{rw,rnw}$	–	Relative permeability (tensor), wetting, non-wetting phase
$k_{rw,rnw}$	–	Relative permeability (scalar), wetting, non-wetting phase
L	–	Porous domain length, transverse
L_T	–	Full domain length
M	–	Mass
m	–	Fitting coefficient, VGM
N	–	number of particles
n	–	Fitting coefficient, VGM
n_r	–	Lattice occupancy number

p – Pressure
$\vec{p}$ – Phase space momenta
p_c – Capillary pressure
$p_{c,eff}$ – Capillary pressure, effective
p_g – Pressure scaling value, VGM
p_{nw} – Pressure, non-wetting phase
p_w – Pressure, wetting phase
q – Fitting coefficient, VGM
R_r – Spatial and temporal probability density function total fluctuations
r_{eff} – Effective pore radius
r_r – Spatial and temporal probability density function fluctuations
Sat – Saturation
S_e – Effective saturation
$\mathscr{S}$ – Boltzmann streaming operator
t – Time
t^* – Time, dimensionless
$\overline{U}_z$ – Mean vertical velocity
$\mathbf{u}$ – Velocity
$\mathbf{u}_{eq}$ – Velocity for defining equilibrium distribution function
$\mathbf{u}_\omega$ – Phasic velocity
u_c – Pore-scale characteristic velocity
V – Volume
V_{total} – Volume, total
V_{void} – Volume, void (air)
V_{wet} – Volume, wetting phase
$\vec{v}$ – Phase space velocity
$\mathbf{v}_\omega$ – Phasic velocity, Darcy
W – Work
w_p – Cementation coefficient
w_r – Weighting parameter, LBM
$\vec{x}$ – Phase space positional coordinates
α_ω – Volumetric fraction, phasic
Δ_w – Surplus density parameter
ϵ – Porosity
γ – Surface tension
κ – Hydraulic conductivity
κ_r – Equivalent relative hydraulic conductivity
κ_s – Saturated hydraulic conductivity
μ_{nw} – Dynamic viscosity, non-wetting phase
μ_w – Dynamic viscosity, wetting phase
ν – Kinematic viscosity
ν_{nw} – Kinematic viscosity, non-wetting phase
ν_w – Kinematic viscosity, wetting phase
ϕ – Packing parameter
ρ – Density
ρ_{nw} – Density, non-wetting phase
ρ_w – Density, wetting phase

ρ_{wall}	–	Contact angle, equiv. to θ_c
τ	–	Relaxation time coefficient
θ	–	Volumetric water content
θ_c	–	Contact angle, equiv. to ρ_{wall}
θ_r	–	Residual volumetric water content
θ_s	–	Saturated volumetric water content
Ψ	–	Density-dependent pseudo-potential function
$\omega = w, nw$	–	Phase variable (wetting, non-wetting)
Ω	–	Particle collision characteristic angle
Bo	–	Bond number
Ca_c	–	Pore-scale characteristic capillary number
Ca_{eff}	–	Effective capillary number
Ca_g	–	Gas capillary number
Re	–	Reynolds number

Chapter 3

Optimization of green roof growth substrate

Before evaluation of the performance of a green roof growth substrate is presented it is necessary to introduce the concept of subsurface flow and how the phenomenon can be mathematically modeled. Discussion of subsurface flow requires a precise definition: subsurface flow is a term given to liquid transport beneath the Earth's surface. In particular we are interested in the transport of liquid through packed soils exhibiting open volumes within their structure, a material known as a porous medium. This can be any material with the capacity to transport a liquid within a porous network such as a sponge, concrete, and for the purposes of this work, a soil. The field of hydrogeology encompasses the study of liquid transport in soils and makes use of several mathematical formalization for the modeling of this process.

3.1 Concepts in hydrogeology

3.1.1 Porosity

Porosity is the measure of free volume (or void space) within the solid matrix that can be filled with a liquid. Mathematically porosity is a dimensionless quantity defined as the ratio of void space over the total volume present:

$$\epsilon = \frac{V_{void}}{V_{total}}. \tag{3.1}$$

Porosity can be experimentally determined by weighing a porous medium of finite volume and subsequently wetting it until all air is removed. Once saturated it is weighed again and the difference in weights can be used to determine the quantity of water present in the volume and consequently the porosity of the solid matrix.

3.1.2 Permeability

Permeability **K** is a measure of the soil's ability to transport a fluid (or gas) within its porous microstructure and takes into account pore structure and connectivity

of air pockets. Its value can vary drastically from $10^{-7} - 10^{-11}$ m^2 for gravels and sands down to 10^{-19} m^2 for granite, limestone and clays. It is usually measured experimentally by measuring infiltration lengths over a period of time or by the changing weight of a porous volume over a given time. It is very important here to note that when we refer to permeability here we are referring to *intrinsic* permeability, a direct property of the porous material. This distinction is important as there is also the concept of *relative* permeability $\mathbf{k}_{rw,rnw}$ which is used in porous media flows with more than one liquid phase and is a measure of the effect of one such phase on another with regard to ease of infiltration.

3.1.3 Water content and Saturation

Water content is the measure of wetting phase (or water) present in a chosen volume and has the units m^3/m^3 for volumetric water content or kg/kg for gravimetric water content. The mathematical definition is:

$$\theta = \frac{\Phi_{water}}{\Phi_{total}}, \Phi \text{ is } V \text{ or } M. \tag{3.2}$$

Saturation is a direct consequence of water content and is defined as the volumetric ratio of wetting liquid present over total void volume:

$$Sat = \frac{V_{wet}}{V_{void}} = \frac{V_{wet}}{\epsilon V_{total}}. \tag{3.3}$$

In addition to saturation there exists effective saturation (also known as normalized water content) which is defined as

$$S_e = \frac{\theta - \theta_r}{\theta_s - \theta_r}, \tag{3.4}$$

where θ_s is saturated volumetric water content and θ_r is residual volumetric water content.

3.1.4 Capillary pressure

Capillary pressure is given as the difference in pressure between two phases across the phasic interface and is represented mathematically as:

$$p_c = (p_w - p_{nw}), \tag{3.5}$$

where p_w and p_{nw} are the wetting and non-wetting phase pressures near the interface. We make a note here that traditionally this pressure is defined as the non-wetting phase minus the wetting phase however we use the inverse definition due to a later application and discussion. It is worth noting that a positive capillary pressure for us denotes liquid pressure greater than air pressure, leading to a convex meniscus and consequently requires surplus energy to drive the fluid infiltration, as opposed to capillary suction. This can be visualized in Figure 3.1.

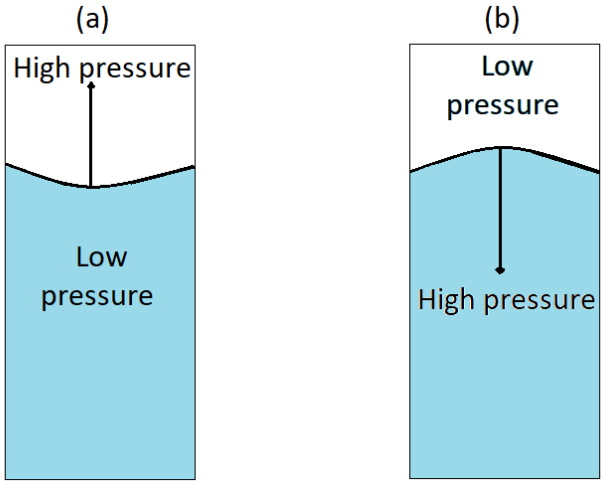

Figure 3.1: Visualization of capillary pressure at the interface, the arrows represent the direction of force applied by the surface tension, air-water.

3.2 Current state of research

Before proceeding with a clear goal statement for the scope of this section of the thesis we provide a brief background on the state of the art research with regard to modeling porous media flow under both saturated and unsaturated conditions. The most common mathematical models used in the modeling of porous media flow are Darcy's law, Richard's equation, and an application of the Kirchhoff potential. These models aim to capture the behavior of the flow at a macroscopic level. By this we mean that the flow is calculated in a continuum with no void spaces. This representation is very convenient for large-scale problems such as calculating flows in aquifers and natural reservoirs where high spatial precision may not be vitally important. When the scale of the domains of interest are reduced it becomes more important to accurately track wetting fronts, velocity of the flow, and local pressure gradients. This requirement for higher accuracy has motivated many researchers to examine porous media flow in detail with the outcome that there still remain several unsolved challenges within the field, most pertaining to the case of variable saturation, where multiple liquid phases interact with the solid porous material as well as each other.

3.2.1 Macroscopic models

Darcy's formulation for porous media flow is one of the most common methods developed originally for flow in saturated media and has been modified for specific purposes. For example, Belleghem et. al. 2014 (Van Belleghem et al. 2014) developed a new coupled HAM (heat-air-moisture) model that includes envelope convection and diffusion within the porous medium. The model uses Darcy's law for moisture transport and Fourier's law for heat transfer. Li et. al. 2009 (Q. Li et al. 2009) employ a HAM-BE model that takes advantage of COMSOL/MATLAB inter-functionality and the model is tested against the HAMSTAD benchmarks with good results. The

HAMSTAD benchmarks were created by a collaboration of researchers to standardize numerical methods for calculation of HAM models (Hagentoft et al. 2004). Others have modified these HAM models to include non-isothermal liquid transport such as Tariku et al. 2010 (Tariku et al. 2010) and Belleudy et al. 2016 (Belleudy et al. 2016) however these were never validated.These models were coupled with finite-element-method (FEM) calculations as in Hibi et al. 2015 (Hibi et al. 2015) and Defraeye et al. 2012a (Defraeye et al. 2011).

Richard's equation represents the expansion of the Darcy formulation to include unsaturated flow. One issue with the Richard's equation is that it is not analytically closed, requiring external conditions and models for closure. Charpentier developed a model employing Richard's equation alongside the van Genuchten closure model and validated it against experimental results (Charpentier 2009). Li and Babcock Jr. solved Richard's equation in the software HYDRUS-2 wherein the boundary conditions included precipitation fluxes, irrigation, and evapotranspiration to determine the effect of porosity on rainwater retention and vegetation growth (Y. Li and Babcock Jr. 2015). Weill et al. proposed a coupling of Darcy's law and Richard's equation to calculate flows across three physical domains with differing saturation levels (Weill et al. 2009). Janssen assessed the simulation efficiency and accuracy of several moisture transfer potentials: two relating to capillary pressure and one with relative humidity (Janssen 2014). Results were mixed, however the recommendation was to use capillary pressure of relative humidity in such moisture transport models.

Regardless which model is used at the macroscopic scale information regarding the interdependence of permeability or hydraulic conductivity and water content must be ascertained in order to close the models. We specifically state models because Darcy's law can be extended to multiphase in a different manner as that of Richard's equation, detailed later in the text. In addition, subzero temperatures are problematic and boundary conditions between porous domains and those with unobstructed flow require additional consideration. It is precisely these relationships that are of intense interest for researchers and the issues encountered with macroscopic modeling are elucidated below. Ferrari et al. 2015 (Ferrari, Jimenez-Martinez, et al. 2015) discussed the issues in numerical modeling of unsteady porous micromodels and their augmentation of the datasets derived form experimental work. Table 3.1 gives an overview of different numerical approaches along with works that used them which are not discussed directly in the text.

3.2.2 Modeling difficulties

Free-flow domain and porous media boundary layer

When we model flow through porous media we assume that the dominant characteristic of the flow is viscosity due to the low velocities involved. This assumption simplifies the equations that are solved quite handily, however this becomes a problem when attempting to combine porous media flow with what is termed "free-flow". In free-flow areas the assumption of viscous-dominance may no longer hold true, and we must capture inertial flow, which can be driven by gravity or some pressure difference. When modeling free-flow using CFD we track the pressure and velocity of the flow,

Table 3.1: Macroscopic scale modeling techniques used in porous media flow.

Author	Model	FEM	FVM	Anal.	Exp.	Other
(Aggelopoulos and Tsakiroglou 2008)	Darcy				X	
(Goel and O'Carroll 2011)					X	
(Goel, Abidoye, et al. 2016)					X	
(Hanspal and Das 2012)	Darcy		X			
(Jahanbakhshi et al. 2013)				X		
(Johnson et al. 2019)		X				
(Juanes 2008)			X			
(Koniorczyk and Gawin 2006)	HAM	X				
(Manthey, Hassanizadeh, and Helmig 2005)	Darcy		X			
(Manthey, Hassanizadeh, Helmig, and Hilfer 2008)	Darcy		X			
(Mikelić and Paoli 1997)				X		
(Mikelić 2003)				X		
(Nieber et al. 2005)	Richard's		X			
(Rätz and Schweizer 2014)	Richard's			X		
(Rudiyanto et al. 2020)				X		
(Virnovsky et al. 2004)	Darcy		X			
(H. Zhang and Zegeling 2017)						X
(Zhuang et al. 2019)	Darcy	X				

however in porous media flow only pressure is tracked. This creates a problem on the boundary between these two regimes as we must apply some condition on this boundary that allows for each to be solved without overdetermination of any one system. Several boundary conditions have been proposed such as the Beavers and Joseph condition (Beavers and Joseph 1967) however all such conditions are not rigorously proven for multiphase systems (Jäger and Mikelić 2000), leaving their accuracy for smaller domains in particular in question.

Subzero temperatures and ice formation

Subzero temperatures over sufficiently long periods can cause residual liquid in the soil structure to freeze, fundamentally altering the attributes of the soil composition. Most existing models do not treat this phenomenon at all due to the liquid-solid phase change, though one such example is work by Häupl and Xu (Haeupl and Xu 2001). In fluid dynamics liquids are defined using density, and more importantly in this case, with viscosity. When a liquid freezes its viscosity goes to infinity (resembling a solid) and this causes severe problems numerically, causing simulations to crash instantly. This can be overcome to an extent by limiting the viscosity to some very high value, however this does not take into account the effect the transition has on the remaining liquid surrounding the "frozen" areas.

Capillary pressure-saturation–permeability dependence and hysteresis

The most challenging aspect of modeling unsaturated porous media flow lies in the relationship between capillary pressure, saturation, and permeability (or hydraulic conductivity). These relationships have been the subject of intense research due to the fact that in order to close the macroscopic models presented prior it is generally necessary to fit an equation to experimental data and generate what is known as a soil water retention curve (SWRC) or water retention curve (WRC). These curves serve to relate the aforementioned quantities however they are limited in a variety of ways. One such way is that each material or composition behaves very differently with regard to the effect of changing saturation and indeed the wetting and drying processes are different, even for the same material. Thus to accurately capture the effect of variable saturation one must perform extensive and time consuming experiments to determine the correct fitting coefficients to models describing this process. This means that not only are spatial inhomogeneities contributing to difficulties in determining the curve fittings but that there exists a difference in these curves during the wetting and drying processes. This difference in behavior in wetting and drying is known as hysteresis and is a large contributing factor to the difficulties encountered in modeling unsaturated porous media flow. In addition to this issue we also point out that these curves are generated at a particular temperature and thus one would expect that large temperature variations may effect the behavior and require the generation of unique curves for various desired temperatures. It is immediately clear that such an undertaking experimentally is highly unfeasible if one desires high accuracy over a range of porous media and climatic conditions.

Several models for determining SWRCs exist such as the van Genuchten model (Genuchten 1980), Purcell method (Purcell et al. 1949), and the Brooks-Corey model (Brooks and Corey 1964) and a direct comparison of these models can be found in Li and Horne (K. Li and Horne 2006). These models are calibrated using fitting parameters to fit experimental data. Several researchers have improved upon the methods for determining hydraulic conductivity and water content, usually through the use of a tensiometer or flow experiments. Wayllace and Lu (Wayllace and Lu 2012) presented a novel transient water release and imbibition (TWRI) method to rapidly capture the SWRC and hydraulic conductivity function under both drying and wetting conditions. Gallage et al. used dual liquid tensiometers to validate their accuracy for sandy soils (Gallage et al. 2013). Wadsö et al. proposed an improvement on previous methods for measuring relative humidity in soil samples without disturbing the sample during measurement, accomplished by keeping the sample sealed to prevent alteration in the local relative humidity (Wadsö et al. 2004). Soltani et al. carried out a statistical analysis of model parameters in order to generate SWRC curves for different soil classes rather than individual experimental datasets, removing direct subjectivity of the resulting curves (Soltani et al. 2019). Nijp et al. outline alterations to the constant-head permeameter capable of measuring hydraulic conductivity at high porosity values (Nijp et al. 2017). Siltecho et al. 2015 provide an overview of many of the experimental methods and outline their respective strengths and weaknesses (Siltecho et al. 2015).

3.2.3 Meso-scale and pore-scale modeling

Rather than attempt to close the problem at the macroscopic scale wherein the continuum assumption is held; another approach has been to model fluid infiltration and drainage at the pore-scale and solve the fluid flow directly. Some researchers have opted to employ traditional CFD techniques to solve the problem however the complex geometries present at this scale make this approach both computationally expensive and time-consuming. An alternative approach is to drop the continuum assumption and solve individual fluid particle motion using the Boltzmann equation for particle motion. This approach is known as the lattice Boltzmann method (LBM) and is described in detail in section 3.6.

Many researchers have employed LBM to examine at the pore scale the effects of a variety of parameters on multiphase porous media flow. Work by Li et al. described the influence of geometrical properties on steady state fluid distribution and capillary pressure in a variety of 2d porous matrices (Z. Li et al. 2018). Suh et al. examined the effect of irregularly shaped pore throats on the capillary pressure within the matrix and concluded the use of the Mayer and Stowe-Princen theory in lieu of the traditional Young-Laplace approach provides good agreement with experimental data (Suh et al. 2017). Porter et al. undertook an examination of the influence of interfacial area in addition to the capillary pressure-saturation interaction and determined that its inclusion as a variable in such models removes the need for scanning curves to accurately represent the hysteretic nature of the imbibition-drainage process (Porter et al. 2009). Liu et al. (Z. Liu et al. 2017a) employed an Euler characteristic to quantify pore structure influence on capillary flow.

The studies discussed above are evaluated at equilibrium and thus do not give any insight into the dynamic quantities and their impact on multiphase flow through porous media. By equilibrium we mean that the liquid velocities are zero and the interface between the phases is stable. In 1987 Weitz et al. studied the dependence of velocity and capillary pressure and their impact on viscous fingering and determined the dynamic component of capillary pressure to have a stabilizing effect on the formation of viscous fingers (Weitz et al. 1987). Cueto-Felueroso and Juanes employed a continuum model based upon thin film flow models to capture the effect of surface tension without introducing new independent parameters and found good agreement with experimental results. This work also confirmed the phenomenon wherein finger velocity and width increase with higher liquid infiltration velocity (Cueto-Felgueroso and Juanes 2008). In 2012 Hilpert developed a model based upon the generalized Green-Ampt approach and showed its ability to correctly estimate the capillary pressure overshoot depending upon upstream and downstream liquid content as well as solid grain size. This formulation of capillary pressure is velocity-dependent as well as dependent upon liquid content (Hilpert 2012). In 2011 Løvoll et al. performed experiments on liquid primary drainage and were able to generate collapsed curves relating the capillary number of a system and its corresponding pressure-saturation curve. They also postulated that the dynamic effects in the capillary pressure may be a combination of the viscous effects from the wetting phase in conjunction with the capillary pressure along the direction of the gaseous phase front (Løvoll et al. 2011).

Vogel et al. (Vogel et al. 2005) performed a comparison between a pore-network model, a lattice Boltzmann approach, and a traditional CFD approach on determining the soil-water retention curve and found the pore network model to be the best option for cost. The limitation of the lattice Boltzmann method was the regularized lattice which had difficulty capturing thin films within the pores. Work by Joekar-Niasar et al. have focused on employing pore network modeling with the addition of a dynamic capillary term to more accurately solve two-phase flow in a porous medium (Joekar-Niasar, Hassanizadeh, and Dahle 2010), (Joekar-Niasar and Hassanizadeh 2011), (Joekar-Niasar and Hassanizadeh 2012). They investigated the non-equilibrium capillary effects under drainage and imbibition as a function of saturation, viscosity ratio, and effective viscosity. Primulkov et al. (Primkulov et al. 2019) introduced a "moving capacitor" pore network model which models the fluid-fluid interfaces as moving capacitors within the more traditional pore network model fixed resistor approach. This model allows the capturing of displacement patterns and the injection pressure signal under a larger variety of capillary numbers and wettabilities. Qin et al. have shown that multiform idealized pore elements used in pore network modeling, in combination with the Young-Laplace equation, result in an over-prediction of the capillary force at the wetting front. This result in an over-prediction of the imbibition rate (Qin and Brummelen 2019).

Li et al. employed a FEM approach with a zero-thickness interface element to solve unsaturated flow in fully 3D porous media (X. Li et al. 2017). The results showed accurate capturing of the wetting front as well as flow velocity and pressure distribution within the network. Jeff Gostick and fellow researchers have developed an open source pore network modeling software (OpenPNM) (Gostick et al. 2016) and tested its efficacy against direct numerical solvers such as FEM and LBM methods. The results showed that for the computational expenditure the more simplistic pore network models provide good accuracy, dependent upon discretization schemes used (Sadeghi et al. 2020). The models are based upon the advection-diffusion equation but incorporate the use of power-law and hybrid finite difference schemes as well as the analytical solution to the 1D advection-diffusion equation.

Zhao et al. developed several improvements to the conventional pore network model by increasing the accuracy of the pore throat representation from simple geometry to full topolgy and solved the transport using a lattice Boltzmann coupling (Zhao et al. 2020). The results showed the most efficient was IPNM2 which uses sub-throat bonds with varying cross-sections to describe the throat topology whereas the full topology was more accurate but suffered from increased computational time. Carmeliet et al. presented a multi-scale pore network model capable of capturing large ranges in pore size by modeling the network at multiple layers of magnification in a two-dimensional grid (Carmeliet, Descamps, et al. 1999) and (Carmeliet and Roels 2001).The conservation of water vapor permeability is used to link the different scales and macroscopic permeability is extracted from an analysis of he calculated permeability at each magnification. This approach was used to determine the macroscopic quantities of a French limestone exhibiting heterogeneous properties and the results were compared to an in-depth experimental analysis of imbibition with good agreement found between the simulations and the experimental results (Roels

et al. 2003b) and (Roels et al. 2003a). Additional works are sorted by numerical approach in Table 3.2 for the reader's reference.

Table 3.2: Mesoscopic and pore-scale modeling techniques used in porous media flow.

Author	Model	FEM	FVM	Anal.	Exp.	Other
(Abidoye and Das 2015)	ANN					X
(Camps-Roach et al. 2010)	PNM					X
(Dahle et al. 2005)						X
(Ferrari and Lunati 2013)	DNS		X			
(Fučík, Mikyška, et al. 2010)			X			
(Fučík and Mikyška 2011)			X			
(Gladkikh and Bryant 2006)						X
(Gray et al. 2015)	LBM		X			
(Hsu et al. 2017)	G-A			X		
(Joekar-Niasar and Hassanizadeh 2011)	PNM					X
(Joekar-Niasar and Hassanizadeh 2012)	PNM					X
(J. Li et al. 2017)	PNM					X
(X. Li et al. 2017)		X				
(Y. Li, C. Liu, et al. 2020)	PNM				X	
(Lunati and Or 2009)	N-S		X			
(O'Carroll, Phelan, et al. 2005)			X			
(O'Carroll, Mumford, et al. 2010)			X			
(Pellichero et al. 2012)	G-A			X		
(Primkulov et al. 2019)	PNM					X
(Qin and Brummelen 2019)	PNM					X
(Raeini et al. 2014)	N-S		X			
(Solazzi et al. 2020)	N-S		X			
(Toussaint et al. 2012)					X	
(Vogel et al. 2005)	PNM, LBM, N-S					X
(J. Yang et al. 2017)	PNM				X	
(Zhou et al. 2013)	LBM					X

There still remain many unanswered questions regarding the influence of the porous microstructure on infiltration dynamics, particularly if the hydrophilicity or hydrophobicity of a material is considered. In addition, the impact of layering and thickness remains open and in transient systems the role of dynamic capillary pressure has not been adequately quantified with regard to infiltration dynamics and might impart some insight into the previously outlined issues at the macroscopic scale.

3.3 Goal of doctoral research (pt. 2)

The goal of this aspect of the work is to provide increased insight into the impact of the growth substrate on storm water infiltration dynamics. This is done by applying the lattice Boltzmann method to chosen porous domains representing the growth substrate of a green roof. We identify and quantify the underlying physical phenomena responsible for transport of storm water through these porous domains and apply the observations to provide guidelines for substrate design. This is accomplished by extracting properties of the flow and the solid microstructure and linking observations with physical and mathematical formalizations.

3.4 Porous media flow modeling and Darcy's law

The Darcy model was developed in 1856 by Henry Darcy and was experimentally determined however the formal derivation from the Navier-Stokes equations was given by Whitaker in 1986 (Whitaker 1986). The simplest steady-state representation of Darcy's law is a consequence of the assumption of high quantities of water already present in the soil, thus the equation only considers one phase, that of the water.

$$\nabla \cdot \mathbf{v}_w = 0, \tag{3.6}$$

$$\mathbf{v}_w = -\frac{\mathbf{K}}{\mu_w} \cdot (\nabla p_w - \rho_w \mathbf{g}), \tag{3.7}$$

where $\mathbf{v}_w$ is the wetting phase Darcy velocity, $\mathbf{K}$ is the permeability tensor, μ_w, p_w, ρ_w are the wetting phase dynamic viscosity, pressure, and density, respectively, and $\mathbf{g}$ is gravity. When we say Darcy velocity we mean a velocity related to the actual flow velocity by the porosity:

$$\mathbf{u}_w = \frac{\mathbf{v}_w}{\epsilon}, \tag{3.8}$$

where $\mathbf{u}_w$ is the actual flow velocity. This formulation can be extended to include multiple phases, with the addition of a few new terms.

3.4.1 Extension to multiphase to variable saturation

The extension of Darcy's law to multiphase is straightforward; define a set of equations for each fluid phase and a scalar variable equation representing the fraction of each

phase present in a single averaging (or computational) volume. Darcy's law can be extended to multiphasic systems by including a subscript $\omega(=\eta)$, giving

$$\begin{aligned} \omega &= w, nw, && (3.9)\\ \alpha_w + \alpha_{nw} + \epsilon &= 1, && (3.10)\\ \frac{\partial \alpha_\omega}{\partial t} + \nabla \cdot \mathbf{v}_\omega &= 0, && (3.11)\\ \mathbf{v}_\omega &= -\frac{\mathbf{K}_\omega}{\mu_\omega} \cdot (\nabla \langle p_\omega \rangle^\omega - \rho_\omega \mathbf{g}) + \mathbf{K}_{\omega\eta} \cdot \mathbf{v}_\eta, && (3.12) \end{aligned}$$

where α_ω is the volume fraction of each phase and $\mathbf{K}_{\omega\eta}$ represent viscous drag effects of one phase upon the other. It is worthwhile to mention that $\mathbf{K}_{w,nw} \neq \mathbf{K}_{nw,w}$ and that these terms can be considered negligible when the magnitude difference of the viscosities is non-unity. The discussion surrounding these terms and the details of the derivation for multiphase Darcy's law can be found in Whitaker (Whitaker 1986). Note that the derivations by Whitaker are valid for quasi-steady state flows. Previously we have considered only a single permeability $\mathbf{K}$ as a material property however in multiphase we now have to consider the interactions between the solid matrix and the fluid phases in addition to their effects on each other. As previously introduced this is relative permeability $k_{r\omega}$ and its mathematical relationship to intrinsic permeability is:

$$\mathbf{K}_\omega = k_{r\omega}\mathbf{K}. \tag{3.13}$$

As with the intrinsic permeability, all values here are represented in tensor form due to the fact that the values can be highly directional. While it may be possible to accurately measure anisotropic values for intrinsic permeability, determining such values for relative permeability is far more difficult and thus this tensor is often reduced to a scalar value. Several approximations can be used to calculate relative permeability and a few are introduced here. The approximations aim to capture lubricating effects on the solid matrix, capillary suction and interpenetration of the phases. When we say interpenetration of the phases we must stress that the phases are considered immiscible and the only possible mass transfer must occur via condensation/evaporation. As we have not introduced temperature dependence this will not be considered further. The phase interaction represented by relative permeabilities is by its construction phase volume fraction dependent.

There are several models to relate saturation (or effective saturation) to capillary pressure such as the Brooks-Corey model used in the oil and gas industry, the Purcell method, and the van Genuchten-Mualem model (VGM). The reader may find a more complete description of these models in the original papers by Brooks and Corey (Brooks and Corey 1964), Purcell (Purcell et al. 1949), and van Genuchten (Genuchten 1980) respectively. We present here the VGM model as it serves to elucidate the issue encountered in accurately modeling variable saturation. The VGM model is comprised of:

$$\begin{aligned} S_e &= [1 + (p_c/p_g)^n]^{-m}, && (3.14)\\ m &= 1 - 1/n, && (3.15) \end{aligned}$$

where p_c is the capillary pressure, p_g is a pressure scaling value, and m and n are fitting coefficients related to the pore size distribution. In order to complete the relationship between relative permeability and effective saturation we must introduce hydraulic conductivity κ, which describes the ability of liquid to flow through the pore spaces of a porous medium. It is related to permeability by

$$\mathbf{K} = \kappa \frac{\mu_w}{\rho_w \mathbf{g}}. \tag{3.16}$$

Now that we can relate permeability and hydraulic conductivity we can define the relationship we require accordingly as

$$\kappa(S_e) = \kappa_s \kappa_r(S_e), \tag{3.17}$$
$$\kappa(S_e) = \kappa_s S_e^q (1 - (1 - S_e^{1/m})^m)^2, \tag{3.18}$$

where κ_s is the saturated hydraulic conductivity and q is a model parameter representing the pore connectivity. If we wish to use the VGM model, we require the coefficient values and material properties. This requires extensive and difficult experimentation to correctly determine their values as the parameters are fit to experimental data and a full curve relating hydraulic conductivity to effective saturation is generated.

3.5 Quantification methods for storm water runoff mitigation

In order understand the full capabilities of green roofs to act as urban storm water mitigation devices we must be able to accurately quantify their performance. This quantification of storm water runoff mitigation can be categorized into two phenomena, detention and retention of water. Retention here refers to the entrapment of water within micro-pores of the growth substrate which serves to lower overall runoff quantity and is removed by evapotranspiration. Evapotranspiration is defined as the process by which water is transferred from the soil to the atmosphere by way of simple evaporation and plant activity. It is worthwhile to note that since the process of evapotranspiration occurs over a much longer time scale than that of mechanical detention, these studies typically take periods from months to years. The role of evapotranspiration has been the subject of many works, such as those of (Cascone et al. 2019), (Mobilia et al. 2017), (Johannessen et al. 2018), (W. Liu et al. 2019) and (Viola et al. 2017).

Detention of storm water refers to the mechanical process by which the infiltration of water is slowed as it travels through the green roof system. The detention serves to reduce peak flow quantities and also provide a delayed and extended runoff period, allowing for traditional storm water infrastructure to more easily avoid being overwhelmed, which can lead to urban flooding problems. Detention is a faster acting process as it only considers the reduction and delay in runoff caused by the presence of the growth substrate and drainage layers. These processes are difficult to separate from an experimental point of view as measurements on detention will

include some contribution from retention, particularly if the soil is largely unsaturated. If one makes the assumption that this contribution is minimal and if the soils are generally not largely unsaturated then the separation is much more straightforward for experimental measurements; unfortunately this is not the case when modeling is introduced to predict these behaviors.

3.6 Introduction to the lattice Boltzmann method (LBM)

3.6.1 The Boltzmann equation

The lattice Boltzmann method is an alternative to the traditional Navier-Stokes approach by solving the discrete Boltzmann equation. It can be applied to the mesoscopic scale as well as the macroscopic scale, depending on the desired resolution and problem scale. While it has advantages over traditional CFD modeling I do not believe it can be used as a substitute due to the extensive background enjoyed by CFD. The original method to use this approach was developed in the 1950s by Ulam and von Neumann and was called the Lattice Gas Automaton. The method has been modified since its earliest form and is experiencing a resurgence in interest due to its capacity for handling multiphase flows in complex geometries, among other benefits. Once again we will present a brief derivation of the discrete Boltzmann equation that is solved in LBM and stress the assumptions required for its application. A more complete derivation can be found in (Maggiolo 2017b).

Before we can present the Boltzmann equation we must discuss the idea of a phase space and a corresponding density function. A phase space is defined as a space in which every state of a system corresponds to a single point within the space. In our case it is defined by positional coordinates $\vec{x}$ and momenta $\vec{p} = M\vec{v}$ where M is mass and $\vec{v}$ is velocity. The space is 6-dimensional and each position is parameterized by time t. Thus a differential elementary volume can be written as

$$d^3\vec{x}d^3\vec{p} = dxdydzdp_xdp_ydp_z, \tag{3.19}$$

and the corresponding density function $f(\vec{x}, \vec{p}, t)$ is defined such that the probable number of particles in the volume is given by

$$N = \int d^3\vec{p} \int d^3\vec{x} f(\vec{x}, \vec{p}, t). \tag{3.20}$$

We can now represent the general Boltzmann equation in terms of the density distribution function by

$$\frac{df}{dt} = \left(\frac{\partial f}{\partial t}\right)_{force} + \left(\frac{\partial f}{\partial t}\right)_{diff} + \left(\frac{\partial f}{\partial t}\right)_{coll}, \tag{3.21}$$

where the force term represents any external force applied to the particles, the diffusion term represents particle diffusion, and the collision term represents inter-particle collisions. After some re-representation of the force and diffusion terms we

can rewrite equation 3.21 by balancing these terms against the collision term.

$$\frac{\partial f}{\partial t} + \frac{\vec{p}}{M} \cdot \nabla f + \vec{F} \cdot \frac{\partial f}{\partial \vec{p}} = \left(\frac{\partial f}{\partial t}\right)_{coll}. \tag{3.22}$$

Before we can solve this equation we must find a representation for the collision term. Deriving this term requires knowledge of statistical mechanics beyond the scope of this work however we will give its representation and most common simplified form in the interest of completeness.

$$\left(\frac{\partial f}{\partial t}\right)_{coll} = \int (\hat{f}_{12} - f_{12}) \vec{g} I(\vec{g}, \Omega) d\Omega d\vec{p}_{12}, \tag{3.23}$$

where $\hat{f}_{12}$ is the post-collision distribution of particles 1 and 2, $\vec{g} = \vec{v}_1 - \vec{v}_2$ is the relative velocity between the particles, I is the differential cross-section of the collision and Ω is the characteristic angle of collision. It is important to note that in order to calculate such interactions Boltzmann applied the argument of so-called *Stosszahlansatz*, or "molecular chaos". This argument states that while the probabilities of two particles colliding is reliant on the collisions of other particles with them *ad infinitum*, however we can consider their distribution functions independent of each other, such that

$$f_{12} = f_1 f_2, \tag{3.24}$$

and consequently we can rewrite equation 3.23 as

$$\left(\frac{\partial f}{\partial t}\right)_{coll} = \int\int (\hat{f}_1 \hat{f}_2 - f_1 f_2) \vec{g} I(\vec{g}, \Omega) d\Omega d\vec{p}_1 d\vec{p}_2. \tag{3.25}$$

For covenience when describing the the discrete Boltzmann equation we can rewrite 3.22 in terms of a streaming operator $\mathscr{S}$ and a collision operator $\mathscr{C}$.

$$\mathscr{S} f = \mathscr{C}_{12}. \tag{3.26}$$

In addition we can relate the macroscopic quantities density ρ, momentum $\rho\mathbf{v}$ and energy density ρe to the collision invariants. These collision invariants are the particle number, momentum and energy. These quantities are related by

$$\rho = M \int f d\vec{v}, \tag{3.27}$$

$$\rho\mathbf{v} = M \int f \vec{v} d\vec{v}, \tag{3.28}$$

$$\rho e = M \int f \frac{\vec{v}^2}{2} d\vec{v}. \tag{3.29}$$

The few final notes on the Boltzmann equation deal with equilibrium. The distribution function satisfies the condition of local equilibrium, that is particles entering the element are balanced with those exiting. In addition, fluids tend to local equilibrium and this process is called local equilibrium relaxation. This relaxation takes place from one-body distribution to local equilibrium among particles and

finally to global equilibrium over the domain. It is therefore unsurprising that one can link the particle kinetics to macroscopic scale theory by spanning ever-larger time scales. It is possible to derive the Navier-Stokes equations of motion from the Boltzmann equation by expanding the variables appropriately. This is done by applying the Chapman-Enskog expansion however the details are beyond the scope of this work.

3.6.2 Lattice-Gas Cellular Automata

In order to reach the discrete Boltzmann equation formulation we must start with the theory behind the predecessor of LBM, the Lattice-Gas Cellular Automata (LGCA). In this method a cell is composed of nodes and vectors connecting them to each other. The cell can be a variety of shapes in 2 and 3 dimensions but we shall focus on a square 2-dimensional lattice for our explanation. The vectors connecting the nodes are given as $\vec{c}_r = [c_{ri}, c_{rj}]$ where r is a node number a i, j are Cartesian coordinates x, y. There are a few rules for lattice occupancy, namely:

- All particles have the same mass, $M = 1$.
- A particle can move only in one direction in a single time interval.
- A particle moves from $\vec{x}$ to $\vec{x} + \vec{c}_r$.
- Two particles in the same position cannot move in the same direction.

These rules allow for a cell to hold up to 8 fluid particles simultaneously at a single time instant and we therefore define an occupancy number n_r to define the possible states

$$n_r(\vec{x}, t) = 0, \text{ no particles present,} \tag{3.30}$$
$$n_r(\vec{x}, t) = 1, \text{ a particle is present.} \tag{3.31}$$

The streaming and collision operators given in the compressed Boltzmann equation 3.26 can be written in discrete format to describe a particle's motion in the lattice by

$$\mathscr{S}_r n_r = n_r(\vec{x} + \vec{c}_r, t + 1) - n_r(\vec{x}, t), \tag{3.32}$$
$$\mathscr{C}_r(n_1, ..., n_9) = \hat{n}_r(\vec{x}, t) - n_r(\vec{x}, t), \tag{3.33}$$
$$\mathscr{S}_r n_r = \mathscr{C}_r(n_1, ..., n_9), \tag{3.34}$$

where $\hat{n}_r$ is the post-collision state. In order to recover the Navier-Stokes equations the collisions in this system must satisfy conservation of mass and momentum. In addition, the cells must be shaped such that the rotational invariance of the Navier-Stokes stress and strain tensor elements is properly captured.

3.6.3 The lattice Boltzmann equation

An improvement upon the LGCA was developed by McNamara and Zanetti (McNamara and Zanetti 1988) in 1988 that removes the occupancy number Boolean values and replaced them with a mean and fluctuating value

$$n_r = f_r + r_r, \tag{3.35}$$

where f_r is the spatial and temporal mean value of the occupancy number and r_r is the fluctuation. This modification meant that rather than fixing particles to a specific point, each location is assigned a mean probability of finding a particle at that location. The motivation for this change was to reduce statistical noise which was present in the LGCA. Substituting equation 3.35 into 3.34 we get

$$\mathscr{S} f_r = \mathscr{C}_r(f_1, ..., f_9) + R_r, \tag{3.36}$$

where R_r is the sum of the fluctuations. Due to the concept of molecular chaos mentioned earlier all particles are uncorrelated and thus all have the same probabilities thus $R_r = 0$. Thus the non-linear lattice Boltzmann is written as

$$\mathscr{S} f_r = \mathscr{C}_r(f_1, ..., f_9). \tag{3.37}$$

In order to overcome the nonlinearity of the collision operator the Chapman-Enskog expansion was suggested by both McNamara and Zanetti (McNamara and Zanetti 1988) as well as Higuera and Jimenez (Higuera and Jiménez 1989) to generate the quasi-linear lattice Boltzmann equation

$$\mathscr{S} f_r = \mathscr{A}_{r_1 r_2}(f_{r_1} - f^e_{r_2}), \tag{3.38}$$

where r_1, r_2 are distinct directions and $\mathscr{A}$ is a scattering matrix. A further modification of this equation resulted in the Lattice-Bhatnagar-Gross-Krook (LBGK) model. This model replaced the scattering matrix with a single parameter τ to define the physics of the fluid and is written as

$$\mathscr{S} f_r = -\frac{1}{\tau}(f_{r_1} - f^e_r). \tag{3.39}$$

This model is also known as the single time relaxation model and requires the satisfaction of the conditions:

$$\rho = \sum_r f^e_r = \sum_r f_r, \tag{3.40}$$

$$\rho v_i = \sum_r f^e_r c_{ri} = \sum_r f_r c_{ri}. \tag{3.41}$$

The equilibrium distributions f^e_r must be chosen to correctly reflect the Navier-Stokes equations in terms of conservation and depend on the choice of cell dimension and shape. In addition there is some restriction of the choice of τ as it is related to fluid kinematic viscosity by

$$\nu = c_s^2(\tau - 0.5), \tag{3.42}$$

where c_s is a speed of sound coefficient. From this we can see that values of τ below 0.5 will induce a negative viscosity and if we increase it too much we will increase the fluid viscosity similarly.

3.6.4 The lattice Boltzmann model

The solved equation is given as

$$f_r(\mathbf{x} + \mathbf{c}_r\delta t, t + \delta t) - f_r(\mathbf{x}, t) = -\tau^{-1}(f_r(\mathbf{x}, t) - f_r^{eq}(\mathbf{x}, t)) + F_r \tag{3.43}$$

where $f_r(\mathbf{x}, t)$ is the distribution function at position $\mathbf{x}$ and time t along the r-th direction; $\mathbf{c}_r$ is the so-called discrete velocity vector along the r-th direction over time interval δt; τ is the mean collision time and is related to kinematic viscosity by $\nu = c_s^2(\tau - 0.5\delta t)$. The fluid is forced by a body force F_r which mimics the effect of gravity. Such a force is defined following the approach defined by Guo et al. (Guo et al. 2002),

$$F_r = \left(1 - \frac{1}{2\tau}\right) w_r \left(\frac{\mathbf{c}_r - \mathbf{u}}{c_s^2} + \frac{\mathbf{c}_r \cdot \mathbf{u}}{c_s^4}\mathbf{c}_r\right)(\rho\mathbf{g}) \tag{3.44}$$

with $\mathbf{g}$ representing gravitational acceleration and $\mathbf{u}$ the fluid velocity. The equilibrium distribution function $f_r^{eq}(\mathbf{x}, t)$ takes the form

$$f_r^{eq} = w_r\rho\left(1 - \frac{\mathbf{u}_{eq} \cdot \mathbf{u}_{eq}}{2c_s^2}\right),\ r = 1 \tag{3.45}$$

$$f_r^{eq} = w_r\rho\left(1 + \frac{\mathbf{c}_r \cdot \mathbf{u}_{eq}}{c_s^2} + \frac{(\mathbf{c}_r \cdot \mathbf{u}_{eq})^2}{2c_s^4} - \frac{\mathbf{u}_{eq} \cdot \mathbf{u}_{eq}}{2c_s^2}\right),\ r = 2 - 19 \tag{3.46}$$

where w_r is the appropriate weighting parameter for the D3Q19 lattice (3 dimensions, 19 degrees of freedom); ρ is the density; c_s is the speed of sound; and $\mathbf{u}_{eq}$ is the velocity used for defining the equilibrium distribution functions, which can differ from the fluid hydrodynamic velocity, on the basis of the specific forcing scheme used. In the present work, we apply the Guo forcing formulation for implementing the gravitational force whereas we make use of the Shan-Chen force for simulating surface tension (Shan and H. Chen 1993). The macroscopic flow quantities density and velocity, $(\rho, \mathbf{u})$ are thus related to the hydrodynamic moments as the following:

$$\rho = \sum_r f_r \tag{3.47}$$

$$\rho\mathbf{u} = \sum_r \mathbf{c}_r f_r + 1/2\ \rho\mathbf{g} + 1/2\ F_{sc}\ , \tag{3.48}$$

and the equilibrium velocity is formulated as: (L. Chen et al. 2014)

$$\mathbf{u}_{eq} = \rho\mathbf{u} + (\tau - 1/2)F_{sc} \tag{3.49}$$

where F_{sc} is the Shan-Chen gas-liquid interaction force. In practicality in this work we deal with a steam-liquid system wherein some mass transfer between the phases can occur due to the diffuse interface as a consequence of the method. A detailed discussion of the forcing schemes proposed by Shan-Chen and Guo can be found in Huang et al. (H. Huang et al. 2011). The Shan-Chen model was developed to

overcome the limitations of LBM in dealing with components of differing molecular mass as well as thermodynamic phase transitions (Shan and H. Chen 1993). It is an ideal choice since we are interested in the interaction of two immiscible fluids as well as the interaction of the microstructure with the fluids. Its fundamental feature is the addition of an inter-particle potential which adds attractive or repulsive properties in combination with the elastic collision force already present in previous models. The inter-particle force gives rise in the system to a non-ideal equation of state:

$$p = \rho c_s^2 + \frac{G}{2} c_s^2 \Psi^2, \tag{3.50}$$

where liquid and gas phases coexist at the thermodynamic equilibrium state. The Shan-Chen force is given by:

$$F_{sc} = -G\Psi(\mathbf{x}, t) \sum_r w_r \Psi(\mathbf{x} + \mathbf{c}_r \delta t, t) \mathbf{c}_r \tag{3.51}$$

where G, valued -5.5 in this work, is the interaction strength between the phases and $\Psi(\rho)$ is a density-dependent pseudo potential function. Negative values of G define an attractive force and positive values a repulsive force. The pseudo-potential function calculates effective mass locally:

$$\Psi(\rho) = 1 - e^{-\rho}. \tag{3.52}$$

The effective mass approaches ρ itself when its value is low and obtains a saturation value when it is increased. It is capable of capturing the two important characteristics of a non-ideal flow, namely the equation of state in Eq.(3.50) and surface tension.

The fluid-solid interaction is determined by a moving gas-liquid contact line. This contact line is characterised by a contact angle that is chosen under equilibrium conditions, without external forces, as determined by Young's equation. The equilibrium contact angle is implemented through spatial averaging of the density-dependent potential function. The force at the solid wall (Ψ_{wall}) is calculated using the method proposed by De Maio et al. (De Maio et al. 2011) and is of the form:

$$\Psi_{wall} = N^{-1} \sum_N \Psi + \Delta_w \tag{3.53}$$

where Ψ is the density-dependent function and N the nearest fluid computational nodes. This formulation enforces a fixed density gradient at the wall and by tuning the parameter representing surplus density, Δ_w, different contact angles can be represented at the desired lattice resolution. More information regarding the relationship between Δ_w and the contact angle can be found in Benzi et al. (Benzi et al. 2006).

3.7 Implementation of LBM

The open source code developed by Dario Maggiolo was used (Maggiolo 2017a) for all LBM solutions presented in this work and is capable of handling multiphase flow with the density magnitude difference limitation of 10^4, which holds for air and water.

3.7.1 Binary lattice generation

In order to run any simulations a binary 3D lattice representing the desired soil geometry is required. There are a myriad of approaches that may be taken to accomplish this task, from structured or randomized volume packing algorithms to image analysis of X-ray tomography scans. The lattices used in this work are generated using the modeling software Blender, which can handle a large number of objects and apply simple collision physics to allow for a randomized packing in a chosen volume. These spheres can be considered randomly packed and this method of packing has been validated for use as such in (Boccardo et al. 2015). Once the simulation is run in Blender and the particles are randomly packed the sphere center locations are exported to MATLAB and the domain is reconstructed as a 3D binary lattice. The process is shown in Figure 3.2. The computational volume

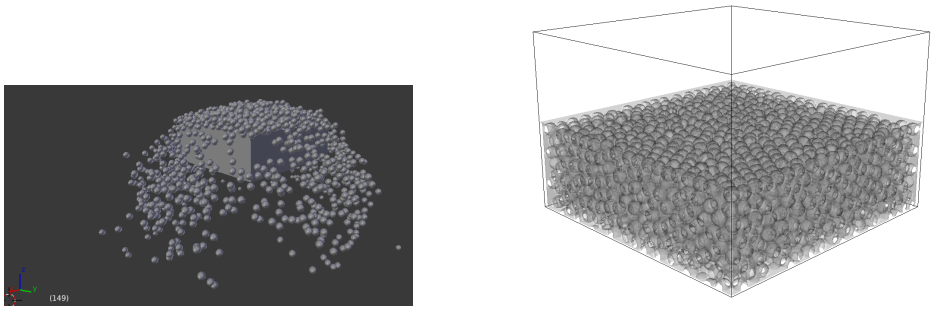

(a) (b)

Figure 3.2: (a) Lattice generation in Blender and (b) reconstruction in MATLAB.

dimensions adhere to restrictions regarding wall effects on the calculated flow field (Galindo-Torres et al. 2016) while capturing a representative soil volume with regard to pore structure and particle size. The spherical particle diameter is calculated from the desired pore-size resolution. The typical pore sizes of lightweight expanded clay aggregates (LECA) are chosen for this work and the relevant data is extracted from the work of Bajare et al. (Bajare et al. 2012). The equivalent grain size is determined from our resolved pore size by applying the Revil, Glover, Pezard and Zamora (RGPZ) model (Glover, Zadjali, et al. 2006), (Glover and Walker 2009) which states

$$d_{eff} = 2\Theta r_{eff}, \tag{3.54}$$

$$\Theta = \sqrt{\frac{e_p w_p^2}{8\epsilon^{2w_p}}}, \tag{3.55}$$

where e_p is a parameter valued 8/3, w_p is the cementation exponent valued 1.5 for spherical particles and ϵ is the porosity.

3.7.2 Simulation inputs and conditions

The height of the packed bed H is determined by the representative volume requirement for the porous medium with particle sizes as previously defined. The particle

diameter is chosen as a characteristic length as it determines the pore microstructure within the porous region. A new parameter ϕ representing the packing effect of the particles on the microstructure is given by

$$\phi = \frac{H}{d}. \tag{3.56}$$

This quantity will be used to define the three different cases of packing arrangements and is one of the two primary parameters in this study. The values of ϕ are listed in Table 3.3. The packed bed length perpendicular to the flow direction, L, is chosen such that it adheres to restrictions regarding wall effects on the calculated flow field (Galindo-Torres et al. 2016). The boundaries perpendicular to the primary flow direction must be at least 15-20 times the particle diameter to ensure wall effects are negated. The information for the three domains is given in Table 3.3 and an example is plotted in Figure 3.3. Here ϵ is the porosity calculated over the domain for each case.

Table 3.3: Packed bed domain physical properties.

ϕ	6.7	10.1	5.1
L×L×H [mm]	15×15×5	15×15×5	15×15×5
d [mm]	0.740	0.494	0.986
ϵ	0.389	0.377	0.40

Boundary conditions

The boundary conditions used in all simulations in this work consist of the following: the upper and lower boundaries are periodic, the transverse boundaries (as defined by length L in Figure 3.3) are symmetric. The driving force for the flow is applied in the vertical direction (as defined parallel to H in Figure 3.3). We note specifically that walls are imposed on the transverse boundaries with the depth of the porous medium given by H. the rest of the domain height $L_T - H$ does not have any walls on the transverse boundaries.

Input values

Table 3.4 displays the input parameters used in the simulations. The physical and lattice unit value are interchangeable via ratios as given in the table caption.

3.7.3 Lattice resolution determination

An appropriate lattice resolution must be determined before any results can be obtained. The choice of resolution has large ramifications on the domain size and consequently computational time and resources required for the calculation. Several lattice resolutions were chosen as detailed in Table 3.5 and it stressed here that as resolution is increased the total node count can increase extremely quickly, thus a

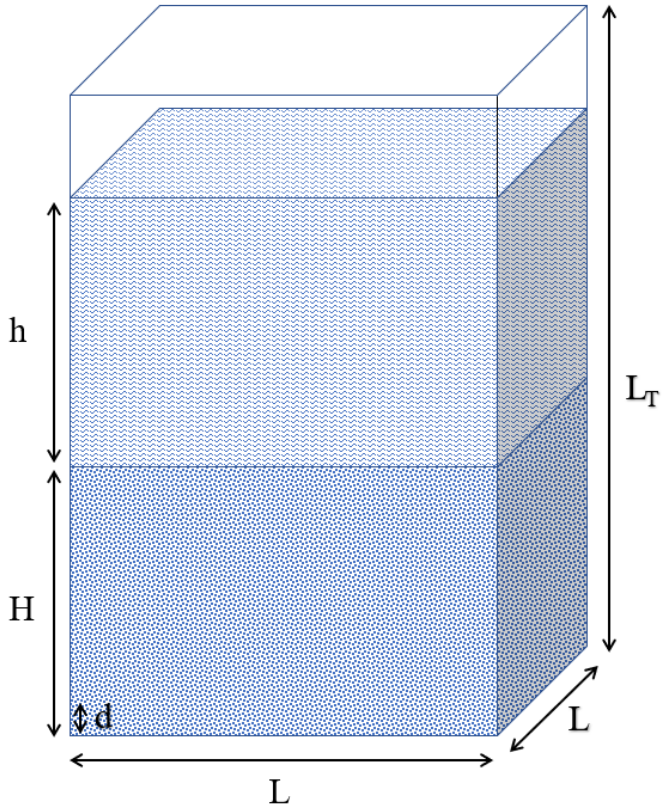

Figure 3.3: Domain dimensions and parameters.

Table 3.4: Physical and non-dimensional input parameters. The physical time is computed via the equivalence between physical and lattice units, i.e. $t = t_{LB}\ (L^2/L_{LB}^2)\ (\nu_{LB}/\nu_l)$. w - wetting phase, nw - non-etting phase.

Parameter	Variable	Value	Physical value	Physical unit
Porous medium height	H	70	5.0	[mm]
Standing water height	h	70, 105	5.0, 7.5	[mm]
Particle diameter	d	10.4, 6.9, 13.8	0.74, 0.494, 0.986	[mm]
Horizontal domain length	L	210	15	[mm]
Dynamic viscosity, w	μ_w	2.4/6	1.00e-3	[Ns/m^2]
Dynamic viscosity, nw	μ_{nw}	0.12/6	1.68e-7	[Ns/m^2]
Kinematic viscosity, w	ν_w	1/6	1.00e-6	[m^2/s]
Kinematic viscosity, nw	ν_{nw}	1/6	1.27e-5	[m^2/s]
Density, w	ρ_w	2.4	998	[kg/m^3]
Density, nw	ρ_{nw}	0.12	1.20	[kg/m^3]
Surface tension	γ	0.093	0.073	[N/m]
Gravity	g	3.3 $\times 10^{-5}$	9.8	[m/s^2]
Time	t	1	8.5 $\times 10^{-4}$	[s]
Contact angle	ρ_{wall}	0.02	82	$^\circ$

balance must be found between computational accuracy and simulation complexity. The resolution chosen for all subsequent simulations is Grid 3, which was determined to meet the resolution and computational time requirements. Single phase simulations

are used to calibrate the correct resolution before any liquid phase is added. The

Table 3.5: Grid resolution test case input and results.

Case	g [lattice units]	Re [-]	Permeability [-]	% Difference
Grid 1	6.53E-5	0.00514	0.00539	-
Grid 2	4.53E-5	0.00575	0.00500	7
Grid 3	3.30E-5	0.00634	0.00474	5
Grid 4	2.55E-5	0.00703	0.00466	2

determination of grid resolution accuracy is accomplished by evaluating the relative error of the dimensionless permeability

$$K^* = K/d^2 = \frac{\overline{U}_z \mu_{nw}}{(\rho_{nw} g) d^2}, \tag{3.57}$$

where K is the permeability, $\overline{U}_z$ is the mean vertical velocity, μ_{nw} is the non-wetting phase dynamic viscosity, ρ_{nw} is the density, and g is gravitational acceleration. The permeability is evaluated only on the inner 2/3 of the geometry in the lateral direction to eliminate the contribution of the side wall effect as noted by Galindo-Torres et al. (Galindo-Torres et al. 2016). The dimensionless permeability in the grid resolution test is computed at a fixed characteristic gas capillary number $Ca_g = \rho_{nw} g d^2/\gamma$, where γ is the surface tension used in the multiphase simulations. The relative difference of dimensionless permeability is calculated over successive grid refinements as:

$$\% \text{ Difference} = \frac{\text{Permeability}_{\text{Grid i+1}} - \text{Permeability}_{\text{Grid i}}}{\text{Permeability}_{\text{Grid i}}}. \tag{3.58}$$

3.7.4 Multiphase simulations

Standing water is initialized within the domain directly above the porous medium. The standing water height h is used as a characteristic length due to its contribution as the body force by way of hydrostatic pressure. Using the particle diameter and standing water height as well as the choice of lattice resolution we can convert all relevant quantities. The results are categorized by two primary non-dimensional parameters; ϕ which is defined previously, and the Bond number

$$\text{Bo} = \frac{(\Delta\rho g) h^2}{\gamma}, \tag{3.59}$$

where g is the variable representing the gravitational component of the body force, $\Delta\rho = \rho_w - \rho_{nw}$ is the phase density difference, and γ is the interfacial surface tension. The Bond number represents the ratio of gravitational and surface tension forces. Work by Slobozhanin et al. showed that for Bond numbers from 0 to 5 there is little difference in the capillary pressure in tightly packed spheres (Slobozhanin et al. 2006). Moreover if the Bond number is below 0.1 the effect of gravity can be neglected entirely.

A statistical analysis of meteorological data taken from Gothenburg, Sweden and provided by Swedish Meteorological and Hydrological Institute (SMHI) is used to determine the standing water height and consequently the Bond numbers used in this study. The statistical analysis of hourly weather data taken over the period 1995.08.04 - 2018.05.01 is used to determine the average rainfall intensity with the result being 2.5 mm/hr when rainless periods are discarded. This value is taken as the equivalent standing water height when the Bond number is 1. Since we are interested in rainfall events causing flooding this number is increased two and threefold for our simulations, analogous to a scenario where extreme rainfall occurs over a short period of time and surface water is present. This corresponds to Bond numbers of 3.96 for a standing water height of $h = 5.0$ mm and 8.92 when $h = 7.5$ mm.

An additional parameter is required for implementing the multiphase simulations; the contact angle. Measurements by Ramírez-Flores et al. (Ramírez-Flores et al. 2010), Schrader and Yariv (Schrader and Yariv 1990), and Fér et al. (Fér et al. 2016) demonstrate the variability of the contact angles with regard to soil aggregates and clay minerals. We motivate our choice of 82° by noting that this value lies within the range of values reported in experimental work. As reported in Fér et al. clay-coated materials exhibit a contact angle around 80° and the value decreases over time. While a singular equilibrium value is set, a dynamic contact angle arises from the simulation due to the presence of external forcing from gravity. A more complicated modeling of the contact angle is neglected on the grounds that we do not expect significant variations in the contact angle due to the low flow velocity of the system (Raiskinmäki et al. 2002).

Once complete, the exported quantities are the velocity vector, density, and the lattice information. With this information it is possible to calculate several quantities of interest, most notably permeability, porosity, average velocity, pore size distribution and saturation. It is worthwhile to note that to ensure no effects from the walls are included we only perform analysis on the interior two-thirds of the domain perpendicular to the flow. The analysis of a variety of multiphase cases is presented in the next section.

3.8 Results and discussion on the role of porous microstructure on infiltration

3.8.1 Selection of the contact angle

The first investigation used variable values of the contact angle given by $\rho_{wall} = 0.03, 0.04, 0.06$ which correspond to an angle of $\theta_c = 82, 78, 72°$, respectively. These results comprised an initial impetus for further examination of the near-neutral contact angle case $\theta_c = 82°$. Figures 3.4 and 3.5 display the saturation as a function of time for four of the cases run. Saturation Sat is calculated by summing the liquid nodes in the porous medium and dividing by the total void node quantity. We stress here that all other parameters are kept identical and the only variation is the contact

angle. We can clearly see the impact of a modification of the contact angle on the

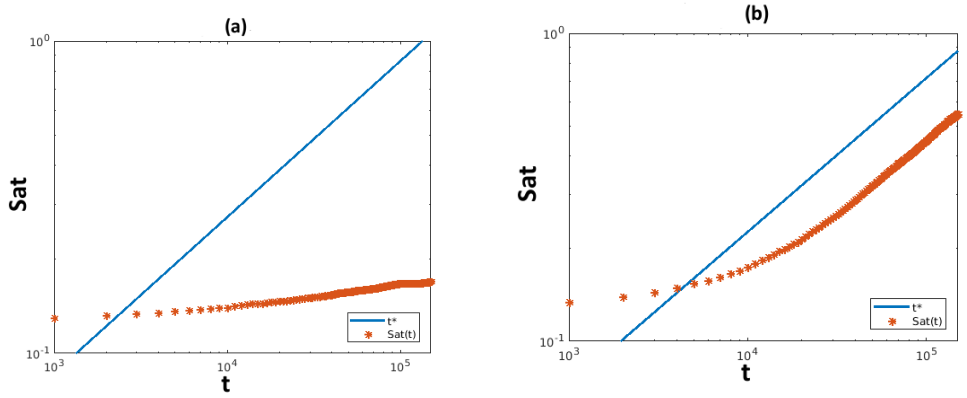

(a) $\theta_c = 82, h = 35$. (b) $\theta_c = 78, h = 35$.

Figure 3.4: Saturation vs time plots for exploratory cases, $h = 35$.

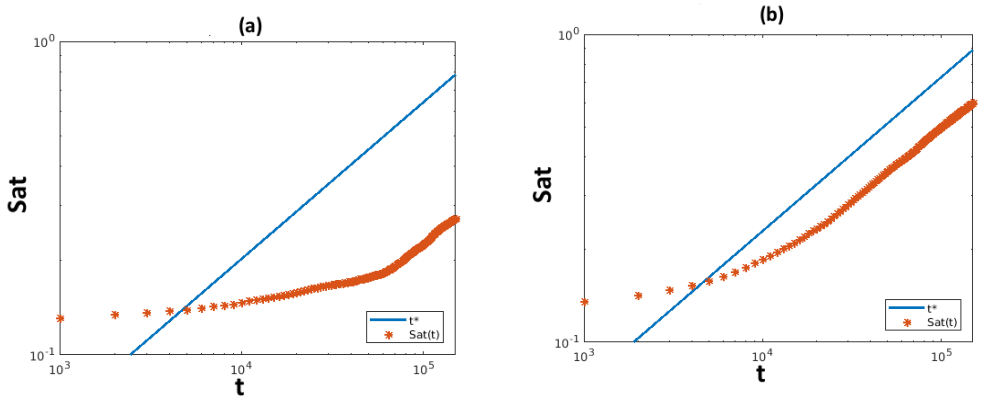

(a) $\theta_c = 82, h = 50$. (b) $\theta_c = 78, h = 50$.

Figure 3.5: Saturation vs time plots for exploratory cases, $h = 50$.

initial stage and subsequent infiltration rate, particularly for the cases with lower standing water height. Indeed in the case of a nearly neutral contact angle the flow almost stagnates however the gravitational forces appear sufficient to force infiltration in the case of higher applied hydrostatic pressure. A more thorough investigation was required to determine the underlying physical processes at work and their criteria for manifestation. One final check to remove the possibility of any lattice resolution or temporal influence on the results was undertaken and simulations were run at higher resolution for three times as long, from 150K to 450K iterations. Figure 3.6 displays clearly that there is minimal influence of the grid resolution on the flow thus we can safely conclude that the phenomenon is physical and not a numerical aberration. Figure 3.7 shows the extensions of the original cases from Figure 3.4a and 3.5a in time. We can conclude that there appears to be a period of liquid buildup to a point that further infiltration can occur, wherein the gravitational forces overcome the surface tension forces. We also note here that when the simulations were extended

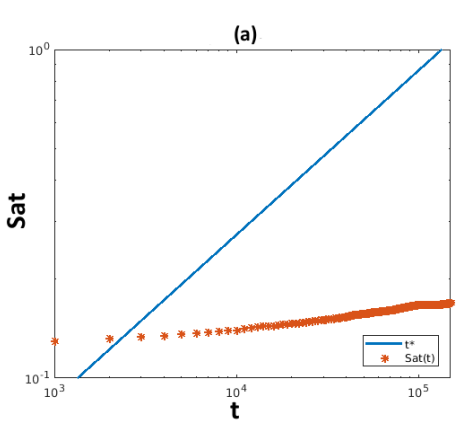

(a) $\theta_c = 82, h = 35$.

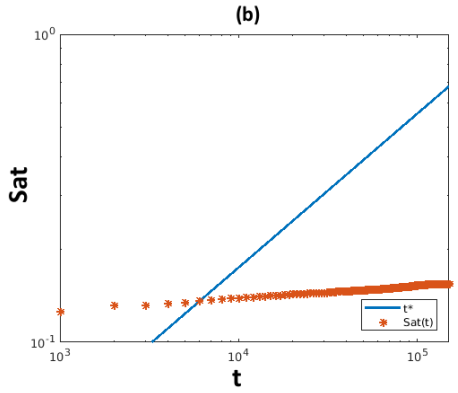

(b) $\theta_c = 82, h = 40$, increased lattice resolution.

Figure 3.6: Increased lattice resolution comparison.

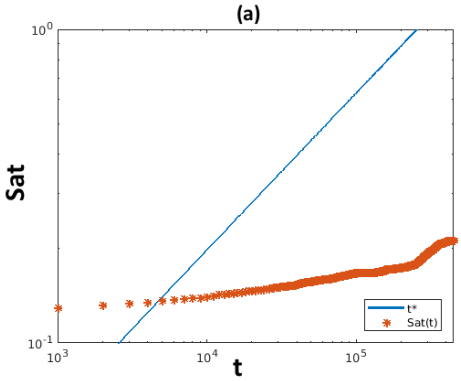

(a) $\theta_c = 82, h = 35$, increased simulation time.

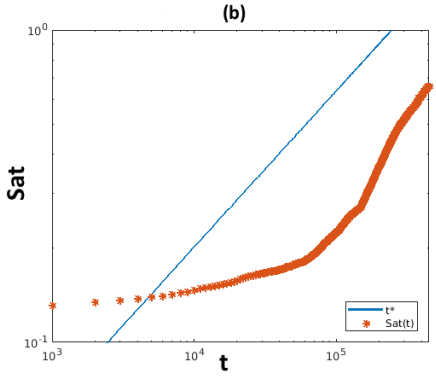

(b) $\theta_c = 82, h = 50$, increased simulation time.

Figure 3.7: Comparison of results with increased simulation running time.

they were run using a slightly updated definition of the contact angle however testing verified this modification had negligible impact on the result.

While it is clear that by decreasing the contact angle (creating a more hydrophilic surface) we can improve infiltration it ws more interesting to examine the case of a near-neutral material as it is here the role of the microstructure becomes more important on the infiltration process. This is relevant because some soils will contain substrates with near-neutral materials as with the LECA we introduced earlier and rainfall does not usually create extreme ponding effects wherein the hydrostatic pressure will be overpowering. If we consider the possibility of long drying periods on the substrate we further our case for the validity of such a study as desiccated soil tends to be more hydrophobic, as in the case of flash flooding in desert environments. We therefore choose to fix the contact angle of our material at this near-neutral angle of $\theta_c = 82°$ and proceed to examine the effect of the porous microstructure on infiltration dynamics.

3.8.2 Evolution of saturation

Once certain that the results were not misleading due to numerical or resolution issues, the underlying physical process causing the infiltration retardation was investigated in detail. This investigation began with an analysis of the saturation for a host of new simulations with updated parameters. In all subsequent simulations and their respective results the contact angle has been fixed to $\theta_c = 82°$. Table 3.6 identifies the six cases as presented in Paper 2 in terms of ϕ and Bo. Before we provide any

Table 3.6: Case specifications.

	Case 1	Case 2	Case 3	Case 4	Case 5	Case 6
ϕ	6.7	10.1	5.1	6.7	10.1	5.1
Bo	8.92	8.92	8.92	3.96	3.96	3.96

analysis we note that we use the term homogeneous to describe the porous medium with respect to the packed bed. It is important to say that due to the thickness of our medium there will be differences in the packing due to the nature of the random packing at the base of the medium. We would therefore encounter a layering effect if a periodic condition were used in the vertical direction. This consideration is taken into account by the introduction of a packing parameter which quantifies this inherent anisotropy.

In Figure 3.8, saturation Sat is plotted as a function of dimensionless time for Bo $= 8.92, 3.96$. The dimensionless time is defined as

$$t^* = \frac{t}{\sqrt{\frac{h}{g}}}. \tag{3.60}$$

It can be seen that the infiltration for all values of ϕ displays a trend with a slope ≤ 0.5 in logarithmic scale, which matches the theoretical solution of Washburn's equation (Washburn 1921) which describes the relationship between penetration length l_p of a liquid into a fixed-radius capillary tube over time without gravitational forces. Washburn's equation does not take into account gravity and thus in our case only can act as the roughest of guides as to the observed behavior. In our case gravity is the force that drives liquid penetration rather than the contact angle.

Rather than a single tube we are trying to capture liquid infiltration into a porous complex structure, thus the physical description is more complicated, The infiltration is affected by the surrounding pore network and thus infiltration rate can be increased or decreased based upon the distributions in the neighboring pores and can also be intermittent, as recently observed in experiments of two-phase flows into rock samples (Reynolds et al. 2017). This type of behavior occurs more prevalently at low values of porosity and Bond numbers, such as the ones considered here. Since we are within the regime of low values for the parameters we justify the use of a power law similar to that of Washburn as a guide to analyze the flow dynamics; thus at the macroscopic scale, on average, the saturation of the porous medium follows a

law as:

$$Sat(t) \quad \propto \quad (D_c t)^{\alpha(t)}. \tag{3.61}$$

In this formulation the diffusive coefficient is a consequence of the hydraulic pressure and the porous microstructure and alpha is a time-dependent exponent $\alpha(t) \leq 0.5$ as seen in Figure 3.8 in the form of triangles.

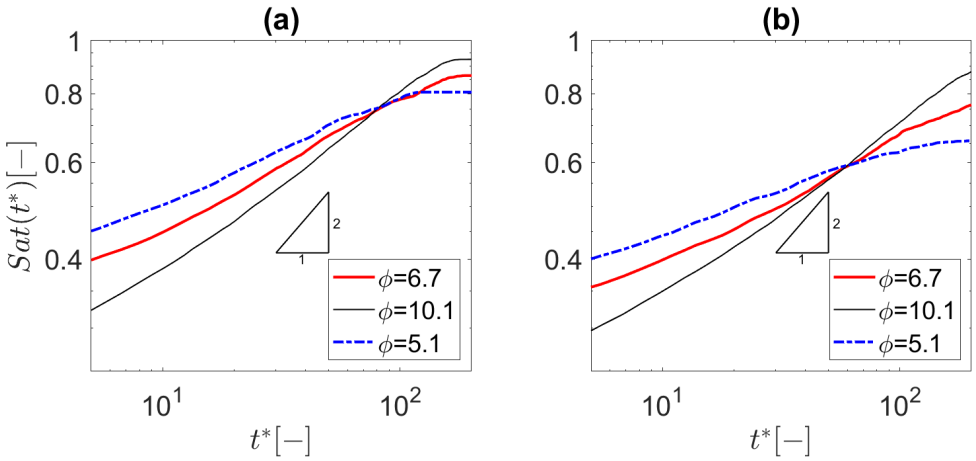

Figure 3.8: (a) Log-linear plot of saturation as a function of dimensionless time for $\phi = 6.7, 10.1, 5.1$ with Bo $= 8.92$. (b) Log-linear plot of saturation as a function of dimensionless time for $\phi = 6.7, 10.1, 5.1$ with Bo $= 3.96$.

We note the differences in initial saturation are due to the particle packing at the surface which is not uniform for all cases. The mid-range saturation values for $\phi = 10.1$ follow Eq. (3.61) with slope 0.5 indicating a flow behavior similar to a single pore penetration.

It is important to stress here that $\alpha = 0.5$ is recovered if we have a constant pressure difference at inlet and outlet of the medium and a constant capillary pressure. In reality, while we can neglect pressure gradients in the less viscous gas phase, we have a variable inlet hydrostatic pressure over the medium which decreases with increasing saturation of the medium. This can explain the values of α lower than 0.5 as evidenced here.

For larger particle sizes the infiltration is less efficient and the decreased hydraulic pressure has an additional adverse effect on the infiltration. As saturation approaches $0.7 - 0.9$ the values almost stagnate for several of the cases indicating an infiltration reduction not heavily dependent upon the flow itself but rather the porous microstructure. This may also be attributed to the influence of the packing near the bottom boundary, and appears to be influenced also by particle size. These postulations were investigated in more detail by examining the pore microstructure directly.

3.8.3 Microstructure quantification, porosity and pore size

Figure 3.9 displays the planar porosity as a function of distance from the porous medium base ($H = 70$), measured in particle diameters d. This value is calculated

by simply summing all void nodes in a 2D plane and dividing by the total planar area. As predicted, at the base of the porous medium the particles are more ordered

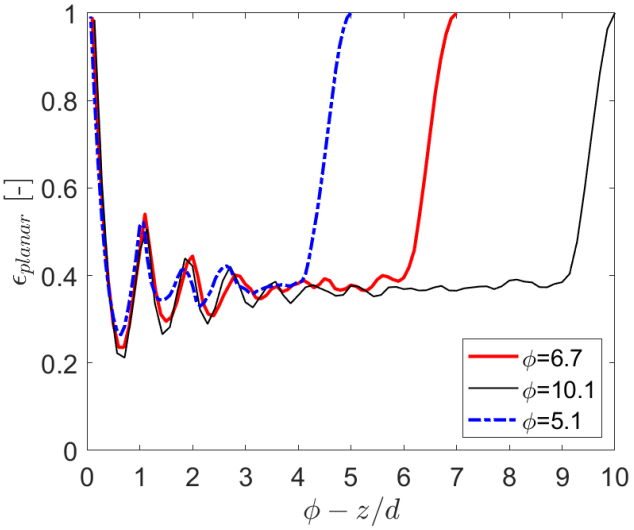

Figure 3.9: Flow-normal planar porosity ϵ_{planar} as a function of particle diameters d from porous medium base for $\phi = 6.7, 10.1, 5.1$.

however this boundary effect is lost thereafter until the surface is reached. We also observe that when $\max(Sat) \approx 0.8, 0.85, 0.9$ is reached for $\phi = 5.1, 6.7, 10.1$ the infiltration rate is dramatically reduced when the liquid front approaches the bottom at a distance of approximately one particle diameter. This interval over the last particle layer is accompanied by a sudden increase in the value of porosity, which suggests that pore throat expansions can act to impair liquid infiltration.

Several attempts were made to quantify the pore microstructure, which is a challenging undertaking when one considers that we are working in full 3D. Attempts have been made, such as by Suh et al. (Suh et al. 2017) and Liu et al. (Z. Liu et al. 2017b). We have opted for characterization by analyzing porosity and pore sizes in the plane lying perpendicular to the primary flow direction. One can measure the volume of each pore to a point however this gives no information on its size or shape thus an approach applying image analysis was used. Rather than attempt any kind of 3D categorization an equivalent pore diameter was calculated for each pore present on every 2D slice of the microstructure. The slices were taken perpendicular to the primary flow direction. Individual pore size distributions based upon this equivalent pore diameter have been calculated for each porous domain and the mean and standard errors at specific depths are plotted in Figure 3.10 as a function of distance from the porous medium base, measured in particle diameters. The standard error is computed as

$$s_{\overline{x}} = \frac{s}{\sqrt{n}}, \tag{3.62}$$

where s is the sample standard deviation and n is the sample size. The jump visible at the base of the porous medium corresponds to the top of the first particle layer before the randomness of the packing truly takes hold. This matches the oscillation

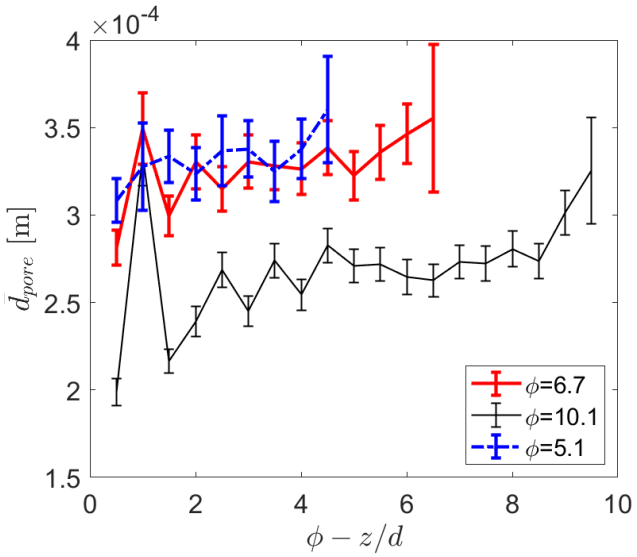

Figure 3.10: Pore diameter d_{pore} mean with standard error as a function of particle diameters d from porous medium base for $\phi = 6.7, 10.1, 5.1$.

we mentioned in the planar porosity and affirms the assumption that the oscillation is due to the boundary influence. We see the standard errors for each particle increase from the smallest particle size to higher largest particle size, meaning the distribution of pore sizes is greater for larger particles. The standard errors averaged over the depth of the medium are $\overline{s_{\overline{x}}} = 0.2, 0.14, 0.26$ for $\phi = 6.7, 10.1, 5.1$ respectively, which confirms that the larger particle size and the uniformity of packing near the surface is relevant at the individual pore level.

A method by which pore connectivity was also measured was attempted however this became very difficult to quantify in any meaningful way. The locations and sizes of the pores were taken from the previous image analysis of the 2D domain cuts. Figure 3.11 shows early attempts to visualize the pore networks for a few cases. One issue encountered in this quantification was deciding the threshold for extrema with regard to pore throat size. This would require a record of previous pore locations along with their respective diameters and comparison must be made between all neighboring layers to ascertain accurate connectivity information. An added complication is the branching of pores and directional considerations other than those purely in the main flow direction. After consideration this method was scrapped in favor of probabilistic representations of the pore size distributions.

3.8.4 Impact of interfacial area

Figure 3.12 gives the dimensionless liquid-gas interfacial area for each geometry as a function of dimensionless time. The clearest visible trends within the figures are the general slopes for all cases. When $\phi = 10.1$ and $\phi = 6.7$ we see a decrease over time in interfacial area for both hydraulic heads. The slope of the $\phi = 5.1$ case seems instead to oscillate around a constant value. The overall oscillation in interfacial area is indicative of liquid buildup at pore throats and subsequent sporadic jumping

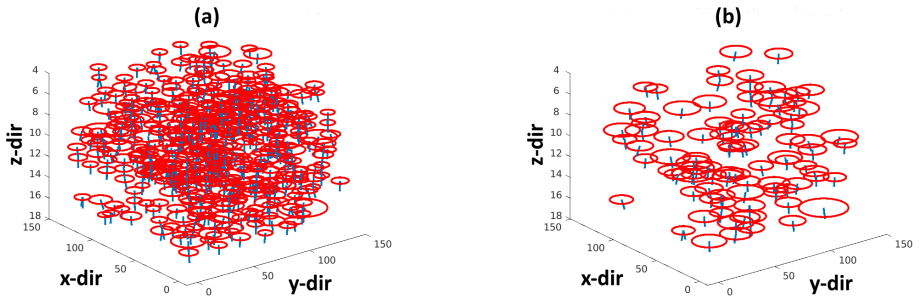

(a) $\phi = 6.7$, minimum radius size 5 lu. (b) $\phi = 6.7$, minimum radius size 8 lu.

Figure 3.11: Pore connectivity representations, red circles represent pores and blue lines to which other pores they connect.

patterns of pore saturation. The $\phi = 5.1$ case displays small fluctuation amplitudes, suggesting slower infiltration in time. The underlying cause of the intermittent

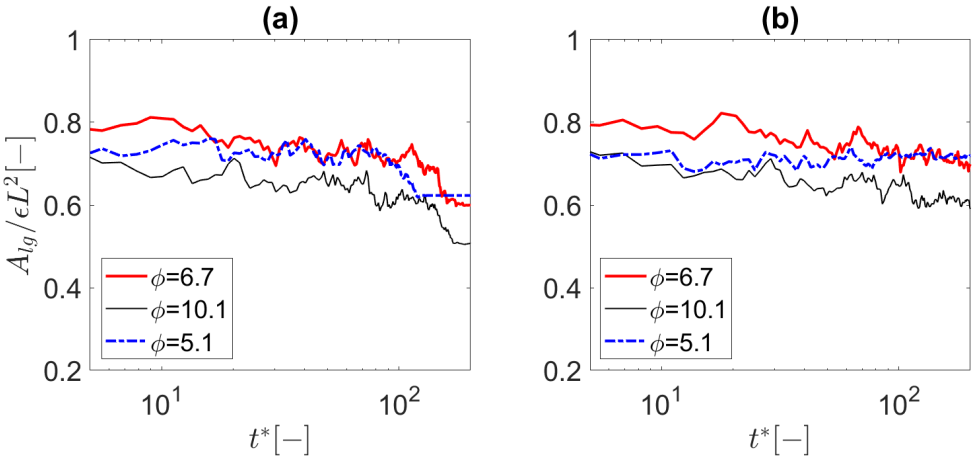

Figure 3.12: (a) Dimensionless liquid-gas interfacial area $A_{lg}/\epsilon L^2$ as a function of dimensionless time t^* for $\phi = 6.7, 10.1, 5.1$ with Bo $= 8.92$. (b) Dimensionless liquid-gas interfacial area $A_{lg}/\epsilon L^2$ as a function of dimensionless time t^* for $\phi = 6.7, 10.1, 5.1$ with Bo $= 3.96$.

behavior of liquid-gas area buildup and possible stagnation lies in the balance of forces acting in the capillary structure and has been mathematically formalized in Cassie and Baxter (Cassie and Baxter 1944) for describing the mechanical balance responsible for the behavior of droplets leaning on rough surfaces. The same concept has been applied for describing the rapid pore-scale displacement known as Haines jump (Haines 1930). We can formalize such a force balance by applying the principle of Helmholtz free energy F which describes the thermodynamic balance of a isochoric and isothermal system as in (3.63). This formulation is valid under the assumption

of low capillary numbers where viscous forces can be considered negligible.

$$
\begin{aligned}
dF &= \delta W < 0 && (3.63)\\
&= -\sum_{i=w,nw} p_i dV_i + \gamma dA_{lg} && (3.64)\\
&= -(p_w - p_n w)dV_w + \gamma dA_{lg} && (3.65)\\
&= -p_c d(Sat\ V_f) + \gamma dA_{lg} && (3.66)\\
dF^* &= -\frac{p_c V_f}{\gamma} + \frac{dA_{lg}}{dSat} < 0 && (3.67)\\
V_f &= \epsilon V_{tot} && (3.68)
\end{aligned}
$$

where p_w, p_{nw}, p_c are the liquid, gas and capillary pressure, respectively; V_l, V_f, V_{tot} are the liquid, total void, and total volume; and A_{lg} is the liquid-gas interfacial area. Applying the concepts of thermodynamics of surface tension we rewrite Eq. (3.63) as Eq. (3.64). This equation represents the maximum amount of reversible work done by such a system, and with a few algebraic manipulations the resulting relation is given in Eq. (3.67).

This equation clearly shows the relationship between the interfacial area derivative and capillary pressure. This relationship determines the energy balance of the system: in presence of an interfacial area expansion, the capillary pressure term must compensate to facilitate liquid infiltration. This energy requirement can explain why drastic expansions, as the one induced by the packed microstructure at the bottom of the medium, can considerably reduce infiltration rate and possibly impede it. The continuous liquid buildup at the pore throat and rapid pore invasion mechanisms induced by packed microstructures give rise to intermittent infiltration behavior at pore-level and an anomalous reduced infiltration rate at the macroscopic scale.

Thus to further evaluate this formalized requirement we plot in Figure 3.13 the interfacial area as a function of saturation for all cases. In Figure 3.13(a) and 3.13(b) where infiltration occurs the general slope is negative so that the inequality in Eq. (3.67) is easily satisfied and infiltration occurs uniformly. In Figure 3.13(c) it is clear that especially under lower hydraulic pressure the area does not significantly decrease with saturation, indicating that Eq. (3.67) is possibly not satisfied in some pores and total infiltration of the medium is slowed down. In addition, infiltration fails when the area-saturation derivative is not sufficiently steep after some small initial increase. When this derivative condition is reached infiltration occurs, however this condition must be maintained for increasing saturation for the process to continue. If the interfacial area increment is too large to be sustained by the capillary pressure, infiltration will stop, causing the packed bed to act like a capillary barrier.

Ross (1990) discussed capillary barriers and determined criteria for their size and liquid diversion capacity in analytical terms (Ross 1990). Diversion capacity in this case refers to the amount of liquid that can be channeled in a lateral direction by the interaction between an upper and lower layer of different sized particles. It is important to note that while the effect has been noted and studied, the conditions for the phenomenon to affect the infiltration process from a morphological perspective have not been quantified, to the best knowledge of the authors. This phenomenon

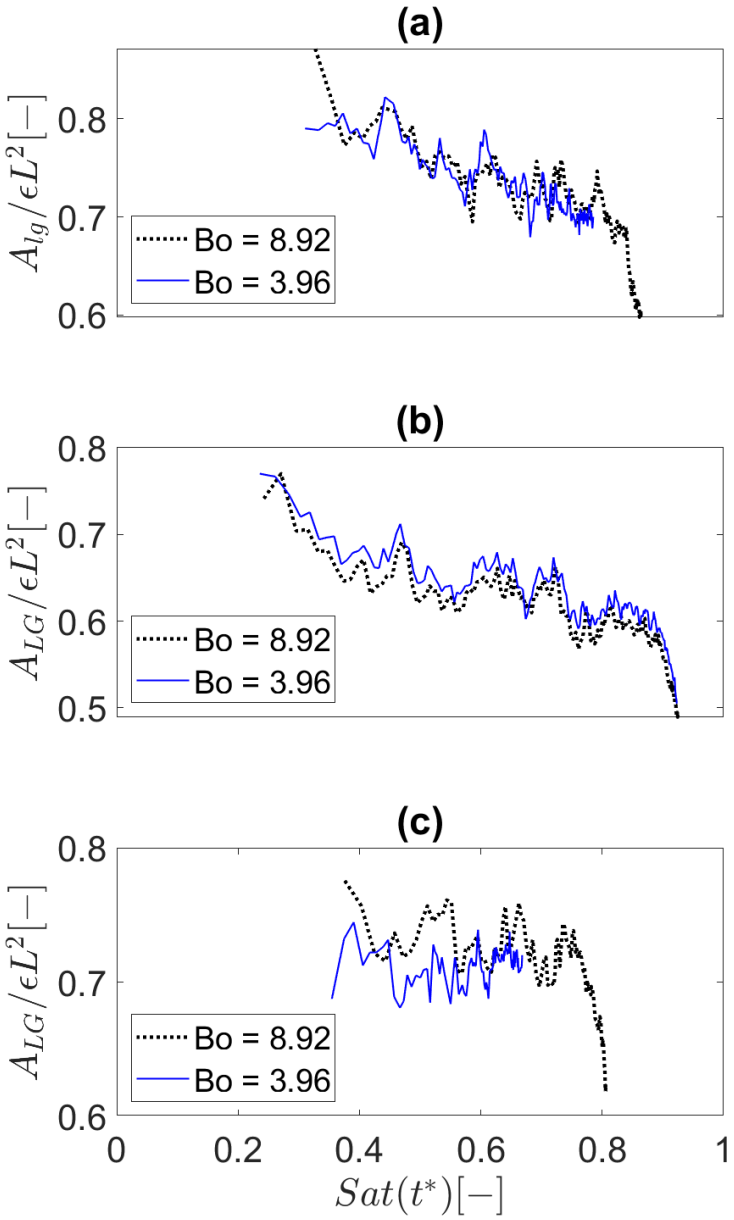

Figure 3.13: Dimensionless liquid-gas interfacial area $A_{lg}/\epsilon L^2$ as a function of saturation $Sat(t^*)$ for $\phi = 6.7$ (a), $\phi = 10.1$ (b), and $\phi = 5.1$ (c).

clearly plays a role in infiltration dynamics, even when contact angles are near neutral. The morphological impact on liquid infiltration is expected to increase when the contact angle is reduced; thus quantifying its influence is of importance for cases with variable saturation, as is the case with rainfall infiltration of soils. An investigation of the capillary pressure should provide more insight on this issue.

3.8.5 Effective capillary number

Dimensionless parameters

We now introduce another parameter representing the dimensionless wetting phase height is given as $h^* = h/d$. This parameter represents a measure of the approximate pore sizes in the microstructure against the applied hydrostatic pressure from the surface. This gives us the final characteristic quantity: the pore-scale characteristic capillary number,

$$Ca_c = \frac{u_c \mu_w}{\gamma}, \tag{3.69}$$

$$u_c = \frac{\rho_w g d^2}{\mu_w}, \tag{3.70}$$

where u_c is the pore-scale characteristic velocity. The pore-scale capillary number represents the importance of gravity-induced viscous forces over surface tension at the pore scale. The values for each of the dimensionless parameters is given in Table 3.7. The porous subdomain thickness in case 2 and 6 are modified, thus the particle size is slightly reduced to keep the packing ratio the same, however the hydrostatic pressure applied is unchanged.

Table 3.7: Dimensionless quantities for each case, grouped by ϕ.

Case #	ϕ	h^*	Ca_c
1	10.1	10	0.041
2	10.1	13	0.025
3	10.1	15	0.041
4	6.7	6.7	0.092
5	6.7	10	0.092
6	6.7	11.3	0.074
7	5.1	5	0.167
8	5.1	7.5	0.167
9	5.1	15	0.167

We examine the interdependence of velocity and saturation Sat by plotting the effective capillary number Ca_{eff} as a function of saturation in Figure **??**. The effective capillary number is given by

$$Ca_{eff} = \left(\frac{dSat}{dt} H\right) \frac{\mu_w}{\gamma} = U \frac{\mu_w}{\gamma}, \tag{3.71}$$

where the velocity is given by the rate of overall stream-wise infiltration over time. Saturation is calculated by summing the total nodes occupied by the wetting phase and dividing by the total available void space within the porous domain subsection. In Figure 3.14 we see an overall decrease in velocity as the saturation increases for all cases. This decrease of Ca_{eff} as a function of saturation remains overall

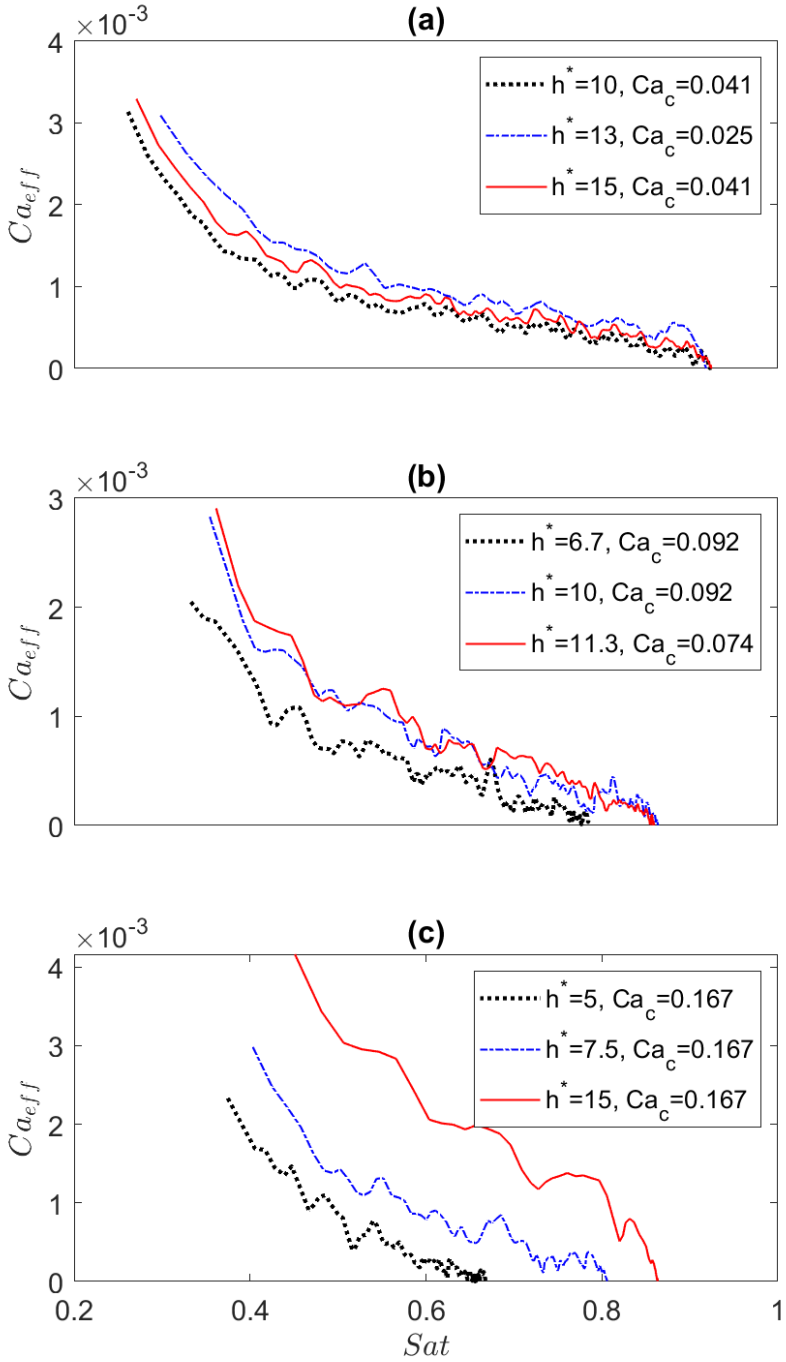

Figure 3.14: (a) Effective capillary number Ca_{eff} as a function of saturation, $\phi = 10.1$. (b) $\phi = 6.7$ (c) $\phi = 5.1$. Approximately $Ca_{eff} \propto 1/Sat$ after initial infiltration stage.

constant after the initial phase of infiltration through the uppermost layer. This can can attributed to our definition of the infiltrating velocity and the increasing viscous resistance to the infiltration fluid as saturation increases. If one assumes the derivative of Ca_{eff} with respect to saturation remains constant then as the rate of saturation increase in time is reduced, we must have a complementary increase in the viscous resistance.

It can also be noted that h^* plays little to no role in the determination of the velocity, as the curves are largely similar. When the packing parameter is larger as in (a) and (b) we see little effect of particle size on the infiltration velocity; however when the medium is very thin compared to the particle size as in (c), we observe a larger variation in the infiltration rate along with little distinction between the initial stage and subsequent infiltration rate. This observation suggests that in the presence of large pore sizes and thin layers, the magnitude of the hydraulic pressure has a substantial effect on the flow dynamics, given also that dynamic effects and gravitational forces at the pore scales, (larger Ca_c), become important. This impact on the fluid velocity can be better understood when one examines the capillary pressure within the porous network.

3.8.6 Effective capillary pressure

To examine this phenomenon from the pore-scale interactions, we plot the capillary pressure present across the phasic interface within the porous medium. While it is difficult to determine this pressure difference in every location within the pore network, we can use the fact that we are working with thin porous media to look at the spatially averaged capillary pressure across the full interface. In addition to this consideration we also note that since the full volume is included, viscous forces are included as well. Thus when we observe a high $p_{c,eff}$ value at high Ca_{eff}, we may have both effects: a high velocity and high viscous pressure drop and/or a high (positive) capillary pressure. In either case $p_{c,eff}$ represents the total contribution of forces opposed to the flow rather than an isolated one.

The wetting phase pressure is calculated by summing the density values for the wetted nodes and the non-wetting pressure at the non-wetted nodes and dividing by node count appropriately. This approach cannot account for non-wetting phase pockets that remain trapped within the microstructure however we argue that due to the thin nature of the medium in question we can reasonably assume the interface is largely along the wetting front.

In Figure 3.15 we plot the effective capillary pressure-saturation curves and see a correlation regarding particle size and flow behavior, with the larger particle sizes exhibiting hydrophobic characteristics. The effective capillary pressure is defined to be the capillary pressure divided by the ratio of surface tension to particle size. This formulation differs slightly from that of Weitz et al. (Weitz et al. 1987) in that we substitute a characteristic pore throat radius for particle size, which have been determined to be of the same magnitude.

$$p_0 = \gamma/d, \tag{3.72}$$

$$p_{c,eff} = (p_w - p_{nw})/p_0. \tag{3.73}$$

In Figure 3.15 we observe a variation of the average values of the effective capillary

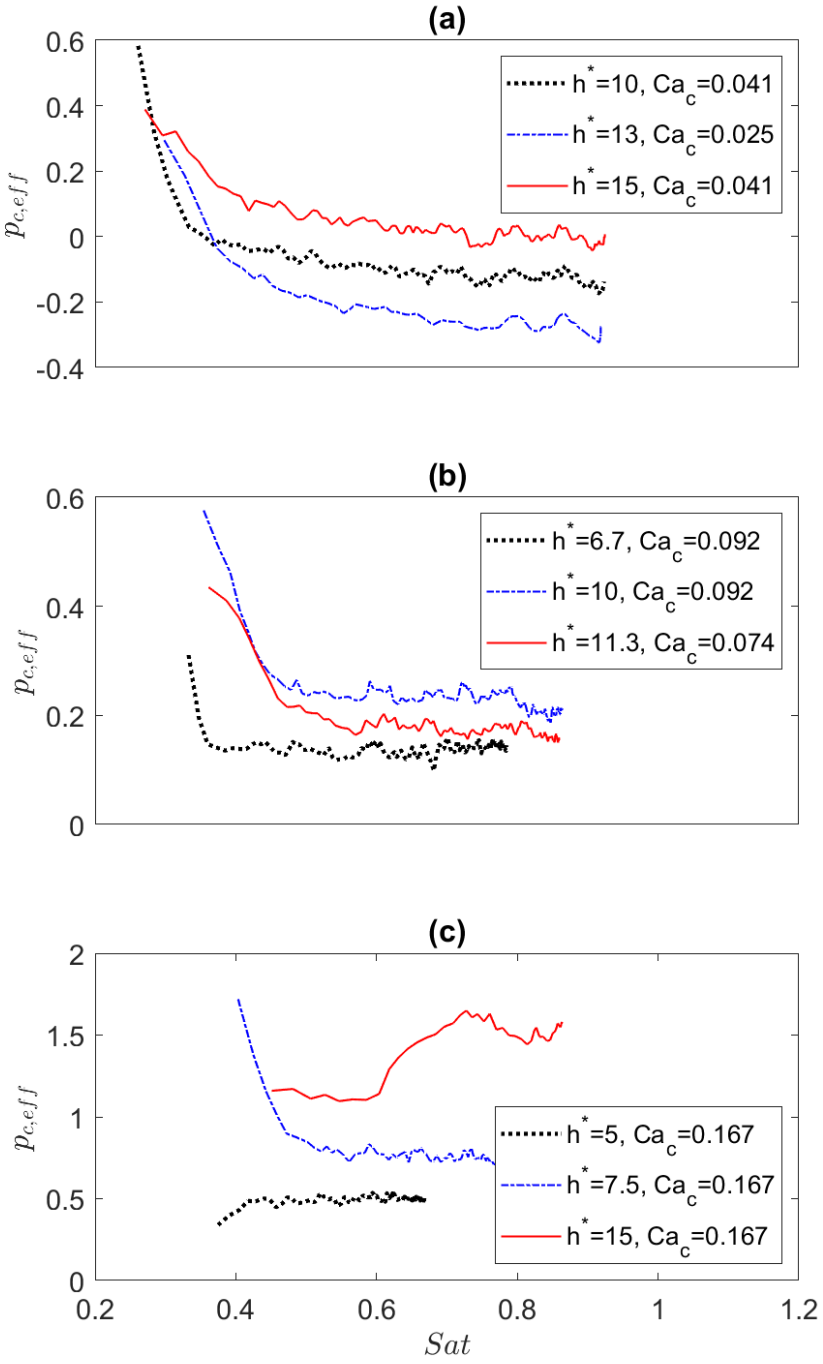

Figure 3.15: (a) Effective capillary pressure $p_{c,eff}$ as a function of saturation, $\phi = 10.1$. (b) $\phi = 6.7$ (c) $\phi = 5.1$. Positive capillary pressures represent capillary forces acting against the flow gradient; negative ones represent capillary suction.

pressure: in the case of a small particles compared to the layer thickness as in (a), the capillary pressures increase along with hydraulic head (h^*) or pore scale velocity (Ca_c), from negative values (suction) to slightly positive ones. This trend indicates that as we increase the pressure head we observe less pronounced suction induced by the hydrophilicity of the material. A similar effect is observed when increasing Ca_c, analogous to decreasing the strength of surface tension forces. This last observation also explains why in Figure 3.14 (a) the Ca_{eff} exhibits a high value for low Ca_c; as the infiltration rate is strongly sustained by the hydrophilicity of the medium. In (b) we observe a similar but less pronounced trend and we notice that the average values of the effective capillary pressure are all positive, implying the the contribution of capillary suction is no longer dominant. In (c), when the particle size is comparable with the thickness of the medium, we again observe a significant increase of $p_{c,eff}$, suggesting again that the hydraulic pressure exerted at the pore level contributes heavily to the capillary pressure dynamics.

In Figure 3.15 we also see the capillary pressure remains fairly stable throughout the simulations for most of the cases however the range of saturation values varies significantly. In some cases the infiltration is fairly constant, experiencing small changes in dynamic capillary pressure as new pores are filled however this isn't true for all cases. Generally speaking, we observe that oscillations in capillary pressure tend to increase as its average value increases, from negative (indicating hydrophilic behaviour of the effective dynamics) to positive values (indicating a medium that acts as a hydrophobic one).

The cases with larger particles exhibit the behavior of a valve-like barrier on the flow as defined by positive values of capillary pressure. In this case the meniscus on the interface is convex in the direction of wetting phase flow. This positive capillary pressure has been found to appear in cases with higher initial fluid velocity as described by Weitz et al. (Weitz et al. 1987). Weitz et al. showed that dynamic capillary pressure is dependent upon this initial fluid velocity. This effect has also been observed in cases where a non-wetting fluid is displacing a more dense wetting fluid under gravitational forces (Løvoll et al. 2011).

In the cases investigated herein a more dense fluid is invading a less dense one. In such a case we observe a similar general dynamic trend of the capillary pressure, whereby increasing the hydraulic head and the infiltration velocity, we notice an increase of the capillary pressure. However, we also observe a marked effect of the packing parameter, determining the porous microstructure. This observation tells us that it is possible to regulate the capillary pressure by modifying the particle size as a means to regulate the the flow behavior within the system. In addition to this insight, we can examine the impact of velocity and consequently, dynamic capillary pressure, on infiltration homogeneity.

3.8.7 Infiltration homogeneity

In Figure 3.16 we plot the probability distribution functions (PDFs) of infiltration depth at timestep $t_{lb} = 250,000$ and examine the resultant distributions. In these cases homogeneous infiltration is characterized by a singular spike near 0 whereas

less homogeneous flow is shown by bimodal behavior as well as less extreme slopes. In (a) we see two of the three cases exhibit a tighter distribution around the mean infiltration depth, denoting a more homogeneous wetting front; however the case with higher hydraulic pressure exhibits less homogeneity. In both (b) and (c) we see similarly less homogeneous infiltration patterns with the exception of the case where $h^* = 15, Ca_c = 0.167$ where once again the infiltration appears more homogeneous. This aberration in the results can be explained by the quick convergence of this case to an equilibrium state due to the thickness of the porous layer in combination with the high hydraulic pressure applied. The general observed trend suggests that when increasing the hydraulic pressure and the pore size compared to the layer thickness; while the flow exhibits higher infiltration rates, the suction mechanism (hydrophilicity) is inhibited and an adverse effective capillary pressure arises. This pressure induces less homogeneous infiltration patterns. In observing this trend of less homogeneous flow for larger particle sizes, we have shown that by applying an initial hydrostatic pressure above a certain threshold to the system and by increasing the particle size we can increase the dynamic capillary pressure (as defined in this work) and generate the conditions under which the porous medium acts in a hydrophobic manner, slowing the resultant wetting phase velocity within the pores. This lower velocity generates higher occurrences of fingering, which is consistent with the works of Weitz et al. (Weitz et al. 1987) and Cueto-Felgueroso and Juanes (Cueto-Felgueroso and Juanes 2008). Thus by choosing a particular particle size one can effectively determine the infiltration rate of the system by bringing about the conditions wherein an inherently hydrophilic or borderline material can act in a hydrophobic manner.

This particular property can be of use in designing green roof soil substrates where a particle size can chosen with a specific hydraulic load to behave in a hydrophobic manner and slow pore infiltration. By layering differently sized particles one can create a system that acts differently under different hydraulic loads without resorting to overly-thick individual layers. This can reduce material use and weight applied to the structure, depending on the material chosen.

3.9 Conclusions and Future Work

3.9.1 Implications for green roof substrate design

In this section the direct consequences of the previous investigations will be discussed. We begin by examining the impact of packing and infiltration rate. This rate is quantified by α which is the exponent of the power law. In Figure 3.17 we plot the value of alpha as a 'function' of the Bond number and the packing ratio. α can be considered as a measure of the ability of the microstructure to detain the infiltrating rainfall, with higher values corresponding to more rapid infiltration and shorter detention time. Therefore it is recommended to consider the microstructure with regard to depth and particle size in the design of a green roof, particularly when including thin substrate layers, when the thickness of the medium and the particle size are of the same magnitude. We see that there are changes in the behavior of the

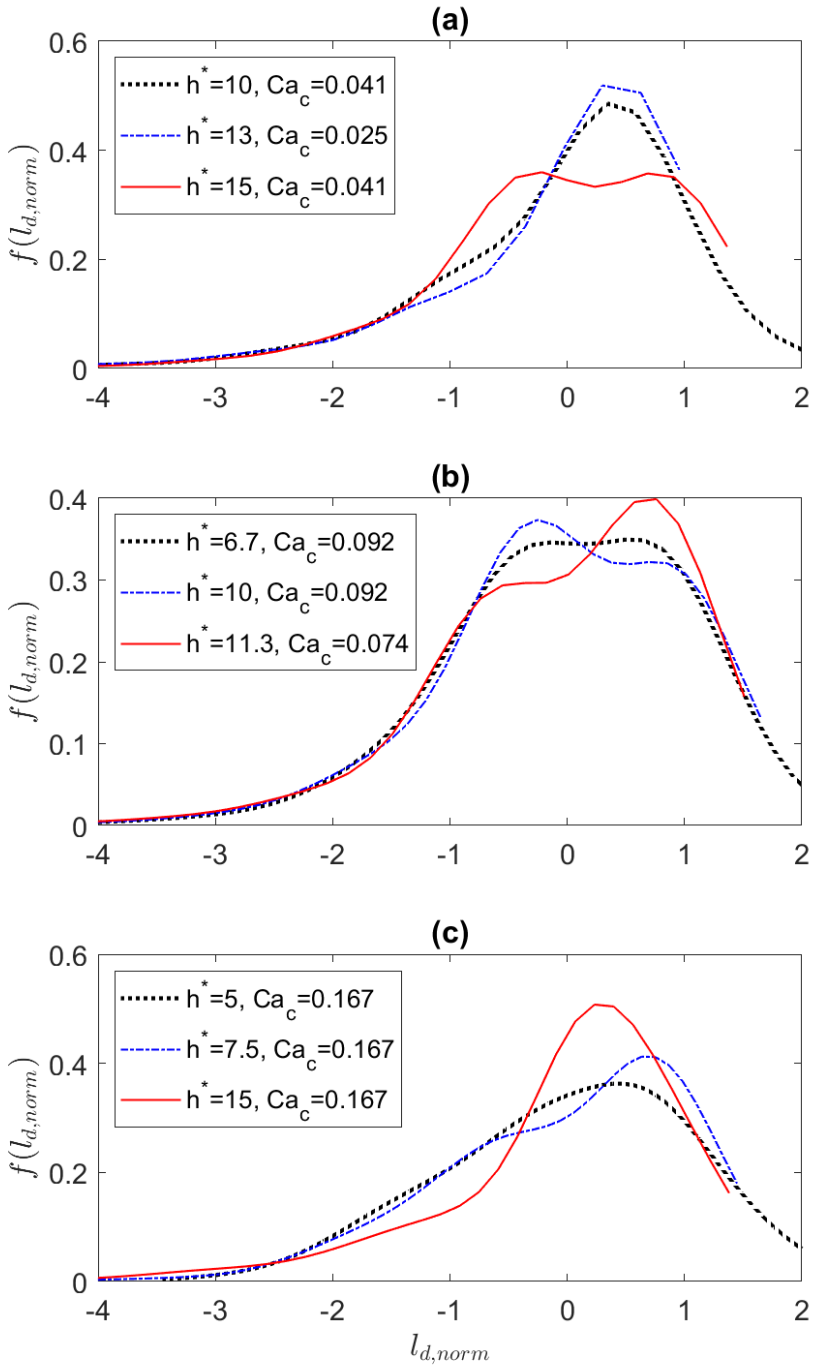

Figure 3.16: PDFs ($f(l_{d,norm})$) of normalized wetting phase infiltration depth ($l_{d,norm}$) as given in standard errors from mean infiltration depth. Single high peaks near $l_{d,norm} = 0$ indicate highly homogeneous infiltration.

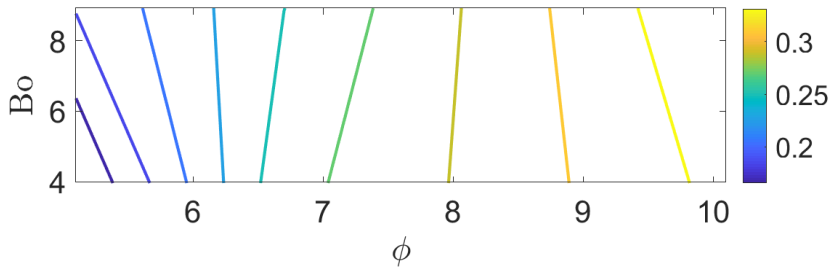

Figure 3.17: α extracted at intermediate times from Figure 3.8 plotted as a function of ϕ and Bo.

infiltration rate for lower packing ratios however the system improves dramatically when the packing ratio is increased, even with lower rainfall intensities. To examine these findings in more detail, we look at the pore-scale velocity, capillary pressure, and their interplay with the microstructure.

In order to get a better idea of the interdependence of the velocity, capillary pressure, saturation, and microstructure we attempt to collapse all cases onto a single curve. Figure 3.18 displays the time-averaged Reynolds number as a function of the effective capillary pressure. The averages for the Reynolds number and the effective capillary pressure are calculated as shown:

$$Re(t) = \frac{dSat}{dt} H \frac{d_p}{\nu_w}, \tag{3.74}$$

$$\overline{Re} = \frac{1}{Sat(t_{end})} \int_{t=0^+}^{t_{end}} \left(Re(t) \frac{dSat(t)}{dt} \right) dt, \tag{3.75}$$

$$\overline{p}_{c,eff} = \frac{1}{Sat(t_{end})} \int_{t=0^+}^{t_{end}} \left(p_{c,eff}(t) \frac{dSat(t)}{dt} \right) dt. \tag{3.76}$$

The time averaging neglects the first time instances wherein the infiltration rate constitute outlier values due to initialization of the infiltrating liquid. Thus $t = 0^+$ represents the second saved iteration and $t = t^{end}$ represents the final saved iteration. In Figure 3.18 the results have been plotted and grouped by packing ratio, with the lower hydraulic pressures in each group to the left of their higher counterparts within each group. The points show the correlation between capillary pressure and velocity across the threshold from negative to positive values of capillary pressure. A similar relationship is shown for instance in Weitz et al. however in that work the dynamic contribution to capillary pressure is related to velocity by the equation

$$\Delta p_c(u) = \gamma / r_{th}(-1 + K N_{Ca}^x), \tag{3.77}$$

$$N_{Ca} = \mu U / \gamma. \tag{3.78}$$

where γ / r_{th} is the static pressure required to de-pin the phasic interface and r_{th} is some characteristic pore throat radius. N_{Ca} is the capillary number and K, x are fitting parameters representing the strength of the dynamic contribution, dependent upon initial velocity. Rather than using the capillary number we choose to use the Reynolds number as our microstructure is dissimilar across our cases; which

is held constant in their work. In the Weitz formulation the exponent x would be valued differently due to the nonlinear dynamic capillary term coefficient utilizing the pore throat radius and including the capillary number as opposed to the Reynolds number. In addition Weitz et al. controlled the entry velocities whereas in our case the velocities are measured as a consequence of the the infiltration dynamics. By controlling the inlet velocities an external forcing of the flow is assumed whereas by allowing gravity and capillary suction to drive the flow no such contribution is applied. This allows for a dynamic measurement of the flow and its properties as a direct consequence of the microstructure. Despite the difference in model parameters we see a striking similarity in the results when we apply a least squares fit of our collapsed data points to the modified equation of Weitz et al., as shown in Figure 3.18. The cases with the highest ϕ value exhibit a lower effective capillary pressure, with

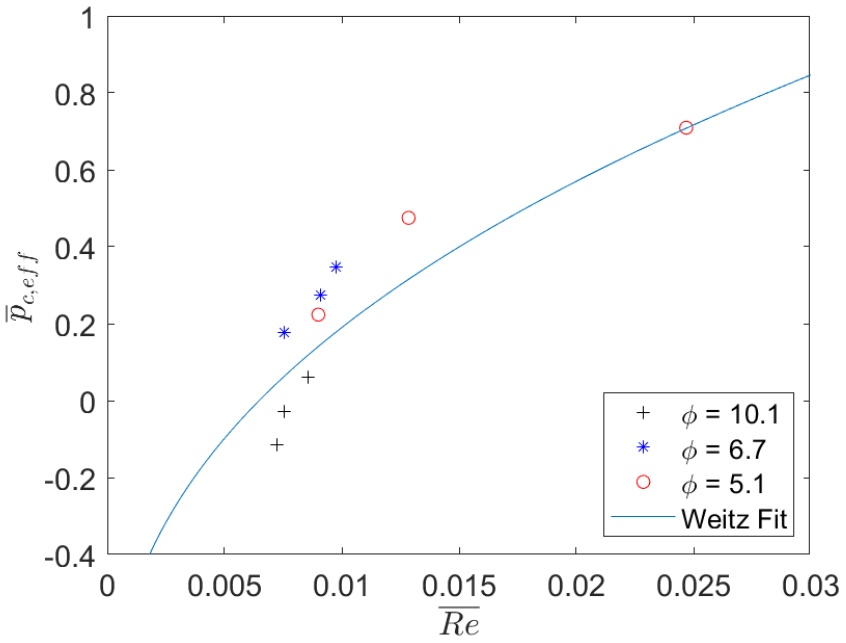

Figure 3.18: Collapsed curve of mean effective capillary pressure as a function of Reynolds number. All cases represented, grouped by packing ratio ϕ. Weitz fit given by $\overline{p}_{c,eff} = -1 + 7.508\overline{Re}^{0.4}$

little variation in velocity when the hydrostatic pressure is increased. They range from capillary suction dominated to more neutral in terms of the driving force for infiltration. The clustering remains similar for $\phi = 6.7$ however the capillary pressure is shifted more in the positive direction, denoting decreasing influence of capillary suction driven infiltration. Finally, for the smallest value of ϕ we see a wide range of velocities, denoting a much stronger dependence of the infiltration on the applied hydrostatic pressure. The capillary pressure increases with more responsiveness with this increased hydraulic pressure when the medium thickness and particle size are of the same magnitude. From this we can state there is a correlation between the choice of particle size and infiltration dynamics in thin homogeneous porous media.

This model allows us to represent the effects of the microstructure and the resulting velocity on the capillary pressure present within the medium.

3.9.2 Applicability of the results

If one considers how these results can be combined with previous research into green roof performance there are a few points to consider. Firstly, we stress here that we have considered only the growth substrate and no vegetation is included. If vegetation is included we must consider the mechanical blocking effect at the surface however this simply reduces the quantity of surface water for infiltration. In addition, root networks will disturb the soil matrix and contribute to small channels throughout the medium where liquid can flow more easily. These channels may contribute to areas in the substrate where liquid will not reach as frequently and will be more hydrophobic. From a larger time scale the impact of evapotranspiration must be considered, however this process primarily affects the retention capacity of a green roof as it removes trapped water from the smallest pores rather than the liquid able to infiltrate and drain out of the soil. Most green roof constructions also include a drainage layer directly beneath the root barrier layer and growth substrate layer. This means that at the base of the growth substrate the packing will resemble the physics where wall impacts will be significant.

Despite the limitations listed above, these parametric design visualizations can be invaluable from a design perspective to understand the behavior of the packing ratio and rainfall intensity on infiltration velocity. This observed velocity can be related directly to the capillary pressures of different substrates prior to extensive testing. By applying the results presented here one can design the substrate on a variety of parameters that influence each other and gain some idea of the substrate behavior prior to any *in situ* testing. Additionally there is merit in considering the climatic conditions in the location of installation as by taking local rainfall quantities into account in the design, it is possible to optimize the roof performance for extreme conditions where the benefit of a green roof is maximized. It is also possible to layer different particle thicknesses so as to create a substrate that is designed to perform optimally under variable conditions. By designing substrates with these parameters in mind one can achieve the desired detention of rainfall in a green roof. Though these tools are useful there is much to be explored in this field, particularly when one considers the dynamic effects of saturation, capillary pressure and the resultant infiltration velocities when restrictions on the microstructure are placed to impede infiltration but not prevent it. A comparison of the behaviors presented in this chapter against real substrates is undertaken to determine if any of the trends identified in these works can be observed using real-world microstructures.

3.10 Impact of topological heterogeneity on liquid infiltration of a thin growth substrate using XMT scans

3.10.1 X-ray microtomography scan information

In this section we present results generated from applying the lattice Boltzmann technique to domains generated from X-ray microtomography scans (XMT) taken from a green roof growth substrate consisting primarily of crushed brick. The scans were taken on core samples of virgin material with the dimension 50 mm in diameter by 68 mm in depth. They were taken at a resolution of 30 microns per pixel and were graciously provided by Virginia Stovin and Simon De-Ville from the University of Sheffield; more details on the composition of the substrate and the scanning procedure may be found in (De-Ville et al. 2017). The technique of segmentation was applied to the raw scans to remove organic matter and convert the images to binary using the open source software ImageJ, such that only void spaces and particles remain.

3.10.2 Subdomain idenification

Due to the resolution of the original scans it was impossible to run any simulations on the full domain due to its sheer size, thus subdomains were selected from the full core. Before any such selection, an analysis of the core was undertaken to determine the average porosities within the medium for an array of candidate subdomain volumes. Unlike in the previous sections there is no common particle size by which to choose the domain thus the reliance on a macroscopic quantification to best determine the most representative subdomain. Ultimately, two such subdomains were chosen based upon the results of the porosity analysis, one that reflects the average porosity within the core sample and one that reflects a more extreme porosity value, these being $\epsilon = 0.212$ and $\epsilon = 0.328$, respectively. Figure 3.19 displays two-dimensional cuts of the chosen subdomains of the core sample. As one can see in Figure 3.19b it is possible that voids may occur within a solid particle and thus will not play any role in the infiltration process of the wetting liquid, though we point out here that as these domains are 3-dimensional this may not necessarily be the case in this image.

3.10.3 Implementation in LBM

The implementation of the XMT scans into the LBM environment is very similar to that which we have previously described, with a few noteworthy modifications. Firstly, since the resolution of the scans is 30 microns and the simulations undertaken with the monodisperse packed beds is at about 70 microns, the domain sizes must be adjusted accordingly if the same volume is to be simulated. We have therefore used a volume with 420 voxels laterally and 140 vertical voxels, representing the porous domain. An additional 140 voxels of liquid is introduced above the XMT media and the gravitational constant is modified accordingly to maintain the same

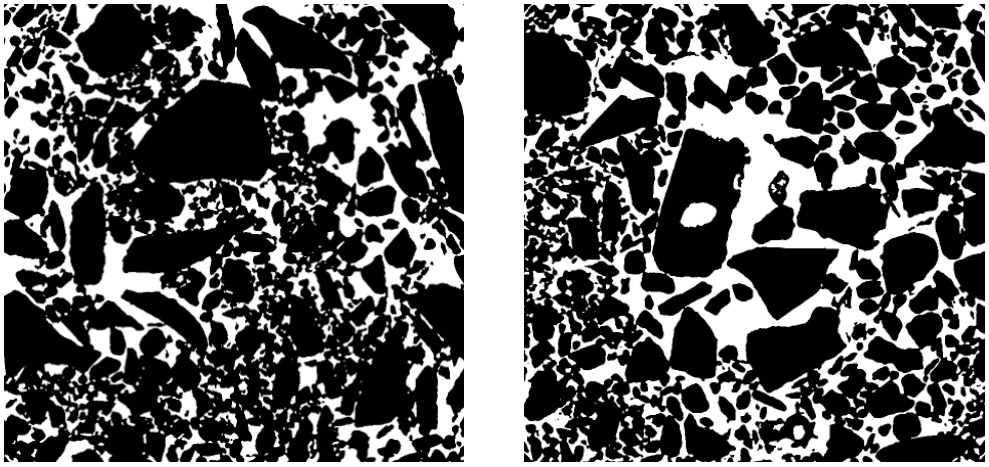

(a) (b)

Figure 3.19: 2D cuts of the XMT core center(curved walls removed), void in white, particles in black.

Bond number. The new gravitational value is $g = 8.24 \times 10^{-6}$ to match the same hydrostatic pressure applied for a liquid height of 5 mm. Another modification is the number of timesteps, reduced from 400K to 50K but with an increased resolution of results every 1K timesteps to better capture the initial infiltration effects. As a comparison the same subdomains were rerun with half of the spatial resolution, marked 'LR' in the figures, to ascertain the impact of a coarser resolution on the infiltration dynamics. This resolution was set at the same value as the packed bed simulations and was accomplished by simply reducing the matrix rank using a nearest neighbor algorithm to determine whether a cell was void or solid.

3.10.4 Saturation and interfacial area

In Figure 3.20 the evolution of saturation and interfacial area over time is plotted for each subdomain. It is immediately clear that in the case of the representative porosity subdomain the infiltration reaches an equilibrium state in a short period of time whereas the more porous subdomain continuously experiences a low rate of infiltration after a comparatively quicker initial filling state. We can see a significant difference in the initial and subsequent behavior of the lower resolution runs, which begin at a higher saturation value due to the resolution reduction. In the case of the $\epsilon = 0.328$ subdomain we also see an increased saturation in time, suggesting that the reduction in resolution has either removed particles blocking the flow or opened new pathways. The other possible cause for this difference is that the flow is no longer correctly resolved and thus we do not see the valve-like blocking effect on the flow caused by the capillary pressure, as discussed later. In the case of $\epsilon = 0.328$ we see the initial infiltration state from $t^* = 0 - 15$ correspond to drops in the interfacial area, due to the initial contact between the liquid and porous domain. Subsequent to this stage we see a steady increase in the interfacial area as the liquid penetrates the microstructure. The lack of instantaneous jumps in the interfacial area is indicative of a lack of spontaneous filling of pores through the buildup of

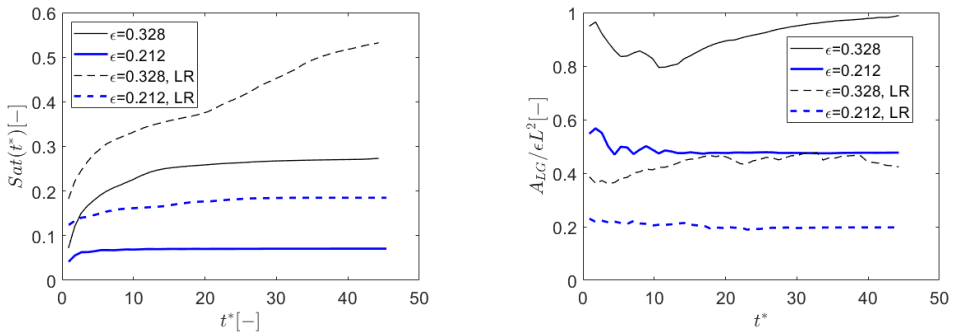

(a) (b)

Figure 3.20: (a) Saturation and (b) interfacial area as a function of nondimensional time. $\epsilon = 0.328$ and $\epsilon = 0.212$. 'LR' - Low Resolution.

pressure to overcome the surface tension but rather a creeping infiltration. The case with porosity $\epsilon = 0.212$ displays a somewhat similar infiltration curve however an equilibrium is reached very quickly whereafter the saturation and interfacial area do not very appreciably in time. In order to verify this we must examine the capillary pressure within each subdomain. Once again we see a marked difference in the lower resolution cases. We see an appreciable drop in initial surface area, from close to 100% to 40% for the more porous subdomain and from 60% to about 20% for the less porous one. This suggests strongly that there are many areas within the medium that cannot be infiltrated, representing 'dead area' wherein no infiltration is possible, thus reducing the possible maximum theoretical interfacial area. The systemic nature of this drop for both cases lends support to this explanation.

3.10.5 Capillary pressure

In Figure 3.21 the effective capillary pressure as defined by $p_{c,eff} = (p_w - p_{nw})d/\gamma$ is plotted as a function of time and saturation. It is important to note here that a negative sign denotes capillary suction and a positive sign a valve-like blocking effect on infiltration. This is due to the higher pressure found on the non-wetting side of the interface as determined by the concave nature of the meniscus as we have set the contact angle to be slightly hydrophilic. An oscillatory pattern is displayed by both cases, with that of the high porosity displaying a higher amplitude of oscillation. Once again the initial period is separable from the subsequent infiltration. In the initial stages the capillary pressure changes sign several times, with an equilibrium value slightly positive, denoting the lack of capillary suction in the later stages of the observed infiltration. This observation confirms the hypothesis concerning the gradual increase in the interfacial area without instantaneous jumps. A position of equilibrium for the effective capillary pressure is reached for both cases, at $t^* = 30$ for $\epsilon = 0.328$ and at $t^* = 15$ for $\epsilon = 0.212$. When one considers the volume averaged capillary pressure as a function of saturation it is difficult to extract any correlation. What we can say is that on the whole the pressure oscillates throughout the process of infiltration, as evidenced when one zooms in as in Figure 3.22 for the case of $\epsilon = 0.212$. The value of capillary pressure repeatedly changes sign, leading to the

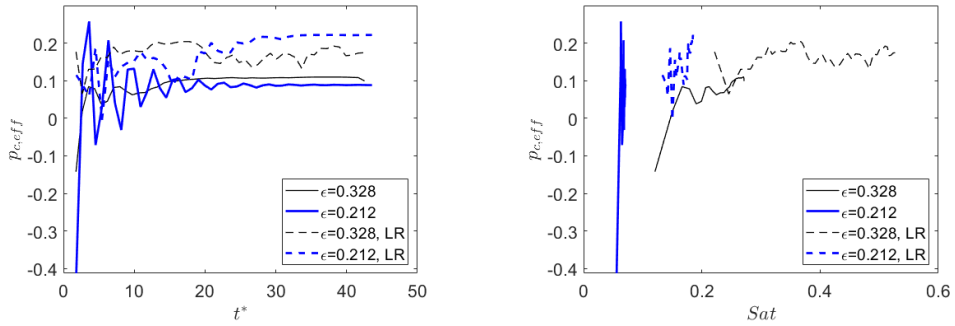

(a) (b)

Figure 3.21: Effective capillary pressure as a function of (a) time, and (b) saturation. 'LR' - Low Resolution.

postulation that capillary suction is not the primary driving force of the infiltration in this case. If one examines the lower resolution cases we find a similar pattern displayed, particularly for the less porous case, wherein the saturation is slightly higher however values for capillary pressure remain similar, though slightly higher in the lower resolution case. This is true for both porosities, with some oscillation occurring for the more porous case which is in line with the continued infiltration previously observed. Both cases with reduced resolution display higher value of positive capillary pressure, corresponding to a resistance to the infiltrating liquid. If the changes in topology are not the driving factor here then we must conclude that the flow is insufficiently resolved at this resolution, at least with regard to the overall capillary pressure with in the subdomain. We now wish to examine the localized capillary pressure for all cases, as this will give additional insight. A closer

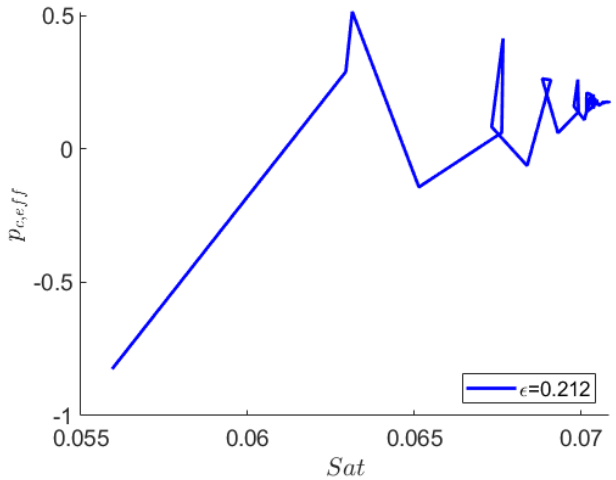

Figure 3.22: Effective capillary pressure as a function of saturation, zoom for 3.21b, $\epsilon = 0.212$

examination of the capillary pressure is necessary, thus the local capillary pressure is calculated within 6 lattice nodes to the wetting-non-wetting interface. At each

timestep the effective capillary pressure is calculated at all local interfaces within the porous volume and the mean and standard deviations are plotted in Figure 3.23.

3.10.6 Localized capillary pressure

Figure 3.23 displays the local effective capillary pressure for each porosity. It is immediately clear that when $\epsilon = 0.212$ the mean value of local capillary pressure is near zero however the standard deviations show a large heterogeneity present within the microstructure. We see the mean value shifted slightly to the positive for the more porous case which agrees with the volumetric averaging for the capillary pressure in this case. The lower porosity case displays behavior inconsistent with the notion of infiltration occurring as a consequence of capillary suction, thus we conclude that viscous forces are playing a more significant role. If this is the case then we should examine the distributions of the porosity within the representative volume as well as the pore size and particle size distributions. The distributions

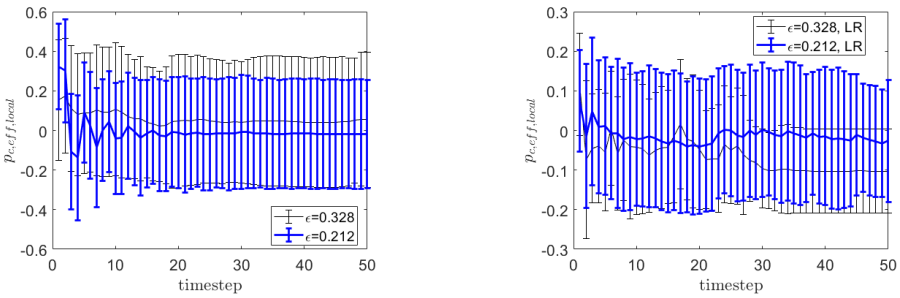

(a) (b)

Figure 3.23: Mean and standard deviation of local capillary pressure over time. (a) standard resolution (b) 'LR' - Low Resolution.

for the same quantities are plotted in Figure 3.23b but for the cases with reduced spatial resolution. The results very significantly from the higher resolution cases, with more pronounced shifts in the more porous case. The capillary pressure means are consistently negative, indicating capillary suction is contributing to the advance of the liquid front, a clear difference from the higher resolution counterpart. The case with $\epsilon = 0.212$ is more consistent with its higher resolution counterpart, wherein little to no capillary suction occurs. The observed differences must be put down to the alteration of the microstructure with the reduction in resolution. In the case of $\epsilon = 0.212$ the results appear to be consistent regardless of resolution, indicating we are indeed observing a physical phenomenon rather than an artifact of the numerics.

3.10.7 Porosity and pore size distribution

In Figure 3.24 the frequency histogram of porosities calculated for a structured distribution of subdomains within the full core is presented along with the pore size distribution for the chosen subdomains on which the infiltration simulations were run. The porosity distribution ranges from very low porosities such as 0.06

to more open solid matrices with values closer to 0.35. The mean value of 0.212 is chosen as one of our cases on the basis it represents most accurately the mean porosity within the core sample and one more extreme case is chosen to illustrate the differences in infiltration with a variation in porosity. No values lower than the mean are chosen for this study as once porosity decreases further the pore network no longer supports connections spanning the depth of the medium and only isolated pockets may experience infiltration, given the contact angle of choice in this work which is near neutral. The distribution of pore size shown in Figure

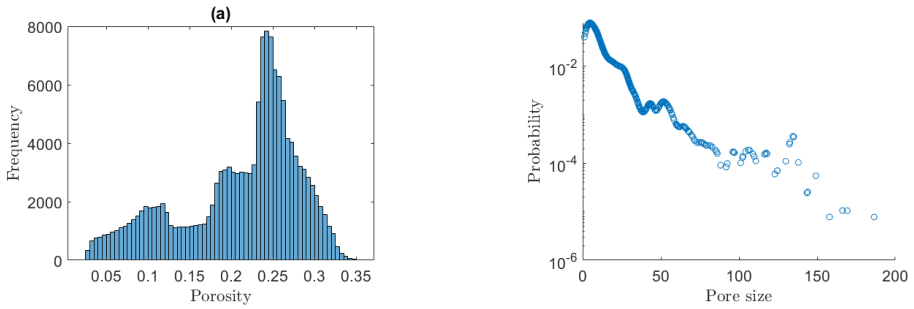

(a) (b)

Figure 3.24: (a) Porosity frequency histogram of core subdomains. (b) PDF of pore size, $\epsilon = 0.328$ and $\epsilon = 0.212$

3.24b shows a high occurrence of very small pores with a radius of about 5 lattice units or 150 microns, and pores above 15-20 lattice units (450-600 microns) are very rare indeed. This brings up the issue of spatial resolution when one considers the lack of infiltration observed, particularly in the case with porosity $\epsilon = 0.212$. It is possible that higher resolution is required to adequately capture the geometry for such small pores, wherein significant energy is required to overcome the resistive forces, particularly in the case where we have little to no capillary suction occurring.

Particle size probability distribution functions are given in Figure 3.25 for each individual subdomain. In both cases the sizes of the particles are of the same magnitude as that of the pore sizes and even more interestingly, the distributions are very similar in terms of a larger frequency of smaller particles followed by a fairly steep drop-off in larger particle occurrence. The most notable difference is the cluster of larger particles in the case of $\epsilon = 0.212$, surrounded by much smaller particles, likely tightly packed. This is in contrast to the case of $\epsilon = 0.328$ where we see a more gradual increase in particle size and smaller maxima, indicating a slightly more homogeneous distribution of particles of similar size, which lends itself to having a higher porosity overall.

3.10.8 Conclusions and Future Work

There are several points of interest to point out from the analysis of liquid infiltration in a realistic growth substrate. The most important take-away is that in the case of extremely low porosity substrates such as those presented in this work, it is likely that higher resolution images are necessary to capture the physics in the micro-pores.

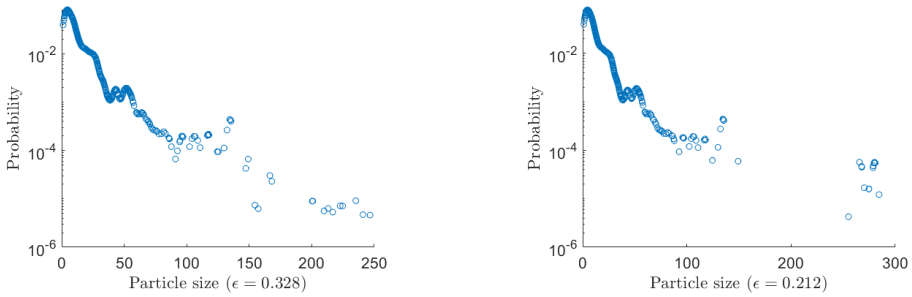

(a) (b)

Figure 3.25: Particle size PDFs for (a) $\epsilon = 0.328$ (b) $\epsilon = 0.212$

This argument is based upon the observed difficulties in the cases we have run with infiltration at such low porosities and a near-neutral contact angle. Another point of note is the magnitude equivalence between the measured pore and particle sizes, as well as their respective probability distribution curves. Considering the subdomains we examined are taken from different locations within the core sample it may be argued that if one takes a sufficiently large subdomain it may be possible to assume it to be representative of a larger sample core or growth substrate. This would most certainly require more work to verify however the current results are encouraging, at least with the material in this work.

Another consequence of this study is the differences (and lack thereof) observed in the volumetric and local effective capillary pressure. We see a consistency in the low porosity cases between the two quantities, indicating a lack of marked contribution from capillary suction. As previously mentioned, the volumetric capillary pressure includes both viscous and capillary forces; so when we see little contribution locally we can identify that the viscous forces are the dominating factor for infiltration. This ability to capture and separate these individual forces allows to more accurately identify when capillary suction plays no role in infiltration, which can be caused if the correct materials and particle sizes are chosen for such a growth substrate.

When the idealized packed bed cases are compared to the cases with realistic porous topology we are able to see similar physical phenomenon but in the case of the sample identified here, the porosity is markedly different. This leads to large divergences in infiltration rates and interfacial areas. Whereas the idealized cases displayed some rate of infiltration even without capillary suction, in the realistic cases we do not see this. The answer may lie in the interfacial area, as we see frequent oscillations in the idealized cases which here again are not observed in the realistic domain simulations. This would suggest that while in the idealized cases there is sufficient energy to overcome the surface tension forces this does not exist in the realistic cases. This would seem counter-intuitive since greater energy is required to invade rapidly expanding pores, thus we argue that the pore expansions in the realistic domains expand rapidly enough as to prevent any infiltration. This can be due to the irregular topology and the presence of larger particles interspersed with much smaller ones, leading to more extreme pore throats and connections that those present in the idealized cases with regular particle topology.

These observations motivate my recommendations for future investigation of this aspect of infiltration of realistic substrates. I believe attention should be paid to increase the spatial resolution of XMT scanned images to ensure the flow is correctly captured. The applicability of a subdomain as a representative volume needs to be investigated, as it is expensive to resolve full-scale substrates using LBM. If it is found not be possible to predict some dynamics from a subdomain then perhaps another approach must be considered. The most obvious expansion of this work is to remove the single contact angle restriction and allow for heterogeneous material makeup but this must be carefully considered as once complexity is added to the microstructure it may be more difficult to isolate the more fundamental physical phenomenon determining the infiltration dynamics. In short, the goal of further work should be to attempt to approach a more realistic substrate in terms of material composition and size/representativity for larger scale green roofs.

Chapter 4

Summary and conclusions

In this work two main objectives concerning the mitigation of storm water runoff in urban environments were investigated: i) optimization of a green roof by placement and ii) optimization of a green roof growth substrate by design. These goals were investigated through the use of CFD modeling techniques to both ascertain their applicability as well as determine the accuracy and possibility of their use as predictive tools in lieu of excessive trial-and-error approaches. In this regard my final thoughts are organized here by topic for ease of the reader.

4.1 Optimization of green roof placement

The work consisted of applying a RANS model with turbulent closure models for each rainfall phase in addition to the wind phase to solve the motion of wind-driven rainfall against building facades. The motion of the rain phases were tracked in the vicinity of the buildings and the quantity of rainfall incident on the building facades was calculated. Two validation cases were undertaken and a full scale application was attempted. The results consisted of highly variable accuracy for the validation cases and insurmountable difficulties with regard to the full scale case.

If one considers the computational resources required to solve the Eulerian multiphase system for wind and multiple rain phases the results are not encouraging if compared to alternative approaches. The aim of including the full turbulent model closures was to improve accuracy by capturing turbulent dispersion near the building facade where most irregular motion will occur and wind velocities are locally the highest. This was not the obtained result, though this can be due to a variety of factors. My opinion on the matter is that there are too many possibilities when determining number of phases to use, the best method of initializing turbulent conditions for both rain and wind phases, how to best locally determine the velocities at the facade, and which turbulent model is best suited for the whole investigation. The addition of more phases reduces each phase's volumetric ratio, and this reduction can cause numerical instabilities since the phasic ratios are already rarified. The local velocities are averaged *near* the facade boundary over a chosen subarea however no studies undertaken (that this author is aware of) have quantified the effect of altering the averaging area or at what distance the measurement is best taken. The closer to

the boundary one gets the velocities will drop to zero within the viscous boundary layer, thus nullifying any measurement significance. The largest issue I have come across is the choice of initial condition and boundary initilization for the turbulent quantities for the rainfall phases. The fields were initialized with minimal turbulent kinetic energy as the wind phase is expected to transfer its energy to the rainfall phases however I encountered many divergences at this stage. Subsequently several different strategies were used and none were found to truly satisfactorily prevent divergences. At smaller scales as with those of the validation cases it was possible to prevent such issues however at the larger scale this issue was never resolved. My thought is that much more investigation needs to be done on this particular aspect of the simulations before advances can be made in accuracy, and this ties in to the choice of turbulence model as well, also possibly improving accuracy.

4.2 Optimization of green roof growth substrate by design

This work consisted of the application of the LBM technique to idealized growth substrates comprising of monodisperse spherical particles in a random packing. Liquid was initialized as surface water above the packed bed and gravitational forces drive the infiltration of the liquid through the porous microstructure. Several parameters including saturation, interfacial area, capillary pressure, wetting front homogeneity, and pore size distribution are used to quantify the performance of different packed beds, each with its own particle size and packing ratio. By looking at cases with a near-neutral contact angle I have identified cases wherein the capillary forces act against the flow gradient and effectively retard the infiltration of the liquid. This phenomenon has been verified and explained by physical and mathematical formulations. The effect of the microstructure on this phenomenon has been quantified and the results applied to the design of green roof growth substrates. Effectively I have produced some design guidelines concerning hydrostatic pressure and packing parameters that can be used to produce differing effectivity of thin green roof growth substrates.

I find this work at the microstructural level very important as we need not rely on curve fitting or empirical relations to determine the infiltration dynamics. We are also able to identify individual factors contributing to the differing behaviors and can test directly their interdependence. This direct method can be used to determine the effects of packing, heterogeneous particle properties such as contact angle or geometry on flows with relative ease; and can possibly be used to substitute or complement experimental studies to gain more insight into unsaturated flow hysteresis. The ultimate goal should be to predict full saturation-interfacial area-water content curves without the need for measurements under some assumptions. In this regard, examining the impact of dynamic properties such as dynamic capillary pressure as the velocities with the porous microstructure are non-zero might aid in this endeavor. Solving these problems under static conditions can only give a partial picture and though it may be enough to provide adequate results at the macroscopic scale it has not succeeded to fully capture the complex physics involved, hence the

hysteresis we must contend with. I believe further examination of the processes using transient measurements should be undertaken to determine methods for measuring these interdependencies in real time. Additionally, more comparison with real green roof microstructures are needed to elucidate over what scope and scale these findings can be applied, do they hold to the applications themselves and if so over what period of time? Finally, with the inclusion of organic matter the models will need to capture vegetation, such a roots and soil displacement as well as climatic differences which may influence the microstructure itself such as ice formation. In short, there are many possible routes of future work that need to be explored to fully bring this methodology to its potential for use in solving the optimization problem but promise has been shown if we can examine the problem this way.

Bibliography

Abidoye, L. K. and D. B. Das (2015). "Artificial neural network modeling of scale-dependent dynamic capillary pressure effects in two-phase flow in porous media". In: *Journal of Hydroinformatics* 17.3, pp. 446–461. ISSN: 14647141. DOI: 10.2166/hydro.2014.079 (cit. on p. 41).

Abuku, M., B. Blocken, K. Nore, J. V. Thue, J. Carmeliet, and S. Roels (2009). "On the validity of numerical wind-driven rain simulation on a rectangular low-rise building under various oblique winds". In: *Building and Environment* 44, pp. 621–632. DOI: 10.1016/j.buildenv.2008.05.003 (cit. on p. 12).

Aggelopoulos, C. A. and C. D. Tsakiroglou (2008). "The effect of micro-heterogeneity and capillary number on capillary pressure and relative permeability curves of soils". In: *Geoderma* 148.1, pp. 25–34. ISSN: 00167061. DOI: 10.1016/j.geoderma.2008.08.011 (cit. on p. 37).

Arisz, H. and B. Burrell (2006). "Urban drainage infrastructure planning and design considering climate change". In: DOI: 10.1109/EICCCC.2006.277251 (cit. on p. 5).

Bajare, D., A. Korjakins, J. Kazjonovs, and I. Rozenstrauha (2012). "Pore structure of lightweight clay aggregate incorporate with non-metallic products coming from aluminium scrap recycling industry". In: *Journal of the European Ceramic Society* 32.1, pp. 141–148. DOI: 10.1016/j.jeurceramsoc.2011.07.039 (cit. on p. 51).

Beard, K. (1976). "TERMINAL VELOCITY AND SHAPE OF CLOUD AND PRECIPITATION DROPS ALOFT." In: *Journal of the Atmospheric Sciences* 33.5, pp. 851–864. DOI: 10.1175/1520-0469(1976)033<0851:TVASOC>2.0.CO;2 (cit. on p. 23).

Beavers, G. and D. Joseph (1967). "Boundary conditions at a naturally permeable wall". In: *Journal of Fluid Mechanics* 30.1, pp. 197–207. DOI: 10.1017/S0022112067001375 (cit. on p. 37).

Belleudy, C., M. Woloszyn, M. Chhay, and M. Cosnier (Apr. 2016). "A 2D model for coupled heat, air, and moisture transfer through porous media in contact with air channels". In: *International Journal of Heat and Mass Transfer* 95, pp. 453–465 (cit. on p. 36).

Benzi, R., L. Biferale, M. Sbragaglia, S. Succi, and F. Toschi (2006). "Mesoscopic modeling of a two-phase flow in the presence of boundaries: The contact angle". In: *Physical Review E - Statistical, Nonlinear, and Soft Matter Physics* 74.2. DOI: 10.1103/PhysRevE.74.021509 (cit. on p. 50).

Best, A. C. (1950). "Size distribution of raindrops". In: *Quarterly J. Royal Meteorol. Soc.* 76, pp. 16–36 (cit. on pp. 12, 22).

Bhatla, R., S. Verma, R. Pandey, and A. Tripathi (2019). "Evolution of extreme rainfall events over Indo-Gangetic plain in changing climate during 1901–2010". In: *Journal of Earth System Science* 128.5. DOI: 10.1007/s12040-019-1162-1 (cit. on p. 5).

Blocken, B. and J. Carmeliet (May 2008). "Guidelines for the required time resolution of meteorological input data for wind-driven rain calculations on buildings". In: *Journal of Wind Engineering and Industrial Aerodynamics* 96.5, pp. 621–639. DOI: 10.1016/j.jweia.2008.02.008 (cit. on p. 12).

Blocken, B., G. Dezsö, J. van Beeck, and J. Carmeliet (Aug. 2009). "The mutual influence of two buildings on their wind-driven rain exposure and comments on the obstruction factor". In: *Journal of Wind Engineering and Industrial Aerodynamics* 97.5-6, pp. 180–196. DOI: 10.1016/j.jweia.2009.06.003 (cit. on p. 12).

Blocken, B. and J. Carmeliet (2002). "Spatial and temporal distribution of driving rain on a low-rise building". In: *Wind and Structures, An International Journal* 5.5, pp. 441–462 (cit. on p. 12).

Blocken, B. and J. Carmeliet (Feb. 2006). "The influence of the wind-blocking effect by a building on its wind-driven rain exposure". In: *Journal of Wind Engineering and Industrial Aerodynamics* 94.2, pp. 101–127. DOI: 10.1016/j.jweia.2005.11.001 (cit. on p. 12).

Blocken, B. and J. Carmeliet (July 2007). "Validation of CFD simulations of wind-driven rain on a low-rise building facade". In: *Building and Environment* 42.7, pp. 2530–2548. DOI: 10.1016/j.buildenv.2006.07.032 (cit. on p. 12).

Boccardo, G., F. Augier, Y. Haroun, D. Ferré, and D. Marchisio (2015). "Validation of a novel open-source work-flow for the simulation of packed-bed reactors". In: *Chemical Engineering Journal* 279, pp. 809–820–820. DOI: 10.1016/j.cej.2015.05.032 (cit. on p. 51).

Brooks, R. H. and A. Corey (1964). *Hydraulic properties of porous media*. Hydrology papers 3. Fort Collins, Colorado: Colorado State University (cit. on pp. 38, 43).

Camps-Roach, G., D. M. O'Carroll, T. A. Newson, T. Sakaki, and T. H. Illangasekare (2010). "Experimental investigation of dynamic effects in capillary pressure: Grain size dependency and upscaling". In: *Water Resources Research* 46.8. ISSN: 00431397. DOI: 10.1029/2009WR008881 (cit. on p. 41).

Carmeliet, J., F. Descamps, and G. Houvenaghel (1999). "A multiscale network model for simulating moisture transfer properties of porous media". In: 35.1, pp. 67–88. DOI: 10.1023/A:1006500716417 (cit. on p. 40).

Carmeliet, J. and S. Roels (2001). "Determination of the isothermal moisture transport properties of porous building materials". In: 24.3, pp. 183–210. DOI: 10.1106/Y6T2-9LLP-04Y5-AN6T (cit. on p. 40).

Cascone, S., J. Coma, A. Gagliano, and G. Pérez (2019). "The evapotranspiration process in green roofs: A review". In: *Building and Environment* 147, pp. 337–355. ISSN: 0360-1323. DOI: https://doi.org/10.1016/j.buildenv.2018.10.024 (cit. on p. 44).

Cassie, A. B. D. and S. Baxter (1944). "Wettability of porous surfaces". In: *Trans. Faraday Soc.* 40 (0), pp. 546–551. DOI: 10.1039/TF9444000546 (cit. on p. 62).

Charpentier, S. (June 2009). *Simulation of heat exchange phenomena and water regime in green roof substrates. Proceedings of the International Symposium on Growing Media and Composting*. Charlotte, USA: International Society Horticultural Science (cit. on p. 36).

Chen, L., Q. Kang, Y. Mu, Y.-L. He, and W.-Q. Tao (2014). "A critical review of the pseudopotential multiphase lattice Boltzmann model: Methods and applications". In: *International Journal of Heat and Mass Transfer* 76, pp. 210–236. DOI: 10.1016/j.ijheatmasstransfer.2014.04.032 (cit. on p. 49).

Choi, E. (1994). "Determination of wind-driven-rain intensity on building faces". In: *Journal of Wind Engineering and Industrial Aerodynamics* 51, pp. 55–69. DOI: 10.1016/0167-6105(94)90077-9 (cit. on p. 11).

Connelly, M. and M. Hodgson (2013). "Experimental investigation of the sound transmission of vegetated roofs". In: *Applied Acoustics* 74.10, pp. 1136–1143. ISSN: 0003-682X. DOI: https://doi.org/10.1016/j.apacoust.2013.04.003 (cit. on p. 4).

Cueto-Felgueroso, L. and R. Juanes (2008). "Nonlocal interface dynamics and pattern formation in gravity-driven unsaturated flow through porous media". In: 101.24. DOI: 10.1103/PhysRevLett.101.244504 (cit. on pp. 39, 70).

Dahle, H. K., M. A. Celia, and S. M. Hassanizadeh (2005). "Bundle-of-tubes model for calculating dynamic effects in the capillary-pressure-saturation relationship". In: *Transport in Porous Media* 58.1-2, pp. 5–22. ISSN: 01693913. DOI: 10.1007/s11242-004-5466-4 (cit. on p. 41).

De Maio, A., S. Palpacelli, and S. Succi (2011). "A New Boundary Condition for Three-Dimensional Lattice Boltzmann Simulations of Capillary Filling in Rough Micro-Channels". In: *Communications in Computational Physics* 9.5, pp. 1284–1292. DOI: 10.4208/cicp.141009.241110s (cit. on p. 50).

Defraeye, T., B. Blocken, and J. Carmeliet (Sept. 2011). "Analysis of convective heat and mass transfer coefficients for convective drying of a porous flat plate by conjugate modelling". In: *International Journal of Heat and Mass Transfer* 55.1, pp. 112–124. DOI: 10.1016/j.ijheatmasstransfer.2011.08.047 (cit. on p. 36).

Fér, M., M. Leue, R. Kodešová, H. Gerke, and R. Ellerbrock (2016). "Droplet infiltration dynamics and soil wettability related to soil organic matter of soil aggregate coatings and interiors". In: *Journal of Hydrology and Hydromechanics* 64.2, pp. 111–120. DOI: 10.1515/johh-2016-0021 (cit. on p. 55).

Ferrari, A., J. Jimenez-Martinez, T. Borgne, Y. Méheust, and I. Lunati (2015). "Challenges in modeling unstable two-phase flow experiments in porous micromodels". In: *Water Resources Research* 51.3, pp. 1381–1400. DOI: 10.1002/2014WR016384 (cit. on p. 36).

Ferrari, A. and I. Lunati (2013). "Direct numerical simulations of interface dynamics to link capillary pressure and total surface energy". In: *Advances in Water Resources* 57, pp. 19–31. ISSN: 03091708. DOI: 10.1016/j.advwatres.2013.03.005 (cit. on p. 41).

Fučík, R. and J. Mikyška (2011). "Numerical investigation of dynamic capillary pressure in two-phase flow in porous medium". In: *Mathematica Bohemica* 136.4, pp. 395–403. ISSN: 08627959. DOI: 10.21136/mb.2011.141699 (cit. on p. 41).

Fučík, R., J. Mikyška, T. Sakaki, M. Beneš, and T. H. Illangasekare (2010). "Significance of Dynamic Effect in Capillarity during Drainage Experiments in Layered Porous Media". In: *Vadose Zone Journal* 9.3, pp. 697–708. ISSN: 1539-1663. DOI: 10.2136/vzj2009.0106 (cit. on p. 41).

Galindo-Torres, S., A. Scheuermann, and L. Li (2016). "Boundary effects on the Soil Water Characteristic Curves obtained from lattice Boltzmann simulations". In: *Computers and Geotechnics* 71, pp. 136–146. DOI: 10.1016/j.compgeo.2015.09.008 (cit. on pp. 51, 52, 54).

Gallage, C., J. Kodikara, and T. Uchimura (2013). "Laboratory measurement of hydraulic conductivity functions of two unsaturated sandy soils during drying and wetting processes". In: *Soils and Foundations* 53.3, pp. 417–430. DOI: 10.1016/j.sandf.2013.04.004 (cit. on p. 38).

Genuchten, M. van (1980). "CLOSED-FORM EQUATION FOR PREDICTING THE HYDRAULIC CONDUCTIVITY OF UNSATURATED SOILS." In: *Soil Science Society of America Journal* 44.5, pp. 892–898. DOI: 10.2136/sssaj1980.03615995004400050002x (cit. on pp. 38, 43).

Gladkikh, M. and S. L. Bryant (2006). "Influence of wettability on petrophysical properties during imbibition in a random dense packing of equal spheres". In: *Journal of Petroleum Science and Engineering* 52.1-4, pp. 19–34. ISSN: 09204105. DOI: 10.1016/j.petrol.2006.03.004 (cit. on p. 41).

Glover, P. and E. Walker (2009). "Grain-size to effective pore-size transformation derived from electrokinetic theory". In: *Geophysics* 74.1. DOI: 10.1190/1.3033217 (cit. on p. 51).

Glover, P., I. Zadjali, and K. Frew (2006). "Permeability prediction from MICP and NMR data using an electrokinetic approach". In: *Geophysics* 71.4. DOI: 10.1190/1.2216930 (cit. on p. 51).

Goel, G., L. K. Abidoye, B. R. Chahar, and D. B. Das (2016). "Scale dependency of dynamic relative permeability–satuartion curves in relation with fluid viscosity and dynamic capillary pressure effect". In: *Environmental Fluid Mechanics* 16.5, pp. 945–963. ISSN: 15731510. DOI: 10.1007/s10652-016-9459-y (cit. on p. 37).

Goel, G. and D. M. O'Carroll (2011). "Experimental investigation of nonequilibrium capillarity effects: Fluid viscosity effects". In: *Water Resources Research* 47.9. ISSN: 00431397. DOI: 10.1029/2010WR009861 (cit. on p. 37).

Gostick, J. et al. (2016). "OpenPNM: A Pore Network Modeling Package". In: 18.4, pp. 60–74. DOI: 10.1109/MCSE.2016.49 (cit. on p. 40).

Gray, W. G., A. L. Dye, J. E. McClure, L. J. Pyrak-Nolte, and C. T. Miller (2015). "On the dynamics and kinematics of two-fluid-phase flow in porous media". In: *Water Resources Research* 51.7, pp. 5365–5381. ISSN: 19447973. DOI: 10.1002/2015WR016921 (cit. on p. 41).

Gregersen, I., H. Sørup, H. Madsen, D. Rosbjerg, P. Mikkelsen, and K. Arnbjerg-Nielsen (2013). "Assessing future climatic changes of rainfall extremes at small

spatio-temporal scales". In: *Climatic Change* 118.3-4, pp. 783–797. DOI: 10.1007/s10584-012-0669-0 (cit. on p. 6).

Gunn, R. and G. D. Kinzer (1949). *The Terminal Velocity of Fall for Water Droplets in Stagnant Air*. DOI: 10.1175/1520-0469(1949)006<0243:TTVOFF>2.0.CO;2 (cit. on pp. 12, 22).

Guo, Z., C. Zheng, and B. Shi (Apr. 2002). "Discrete lattice effects on the forcing term in the lattice Boltzmann method". In: *Phys. Rev. E* 65 (4). DOI: 10.1103/PhysRevE.65.046308 (cit. on p. 49).

Haeupl, P. and Y. Xu (2001). "Numerical simulation of freezing and melting in porous materials under the consideration of the coupled heat and moisture transport". In: 25.1, pp. 4–31. DOI: 10.1106/RX1L-MBE8-HUJ3-2XX3 (cit. on p. 37).

Hagentoft, C.-E. et al. (2004). "Assessment Method of Numerical Prediction Models for Combined Heat, Air and Moisture Transfer in Building Components: Benchmarks for One-dimensional Cases". In: 27.4, pp. 327–352. DOI: 10.1177/1097196304042436 (cit. on p. 36).

Haines, W. B. (1930). "Studies in the physical properties of soil. V. The hysteresis effect in capillary properties, and the modes of moisture distribution associated therewith". In: *The Journal of Agricultural Science* 20.1, pp. 97–116. DOI: 10.1017/S002185960008864X (cit. on p. 62).

Hanspal, N. S. and D. B. Das (2012). "Dynamic effects on capillary pressure-Saturation relationships for two-phase porous flow: Implications of temperature". In: *AIChE Journal* 58.6, pp. 1951–1965. ISSN: 00011541. DOI: 10.1002/aic.12702 (cit. on p. 37).

Hibi, Y., A. Tomigashi, and M. Hirose (Dec. 2015). "Evaluation of a numerical simulation model for a system coupling atmospheric gas, surface water and unsaturated or saturated porous medium". In: *Journal of Contaminant Hydrology* 183, pp. 121–134 (cit. on p. 36).

Higuera, F. and J. Jiménez (1989). "Boltzmann approach to lattice gas simulations". In: *EPL* 9.7, pp. 663–668. DOI: 10.1209/0295-5075/9/7/009 (cit. on p. 48).

Hilpert, M. (2012). "Velocity-dependent capillary pressure in theory for variably-saturated liquid infiltration into porous media". In: 39.6. DOI: 10.1029/2012GL051114 (cit. on p. 39).

Hsu, S. Y., V. Huang, S. Woo Park, and M. Hilpert (2017). "Water infiltration into prewetted porous media: Dynamic capillary pressure and Green-Ampt modeling". In: *Advances in Water Resources* 106, pp. 60–67. ISSN: 03091708. DOI: 10.1016/j.advwatres.2017.02.017 (cit. on p. 41).

Huang, H., M. Krafczyk, and X. Lu (2011). "Forcing term in single-phase and Shan-Chen-type multiphase lattice Boltzmann models". In: *Physical Review E - Statistical, Nonlinear, and Soft Matter Physics* 84.4. DOI: 10.1103/PhysRevE.84.046710 (cit. on p. 49).

Huang, S. and Q. Li (Dec. 2010). "Numerical simulations of wind-driven rain on building envelopes based on Eulerian multiphase model". In: *Journal of Wind Engineering and Industrial Aerodynamics* 98.12, pp. 843–857. DOI: 10.1016/j.jweia.2010.08.003 (cit. on p. 13).

Huong, H. and A. Pathirana (2013). "Urbanization and climate change impacts on future urban flooding in Can Tho city, Vietnam". In: *Hydrology and Earth System Sciences* 17.1, pp. 379–394. DOI: 10.5194/hess-17-379-2013 (cit. on p. 6).

Jäger, W. and A. Mikelić (2000). "On the interface boundary condition of Beavers, Joseph, and Saffman". In: *SIAM Journal on Applied Mathematics* 60.4, pp. 1111–1127. DOI: 10.1137/s003613999833678x (cit. on p. 37).

Jahanbakhshi, S., M. H. Ghazanfari, and M. Masihi (2013). "Non-equilibrium model of three-phase flow in porous media in presence of capillary and gravity forces". In: *Journal of Hydrology* 478, pp. 119–131. ISSN: 00221694. DOI: 10.1016/j.jhydrol.2012.11.051 (cit. on p. 37).

Janssen, H. (2014). "Simulation efficiency and accuracy of different moisture transfer potentials". In: 7.5, pp. 379–389. DOI: 10.1080/19401493.2013.852246 (cit. on p. 36).

Joekar-Niasar, V. and S. M. Hassanizadeh (2011). "Effect of fluids properties on non-equilibrium capillarity effects: Dynamic pore-network modeling". In: *International Journal of Multiphase Flow* 37.2, pp. 198–214. ISSN: 03019322. DOI: 10.1016/j.ijmultiphaseflow.2010.09.007 (cit. on pp. 40, 41).

Joekar-Niasar, V. and S. M. Hassanizadeh (2012). "Analysis of fundamentals of two-phase flow in porous media using dynamic pore-network models: A review". In: *Critical Reviews in Environmental Science and Technology* 42.18, pp. 1895–1976. ISSN: 10643389. DOI: 10.1080/10643389.2011.574101 (cit. on pp. 40, 41).

Joekar-Niasar, V., S. M. Hassanizadeh, and H. K. Dahle (2010). "Non-equilibrium effects in capillarity and interfacial area in two-phase flow: Dynamic pore-network modelling". In: *Journal of Fluid Mechanics* 655, pp. 38–71. ISSN: 00221120. DOI: 10.1017/S0022112010000704 (cit. on p. 40).

Johannessen, B., T. Muthanna, and B. Braskerud (2018). "Detention and retention behavior of four extensive green roofs in three nordic climate zones". In: *Water* 10.6, p. 671 (cit. on p. 44).

Johnson, P. J., G. A. Zyvoloski, and P. H. Stauffer (2019). "Impact of a Porosity-Dependent Retention Function on Simulations of Porous Flow". In: *Transport in Porous Media* 127.1, pp. 211–232. ISSN: 15731634. DOI: 10.1007/s11242-018-1188-x (cit. on p. 37).

Juanes, R. (2008). "Nonequilibrium effects in models of three-phase flow in porous media". In: *Advances in Water Resources* 31.4, pp. 661–673. ISSN: 03091708. DOI: 10.1016/j.advwatres.2007.12.005 (cit. on p. 37).

Karczmarczyk, A., A. Bus, and A. Baryla (2018). "Phosphate leaching from green roof substrates-Can green roofs pollute urban water bodies?" In: *Water (Switzerland)* 10.2. DOI: 10.3390/w10020199 (cit. on p. 5).

Kim, H., D. Gu, and H. Kim (2018). "Effects of Urban Heat Island mitigation in various climate zones in the United States". In: *Sustainable Cities and Society* 41, pp. 841–852. DOI: 10.1016/j.scs.2018.06.021 (cit. on p. 5).

Koniorczyk, M. and D. Gawin (2006). "Numerical modelling of coupled heat, moisture and salt transport in porous materials". In: *Computer Assisted Mechanics and Engineering Sciences*. Vol. 13. 4, pp. 565–574 (cit. on p. 37).

Kubilay, A., D. Derome, B. Blocken, and J. Carmeliet (Mar. 2013). "CFD simulation and validation of wind-driven rain on a building facade with an Eulerian multiphase model". In: *Building and Environment* 61, pp. 69–81. DOI: 10.1016/j.buildenv.2012.12.005 (cit. on p. 13).

Kubilay, A., D. Derome, B. Blocken, and J. Carmeliet (Aug. 2014a). "High-resolution field measurements of wind-driven rain on an array of low-rise cubic buildings". In: *Building and Environment* 78, pp. 1–13. DOI: 10.1016/j.buildenv.2014.04.004 (cit. on pp. 13, 21, 25).

Kubilay, A., D. Derome, B. Blocken, and J. Carmeliet (June 2014b). "Numerical modeling of turbulent dispersion for wind-driven rain on building facades". In: *Environmental Fluid Mechanics* 15.1, pp. 109–133. DOI: 10.1007/s10652-014-9363-2 (cit. on p. 13).

Kubilay, A., D. Derome, B. Blocken, and J. Carmeliet (Nov. 2014c). "Numerical simulations of wind-driven rain on an array of low-rise cubic buildings and validation by field measurements". In: *Building and Environment* 81, pp. 283–295. DOI: 10.1016/j.buildenv.2014.07.008 (cit. on p. 13).

Launder, B. and D. Spalding (Mar. 1974). "The numerical computation of turbulent flows". In: *Computer Methods in Applied Mechanics and Engineering* 3.2, pp. 269–289. DOI: 10.1016/0045-7825(74)90029-2 (cit. on pp. 15, 16).

Li, J., S. R. McDougall, and K. S. Sorbie (2017). "Dynamic pore-scale network model (PNM) of water imbibition in porous media". In: *Advances in Water Resources* 107, pp. 191–211. ISSN: 03091708. DOI: 10.1016/j.advwatres.2017.06.017 (cit. on p. 41).

Li, K. and R. Horne (2006). "Comparison of methods to calculate relative permeability from capillary pressure in consolidated water-wet porous media". In: *Water Resources Research* 42.6. DOI: 10.1029/2005WR004482 (cit. on p. 38).

Li, Q., J. Rao, and P. Fazio (May 2009). "Development of HAM tool for building envelope analysis". In: *Building and Environment* 44.5, pp. 1065–1073. DOI: 10.1016/j.buildenv.2008.07.017 (cit. on p. 35).

Li, X., S. Chen, Q. Xu, and Y. Xu (2017). "Modeling the three-dimensional unsaturated water transport in concrete at the mesoscale". In: *Computers and Structures* 190, pp. 61–74. ISSN: 00457949. DOI: 10.1016/j.compstruc.2017.05.005 (cit. on pp. 40, 41).

Li, Y. and R. W. Babcock Jr. (2015). "Modeling hydrologic performance of a green roof system with HYDRUS-2D". In: *Journal of Environmental Engineering* 141.11, pp. 1–9. DOI: 10.1061/(ASCE)EE.1943-7870.0000976 (cit. on p. 36).

Li, Y., C. Liu, H. Li, S. Chen, and S. Huang (2020). "A comprehensive modelling investigation of dynamic capillary effect during non-equilibrium flow in tight porous media". In: *Journal of Hydrology* 584. ISSN: 00221694. DOI: 10.1016/j.jhydrol.2020.124709 (cit. on p. 41).

Li, Z., S. Galindo-Torres, G. Yan, A. Scheuermann, and L. Li (2018). "A lattice Boltzmann investigation of steady-state fluid distribution, capillary pressure and relative permeability of a porous medium: Effects of fluid and geometrical properties". In: *Advances in Water Resources* 116, pp. 153–166. DOI: 10.1016/j.advwatres.2018.04.009 (cit. on p. 39).

Liu, W., Q. Feng, W. Chen, W. Wei, and R. Deo (2019). "The influence of structural factors on stormwater runoff retention of extensive green roofs: new evidence from scale-based models and real experiments". In: *Journal of Hydrology* 569, pp. 230–238. DOI: 10.1016/j.jhydrol.2018.11.066 (cit. on p. 44).

Liu, Z., A. Herring, C. Arns, S. Berg, and R. Armstrong (2017a). "Pore-Scale Characterization of Two-Phase Flow Using Integral Geometry". In: *Transport in Porous Media* 118.1, pp. 99–117. DOI: 10.1007/s11242-017-0849-5 (cit. on p. 39).

Liu, Z., A. Herring, C. Arns, S. Berg, and R. Armstrong (2017b). "Pore-Scale Characterization of Two-Phase Flow Using Integral Geometry". In: *Transport in Porous Media* 118.1, pp. 99–117. DOI: 10.1007/s11242-017-0849-5 (cit. on p. 60).

Løvoll, G., M. Jankov, K. Måløy, R. Toussaint, J. Schmittbuhl, G. Schäfer, and Y. Méheust (2011). "Influence of Viscous Fingering on Dynamic Saturation-Pressure Curves in Porous Media". In: 86.1, pp. 305–324. DOI: 10.1007/s11242-010-9622-8 (cit. on pp. 39, 69).

Lunain, D., D. Ecotiere, and B. Gauvreau (2016). "In-situ evaluation of the acoustic efficiency of a green wall in urban area". In: *Proceedings of the INTER-NOISE 2016 - 45th International Congress and Exposition on Noise Control Engineering: Towards a Quieter Future*, pp. 6592–6601 (cit. on p. 4).

Lunati, I. and D. Or (2009). "Gravity-driven slug motion in capillary tubes". In: *Physics of Fluids* 21.5. ISSN: 10706631. DOI: 10.1063/1.3125262 (cit. on p. 41).

Maggiolo, D. (2017a). *A Lattice-Boltzmann open-source code project by Dario Maggiolo*. URL: https://gitlab.com/dariom/lbdm.git (cit. on p. 50).

Maggiolo, D. (2017b). "Numerical modeling and fluid-dynamic optimisation of fuel cells and flow batteries systems". Doctoral Thesis. Università degli Studi di Padov (cit. on p. 45).

Manthey, S., S. M. Hassanizadeh, R. Helmig, and R. Hilfer (2008). "Dimensional analysis of two-phase flow including a rate-dependent capillary pressure-saturation relationship". In: *Advances in Water Resources* 31.9, pp. 1137–1150. ISSN: 03091708. DOI: 10.1016/j.advwatres.2008.01.021 (cit. on p. 37).

Manthey, S., S. M. Hassanizadeh, and R. Helmig (2005). "Macro-scale dynamic effects in homogeneous and heterogeneous porous media". In: *Transport in Porous Media* 58.1-2, pp. 121–145. ISSN: 01693913. DOI: 10.1007/s11242-004-5472-6 (cit. on p. 37).

Masseroni, D. and A. Cislaghi (2016). "Green roof benefits for reducing flood risk at the catchment scale". In: *Environmental Earth Sciences* 75.7. DOI: 10.1007/s12665-016-5377-z (cit. on p. 5).

McNamara, G. and G. Zanetti (1988). "Use of the boltzmann equation to simulate lattice-gas automata". In: *Physical Review Letters* 61.20, pp. 2332–2335. DOI: 10.1103/PhysRevLett.61.2332 (cit. on p. 48).

Mikelić, A. and L. Paoli (1997). "On the derivation of the Buckley-Leverett model from the two fluid Navier-Stokes equations in a thin domain". In: *Computational Geosciences* 1.1, pp. 59–83 (cit. on p. 37).

Mikelić, A. (2003). "On an averaged model for the 2-fluid immiscible flow with surface tension in a thin cylindrical tube". In: *Computational Geosciences* 7.3, pp. 183–196. ISSN: 14200597. DOI: 10.1023/A:1025527716078 (cit. on p. 37).

Mobilia, M., A. Longobardi, and J. Sartor (2017). "Including a-priori assessment of actual evapotranspiration for green roof daily scale hydrological modelling". In: *Water (Switzerland)* 9.2. DOI: 10.3390/w9020072 (cit. on p. 44).

Nieber, J. L., R. Z. Dautov, A. G. Egorov, and A. Y. Sheshukov (2005). "Dynamic capillary pressure mechanism for instability in gravity-driven flows; review and extension to very dry conditions". In: *Transport in Porous Media* 58.1-2, pp. 147–172. ISSN: 01693913. DOI: 10.1007/s11242-004-5473-5 (cit. on p. 37).

Nijp, J., K. Metselaar, J. Limpens, H. Gooren, and S. van der Zee (2017). "A modification of the constant-head permeameter to measure saturated hydraulic conductivity of highly permeable media". In: *MethodsX* 4, pp. 134–142. DOI: 10.1016/j.mex.2017.02.002 (cit. on p. 38).

Nikuradse, J. (Feb. 1933). "Gesetzmäßigkeiten der turbulenten Strömung in glatten Rohren (Nachtrag)". In: *Forschung auf dem Gebiete des Ingenieurwesens* 4.1, pp. 44–44. DOI: 10.1007/BF02716946 (cit. on p. 18).

O'Carroll, D. M., K. G. Mumford, L. M. Abriola, and J. I. Gerhard (2010). "Influence of wettability variations on dynamic effects in capillary pressure". In: *Water Resources Research* 46.8. ISSN: 00431397. DOI: 10.1029/2009WR008712 (cit. on p. 41).

O'Carroll, D. M., T. J. Phelan, and L. M. Abriola (2005). "Exploring dynamic effects in capillary pressure in multistep outflow experiments". In: *Water Resources Research* 41.11, pp. 1–14. ISSN: 00431397. DOI: 10.1029/2005WR004010 (cit. on p. 41).

Olsson, J., P. Berg, A. Eronn, L. Simonsson, J. Södling, L. Wern, and W. Yang (2018). *Extremregn i nuvarande och framtida klimat Analyser av observationer och framtidsscenarier*. Swedish. Report, Series Klimatologi 47. URL: https://www.smhi.se/publikationer/publikationer/extremregn-%5C%5Ci-nuvarande-och-framtida-klimat-analyser-av-observationer%5C%5C-och-framtidsscenarier-1.129407 (cit. on p. 5).

OrgeBot (2017). *Modular-green-roof*. https://commons.wikimedia.org/wiki/File:Modular-green-roof.jpg (cit. on p. 4).

Pellichero, E., R. Glantz, M. Burns, D. Mallick, S. Y. Hsu, and M. Hilpert (2012). "Dynamic capillary pressure during water infiltration: Experiments and Green-Ampt modeling". In: *Water Resources Research* 48.6. ISSN: 00431397. DOI: 10.1029/2011WR011541 (cit. on p. 41).

Porter, M., M. Schaap, and D. Wildenschild (2009). "Lattice-Boltzmann simulations of the capillary pressure-saturation-interfacial area relationship for porous media". In: *Advances in Water Resources* 32.11, pp. 1632–1640. DOI: 10.1016/j.advwatres.2009.08.009 (cit. on p. 39).

Primkulov, B. K., A. A. Pahlavan, X. Fu, B. Zhao, C. W. MacMinn, and R. Juanes (2019). "Signatures of fluid-fluid displacement in porous media: Wettability, patterns and pressures". In: *Journal of Fluid Mechanics* 875, R4. ISSN: 14697645. DOI: 10.1017/jfm.2019.554 (cit. on pp. 40, 41).

Purcell, W. et al. (1949). "Capillary pressures-their measurement using mercury and the calculation of permeability therefrom". In: *Journal of Petroleum Technology* 1.02, pp. 39–48 (cit. on pp. 38, 43).

Qin, C. Z. and H. van Brummelen (2019). "A dynamic pore-network model for spontaneous imbibition in porous media". In: *Advances in Water Resources* 133. ISSN: 03091708. DOI: 10.1016/j.advwatres.2019.103420 (cit. on pp. 40, 41).

Raeini, A. Q., B. Bijeljic, and M. J. Blunt (2014). "Numerical Modelling of Sub-pore Scale Events in Two-Phase Flow Through Porous Media". In: *Transport in Porous Media* 101.2, pp. 191–213. ISSN: 01693913. DOI: 10.1007/s11242-013-0239-6 (cit. on p. 41).

Raiskinmäki, P., A. Shakib-Manesh, A. Jäsberg, A. Koponen, J. Merikoski, and J. Timonen (Apr. 2002). "Lattice-Boltzmann Simulation of Capillary Rise Dynamics". In: *Journal of Statistical Physics* 107.1, pp. 143–158. ISSN: 1572-9613. DOI: 10.1023/A:1014506503793 (cit. on p. 55).

Ramírez-Flores, J. C., J. Bachmann, and A. Marmur (2010). "Direct determination of contact angles of model soils in comparison with wettability characterization by capillary rise". In: *Journal of Hydrology* 382.1, pp. 10–19. ISSN: 0022-1694. DOI: https://doi.org/10.1016/j.jhydrol.2009.12.014 (cit. on p. 55).

Rätz, A. and B. Schweizer (2014). "Hysteresis models and gravity fingering in porous media". In: *ZAMM Zeitschrift fur Angewandte Mathematik und Mechanik* 94.7-8, pp. 645–654. ISSN: 15214001. DOI: 10.1002/zamm.201200052 (cit. on p. 37).

Reynolds, C. A., H. Menke, M. Andrew, M. J. Blunt, and S. Krevor (2017). "Dynamic fluid connectivity during steady-state multiphase flow in a sandstone". In: *Proceedings of the National Academy of Sciences* 114.31, pp. 8187–8192 (cit. on p. 58).

Richards, P. and R. Hoxey (Aug. 1993). "Appropriate boundary conditions for computational wind engineering models using the k-epsilon turbulence model". In: *Journal of Wind Engineering and Industrial Aerodynamics* 46-47, pp. 145–153. DOI: 10.1016/0167-6105(93)90124-7 (cit. on p. 18).

Roels, S., J. Carmeliet, and H. Hens (2003a). "Modelling unsaturated moisture transport in heterogeneous limestone - Part 2. Macroscopic simulations". In: 52.3, pp. 351–369. DOI: 10.1023/A:1023504128480 (cit. on p. 41).

Roels, S., J. Carmeliet, and H. Hens (2003b). "Modelling unsaturated moisture transport in heterogeneous limestone - Part I. A mesoscopic approach". In: 52.3, pp. 333–350. DOI: 10.1023/A:1023552011642 (cit. on p. 40).

Ross, B. (1990). "The diversion capacity of capillary barriers". In: *Water Resources Research* 26.10, pp. 2625–2629. DOI: 10.1029/WR026i010p02625 (cit. on p. 63).

Rudiyanto, B. Minasny, R. M. Shah, B. I. Setiawan, and M. T. van Genuchten (2020). "Simple functions for describing soil water retention and the unsaturated hydraulic conductivity from saturation to complete dryness". In: *Journal of Hydrology* 588. ISSN: 00221694. DOI: 10.1016/j.jhydrol.2020.125041 (cit. on p. 37).

Sadeghi, M., M. Agnaou, J. Barralet, and J. Gostick (2020). "Dispersion modeling in pore networks: A comparison of common pore-scale models and alternative approaches". In: 228. DOI: 10.1016/j.jconhyd.2019.103578 (cit. on p. 40).

Schrader, M. E. and S. Yariv (1990). "Wettability of clay minerals". In: *Journal of Colloid and Interface Science* 136.1, pp. 85–94. ISSN: 0021-9797. DOI: https://doi.org/10.1016/0021-9797(90)90080-8 (cit. on p. 55).

Schreider, S., D. Smith, and A. Jakeman (2000). "Climate change impacts on urban flooding". In: *Climatic Change* 47.1-2, pp. 91–115. DOI: 10.1023/a:1005621523177 (cit. on p. 5).

Shan, X. and H. Chen (Mar. 1993). "Lattice Boltzmann model for simulating flows with multiple phases and components". In: *Phys. Rev. E* 47 (3), pp. 1815–1819. DOI: 10.1103/PhysRevE.47.1815 (cit. on pp. 49, 50).

Siltecho, S., C. Hammecker, V. Sriboonlue, C. Clermont-Dauphin, V. Trelo-Ges, A. Antonino, and R. Angulo-Jaramillo (2015). "Use of field and laboratory methods for estimating unsaturated hydraulic properties under different land uses". In: *Hydrology and Earth System Sciences* 19.3, pp. 1193–1207. DOI: 10.5194/hess-19-1193-2015 (cit. on p. 38).

Slobozhanin, L., J. Alexander, S. Collicott, and S. Gonzalez (2006). "Capillary pressure of a liquid in a layer of close-packed uniform spheres". In: *Physics of Fluids* 18.8. DOI: 10.1063/1.2236123 (cit. on p. 54).

Solazzi, S. G., J. G. Rubino, D. Jougnot, and K. Holliger (2020). "Dynamic permeability functions for partially saturated porous media". In: *Geophysical Journal International* 221.2, pp. 1182–1189. ISSN: 1365246X. DOI: 10.1093/gji/ggaa068 (cit. on p. 41).

Soltani, A., M. Azimi, A. Deng, and A. Taheri (2019). "A simplified method for determination of the soil–water characteristic curve variables". In: *International Journal of Geotechnical Engineering* 13.4, pp. 316–325. DOI: 10.1080/19386362.2017.1344450 (cit. on p. 38).

Stovin, V., G. Vesuviano, and H. Kasmin (2012). "The hydrological performance of a green roof test bed under UK climatic conditions". In: *Journal of Hydrology* 414-415, pp. 148–161. DOI: 10.1016/j.jhydrol.2011.10.022 (cit. on p. 5).

Suh, H. S., D. H. Kang, J. Jang, K. Y. Kim, and T. S. Yun (Dec. 2017). "Capillary pressure at irregularly shaped pore throats: Implications for water retention characteristics". In: *Advances in Water Resources* 110, pp. 51–58. ISSN: 0309-1708. DOI: 10.1016/J.ADVWATRES.2017.09.025 (cit. on pp. 39, 60).

Susca, T. (2019). "Green roofs to reduce building energy use? A review on key structural factors of green roofs and their effects on urban climate". In: *Building and Environment* 162. DOI: 10.1016/j.buildenv.2019.106273 (cit. on p. 5).

Tariku, F., K. Kumaran, and P. Fazio (July 2010). "Transient model for coupled heat, air and moisture transfer through multilayered porous media". In: *International Journal of Heat and Mass Transfer* 53.15-16, pp. 3035–3044. DOI: 10.1016/j.ijheatmasstransfer.2010.03.024 (cit. on p. 36).

Tominaga, Y., A. Mochida, R. Yoshie, H. Kataoka, T. Nozu, M. Yoshikawa, and T. Shirasawa (Oct. 2008). "AIJ guidelines for practical applications of CFD to pedestrian wind environment around buildings". In: *Journal of Wind Engineering and Industrial Aerodynamics* 96.10-11, pp. 1749–1761. DOI: 10.1016/j.jweia.2008.02.058 (cit. on p. 18).

Toussaint, R., K. Måløy, Y. Méheust, G. Løvoll, M. Jankov, G. Schäfer, and J. Schmittbuhl (2012). "Two-Phase Flow: Structure, Upscaling, and Consequences for Macroscopic Transport Properties". In: *Vadose Zone Journal* 11.3, vzj2011.0123. ISSN: 1539-1663. DOI: 10.2136/vzj2011.0123 (cit. on p. 41).

Van Belleghem, M., M. Steeman, H. Janssen, A. Janssens, and M. De Paepe (Nov. 2014). "Validation of a coupled heat, vapour and liquid moisture transport model for porous materials implemented in CFD". In: *Building and Environment* 81, pp. 340–353. DOI: 10.1016/j.buildenv.2014.06.024 (cit. on p. 35).

Van Renterghem, T., M. Hornikx, J. Forssen, and D. Botteldooren (2013). "The potential of building envelope greening to achieve quietness". In: *Building and Environment* 61, pp. 34–44. ISSN: 0360-1323. DOI: https://doi.org/10.1016/j.buildenv.2012.12.001 (cit. on p. 4).

Viecco, M., S. Vera, H. Jorquera, W. Bustamante, J. Gironás, C. Dobbs, and E. Leiva (2018). "Potential of particle matter dry deposition on green roofs and living walls vegetation for mitigating urban atmospheric pollution in semiarid climates". In: *Sustainability (Switzerland)* 10.7. DOI: 10.3390/su10072431 (cit. on p. 4).

Vijayaraghavan, K. and U. Joshi (2015). "Application of seaweed as substrate additive in green roofs: Enhancement of water retention and sorption capacity". In: *Landscape and Urban Planning* 143, pp. 25–32. DOI: 10.1016/j.landurbplan.2015.06.006 (cit. on p. 4).

De-Ville, S., M. Menon, X. Jia, G. Reed, and V. Stovin (2017). "The impact of green roof ageing on substrate characteristics and hydrological performance". In: *Journal of Hydrology* 547, pp. 332–344. ISSN: 00221694. DOI: 10.1016/j.jhydrol.2017.02.006 (cit. on p. 75).

Viola, F., M. Hellies, and R. Deidda (2017). "Retention performance of green roofs in representative climates worldwide". In: *Journal of Hydrology* 553, pp. 763–772. DOI: 10.1016/j.jhydrol.2017.08.033 (cit. on p. 44).

Virnovsky, G. A., H. A. Friis, and A. Lohne (2004). "A Steady-State Upscaling Approach for Immiscible Two-Phase Flow". In: *Transport in Porous Media* 54.2, pp. 167–192. ISSN: 01693913. DOI: 10.1023/A:1026363132351 (cit. on p. 37).

Vogel, H.-J., J. Tölke, V. P. Schulz, M. Krafczyk, and K. Roth (2005). "Comparison of a Lattice-Boltzmann Model, a Full-Morphology Model, and a Pore Network Model for Determining Capillary Pressure-Saturation Relationships". In: *Vadose Zone Journal* 4.2, pp. 380–388. ISSN: 1539-1663. DOI: 10.2136/vzj2004.0114 (cit. on pp. 40, 41).

Wadsö, L., K. Svennberg, and A. Dueck (2004). "An experimentally simple method for measuring sorption isotherms". In: *Drying Technology* 22.10, pp. 2427–2440. DOI: 10.1081/DRT-200032898 (cit. on p. 38).

Washburn, E. W. (Mar. 1921). "The Dynamics of Capillary Flow". In: *Phys. Rev.* 17 (3), pp. 273–283. DOI: 10.1103/PhysRev.17.273 (cit. on p. 58).

Wayllace, A. and N. Lu (2012). "A transient water release and imbibitions method for rapidly measuring wetting and drying soil water retention and hydraulic conductivity functions". In: *Geotechnical Testing Journal* 35.1. DOI: 10.1520/GTJ103596 (cit. on p. 38).

Weill, S., E. Mouche, and J. Patin (2009). "A generalized Richards equation for surface/subsurface flow modelling". In: *Journal of Hydrology* 366.1-4, pp. 9–20. DOI: 10.1016/j.jhydrol.2008.12.007 (cit. on p. 36).

Weitz, D., J. Stokes, R. Ball, and A. Kushnick (1987). "Dynamic Capillary Pressure in Porous Media: Origin of the Viscous-Fingering Length Scale". In: 59.26, pp. 2967–2970. DOI: 10.1103/PhysRevLett.59.2967 (cit. on pp. 39, 67, 69, 70).

Whitaker, S. (1986). "Flow in porous media I: A theoretical derivation of Darcy's law". In: *Transport in Porous Media* 1.1, pp. 3–25. DOI: 10.1007/BF01036523 (cit. on pp. 42, 43).

Wong, G. K. L. and C. Y. Jim (Sept. 2014). "Quantitative hydrologic performance of extensive green roof under humid-tropical rainfall regime". In: *Ecological Engineering* 70, pp. 366–378. DOI: 10.1016/j.ecoleng.2014.06.025 (cit. on p. 5).

Xing, Q., X. Hao, Y. Lin, H. Tan, and K. Yang (2019). "Experimental investigation on the thermal performance of a vertical greening system with green roof in wet and cold climates during winter". In: *Energy and Buildings* 183, pp. 105–117. DOI: 10.1016/j.enbuild.2018.10.038 (cit. on p. 5).

Yang, J., I. Bondino, M. Regaieg, and A. Moncorgé (2017). "Pore to pore validation of pore network modelling against micromodel experiment results". In: *Computational Geosciences* 21.5-6, pp. 849–862. ISSN: 15731499. DOI: 10.1007/s10596-017-9630-7 (cit. on p. 41).

Yang, Q.-s. and J. Zhang (2009). "Simulation of Horizontally Homogeneous Atmosphere Boundary Layer Based on K-E Variant Models Combined With Modified Wall Functions". In: *The Seventh Asia-Pacific Conference on Wind Engineering* 2004, pp. 1–8 (cit. on p. 18).

Yang, Y., M. Gu, S. Chen, and X. Jin (Feb. 2009). "New inflow boundary conditions for modelling the neutral equilibrium atmospheric boundary layer in computational wind engineering". In: *Journal of Wind Engineering and Industrial Aerodynamics* 97.2, pp. 88–95. DOI: 10.1016/j.jweia.2008.12.001 (cit. on p. 18).

Zhang, H. and P. A. Zegeling (2017). "A Numerical Study of Two-Phase Flow Models with Dynamic Capillary Pressure and Hysteresis". In: *Transport in Porous Media* 116.2, pp. 825–846. ISSN: 15731634. DOI: 10.1007/s11242-016-0802-z (cit. on p. 37).

Zhao, J., F. Qin, D. Derome, and J. Carmeliet (2020). "Simulation of quasi-static drainage displacement in porous media on pore-scale: Coupling lattice Boltzmann method and pore network model". In: 588. DOI: 10.1016/j.jhydrol.2020.125080 (cit. on p. 40).

Zhou, Y., J. O. Helland, and E. Jettestuen (2013). "Dynamic capillary pressure curves from pore-scale modeling in mixed-wet-rock images". In: *SPE Journal*. Vol. 18. 4, pp. 634–645. DOI: 10.2118/154474-PA (cit. on p. 41).

Zhuang, L., C. Duijn, and S. M. Hassanizadeh (2019). "The Effect of Dynamic Capillarity in Modeling Saturation Overshoot during Infiltration". In: *Vadose Zone Journal* 18.1, pp. 1–14. ISSN: 1539-1663. DOI: 10.2136/vzj2018.07.0133 (cit. on p. 37).

Part II

Appended papers

Paper 1

Simulating wind-driven rain on building facades using Eulerian multiphase with rain phase turbulence model

Kaj Pettersson, Sinisa Krajnovic, Angela Sasic Kalagasidis, Pär Johansson

Building and Environment (2016), 106: 1–9.

Paper 1. Simulating wind-driven rain on building facades using Eulerian multiphase with rain phase turbulence model

Kaj Pettersson, Sinisa Krajnovic, Angela Sasic Kalagasidis, Pär Johansson

Paper 2

On the impact of porous media microstructure on rainfall infiltration of thin homogeneous green roof growth substrates

Kaj Pettersson, Dario Maggiolo, Srdjan Sasic, Pär Johansson, Angela Sasic Kalagasidis

Journal of Hydrology (2019), 582: 124286

Paper 2. On the impact of porous media microstructure on rainfall infiltration of thin homogeneous green roof growth substrates

Kaj Pettersson, Dario Maggiolo, Srdjan Sasic, Pär Johansson,
Angela Sasic Kalagasidis

Paper 3

Contribution of dynamic capillary pressure to rainfall infiltration in thin homogeneous growth substrates

Kaj Pettersson, Dario Maggiolo, Srdjan Sasic, Pär Johansson, Angela Sasic Kalagasidis

Postprint, under review, 2021

The paper was reformatted for uniformity, but otherwise is unchanged.

Paper 3. Contribution of dynamic capillary pressure to rainfall infiltration in thin homogeneous growth substrates

Kaj Pettersson, Dario Maggiolo, Srdjan Sasic, Pär Johansson,
Angela Sasic Kalagasidis

Paper 4

Impact of topological heterogeneity on liquid infiltration of a thin growth substrate using lattice Boltzmann on XMT scanned core images

Kaj Pettersson, Dario Maggiolo, Srdjan Sasic, Pär Johansson, Angela Sasic Kalagasidis

-

The paper was reformatted for uniformity, but otherwise is unchanged.

Paper 4. Impact of topological heterogeneity on liquid infiltration of a thin growth substrate using lattice Boltzmann on XMT scanned core images

Kaj Pettersson, Dario Maggiolo, Srdjan Sasic, Pär Johansson,
Angela Sasic Kalagasidis